Investigation of Plasma Potential Enhancement in the Scrape-Off Layer of Ion Cyclotron Range of Frequencies Heated Discharges on Alcator C-Mod

by

Roman Igorevitch Ochoukov

Submitted to the Department of Nuclear Science and Engineering
in partial fulfillment of the requirements for the degree of

Doctor of Philosophy in Nuclear Science and Engineering

at the

MASSACHUSETTS INSTITUTE OF TECHNOLOGY

September 2013

Author .....
Department of Nuclear Science and Engineering
August 9, 2013

Certified by .....
Dennis G. Whyte
Professor, Department of Nuclear Science and Engineering
Thesis Supervisor

Certified by .....
Bruce Lipschultz
Senior Research Scientist, Plasma Science and Fusion Center
Thesis Reader

Accepted by .....
Mujid S. Kazimi
TEPCO Professor of Nuclear Engineering
Chair, Department Committee on Graduate Students

Investigation of Plasma Potential Enhancement in the Scrape-Off Layer of Ion Cyclotron Range of Frequencies Heated Discharges on Alcator C-Mod

by

Roman Igorevitch Ochoukov

Submitted to the Department of Nuclear Science and Engineering
on August 9, 2013, in partial fulfillment of the
requirements for the degree of
Doctor of Philosophy in Nuclear Science and Engineering

Abstract

ICRF-heated discharges on Alcator C-Mod are associated with enhanced sputtering of molybdenum plasma facing surfaces and increased levels of core impurity contents, which subsequently degrade the core plasma performance. RF sheath rectification on open magnetic field lines that intercept material surfaces is currently suspected of causing an enhancement of molybdenum impurity sources by increasing the energy with which incident plasma ions strike material surfaces. While it has previously been observed that plasma potentials on open magnetic field lines are enhanced in ICRF-heated discharges on Alcator C-Mod, a direct link between local RF wave fields and plasma potentials has yet to be established.

Experimental measurements reveal that regions that directly magnetically map and do not map to the active antennas experience plasma potential enhancement. The "mapped" results are consistent with the slow wave rectification mechanism where the plasma potential enhancement is a result of rectification of the slow ICRF wave electric field launched directly by the antenna. This rectification mechanism is localized to regions directly magnetically mapped to the active antennas and occurs over a narrow plasma density range where the slow waves can propagate. The potential enhancement in the "unmapped" regions (inaccessible to directly launched slow waves) correlates well with the local fast wave fields and has multiple features that are consistent with the theory that involves fast waves coupling to a slow wave at a conducting surface, which then leads to rectification of the plasma potential.

Cross field profile measurements reveal that the plasma density profile is also affected by ICRF power and it is suspected that the gradients in the plasma potential profile are responsible for the density profile changes through $\mathbf{E}\times\mathbf{B}$ plasma flows along equipotential surfaces. The implications are that the absolute plasma potentials and the plasma potential gradients are capable of affecting molybdenum sputtering and sources by modifying the sputtering yield and the incident ion flux, respectively.

Thesis Supervisor: Dennis G. Whyte
Title: Professor, Department of Nuclear Science and Engineering

Thesis Reader: Bruce Lipschultz
Title: Senior Research Scientist, Plasma Science and Fusion Center

Acknowledgments

The work presented in this thesis would not be possible without the contribution from a great number of people who work for the Plasma Science and Fusion Center and elsewhere in the field of nuclear fusion and plasma physics. In the following paragraph I would like to acknowledge their contributions.

I would like to thank: Jessica Coco, Valerie Censabella, and Dragana Zubcevic for their help with numerous administrative tasks and Lee Keating for keeping our fabrication accounts in order; Heather Barry and Clare Egan for keeping the department of Nuclear Science and Engineering organized; our IT gurus – Josh Stillerman, Henry Bergler, Brandon Savage, Lee Berkowitz, and Felix Kreisel – for promptly resolving any data acquisition related issues; Ed Fitzgerald for his expertise in all things mechanical, I learned a great deal of technical skills from him; Mark Iverson and Sue Agabian for their help with the assembly and construction of the Surface Science Station; Soren Harrison and Niels Gierse for their tremendous help with designing and building the Surface Science Station; Frank Shefton for his help with installing the gas cooling system on the Surface Science Station; Dave Arsenault for his welding work on the Surface Science Station; Joseph Bosco and Yuri Rokhman for their help with the PLC control system during overnight boronization experiments; Jeff Doody and Bill Beck for their assistance with disruption-induced stress analysis of the Surface Science Station; Charlie Cauley and Bill Forbes for their help and assistance in machining parts of the Surface Science Station; Paul Lienard, Rick Leccacorvi, and Henry Savelli for their expertise in CAD drawing of various parts and components of the Surface Science Station; the members of the electronics shop – Willy Burke, Bruce Wood, Bill Parkin, Dave Bellofatto, and Maria Silveira – for their contribution in designing and putting together all things electrical on the Surface Science Station. Additional thanks are to Willy Burke for his involvement in the design and building of the emissive probe power supplies; our vacuum experts – Bob Childs, Tom Toland, and Ron Rosati – for their expertise with vacuum systems in and around Alcator C-Mod; graduate students Mike Garrett, Matt Reinke, Harold Barnard, Mike

Churchill, Jeff Olynyk, Yuri Podpaly, Bob Mumgaard, Kenny Marr, Nate Howard, Ted Golfinopoulos, Ian Faust, Orso Meneghini, Igor Bespamyatnov, Dan Brunner, Greg Wallace, Cornwall Lau, Aaron Bader, Seung Gyou Baek, Choongki Sung, Istvan Cziegler, Chi Gao, John Walk, Jinseok Ko, Yunxing Ma, Leonardo Patacchini, Peng Xu, and many more for providing great camaraderie in the control room. Additional thanks are to Dan Brunner and Brian LaBombard for their help with anything probe-related and to Jim Terry and Istvan Cziegler for their assistance with the gas puff imaging diagnostic; the members of the ICRF group – Andy Pfeiffer, Rick Murray, Steve Wukitch, Yijun Lin, and Alan Binus – for maintaining the RF system on Alcator C-Mod; the lower hybrid team – Pat MacGibbon, Dave Johnson, and Atma Kanojia – for their expertise in anything related to electromagnetic waves in the GHz frequency range; Rui Vieira and Sam Pierson for helping with in-vessel work on Alcator C-Mod; Pete Stahle and Graham Wright for their help with assembling and setting up the DIONISOS experiment at MIT; Matt Fulton and Catherine Fiore for their effort in keeping the PSFC and Alcator C-Mod a safe place to be a student and a researcher; Mike Rowell for providing a tour of the alternator; Tim Davis for his help with shipping equipment to and from the Plasma Science and Fusion Center; Earl Marmar, Jim Irby, and Gary Dekow for keeping Alcator C-Mod a state-of-the-art tokamak facility; Jim Myra and Dan D'Ippolito for their invaluable contributions to the theoretical treatment of the RF wave-plasma sheath interaction; Paul Bonoli and Syun'ichi Shiraiwa for productive discussions on the theoretical aspects of ICRF waves in plasmas; professors Tony Haasz, Peter Stangeby, and Jim Davis for introducing me to the field of nuclear fusion and plasma physics; professors Ian Hutchinson, Jeff Freidberg, and Ron Parker for their superb classes on how plasma physics really works; my friends – Lev Vaisman and Aleksey Tyshchenko – for the numerous bowling sessions played together; professor Dennis Whyte, my thesis supervisor, and Dr. Bruce Lipschultz, my thesis reader, for supervising my thesis work for seven years at MIT.

Above all else I would like to acknowledge the support of my mother. I dedicate this thesis to her.

Contents

List of Figures

List of Tables

Chapter 1

Introduction

Nuclear fusion is currently being pursued as a long term solution to humanity's energy needs. A leading process to achieve controlled nuclear fusion energy relies on the use of a magnetic field to confine fusing fuel and its products. Since temperatures at which fusion needs to take place are 10-20 keV, or 100-200 million K ($1\ eV = 11600\ K$), the fusing particles are in a state of plasma. The most advanced magnetic confinement device is a tokamak. A detailed overview of magnetically confined nuclear fusion energy may be found in [1].

Figure 1-1 shows a diagram of a typical tokamak. An excellent overview of how the device operates may be found in [2]. The two dominant magnetic features of a tokamak are a toroidal magnetic field (B_{Tor}) generated by external toroidal magnetic field coils and a poloidal magnetic field (B_P) generated by a toroidal electric current (I_P) flowing in the plasma. The toroidal current I_P is driven inductively by the central solenoid. Additional poloidal field coils are required to shape the plasma and control its position.

In order to reach fusion-relevant temperatures in a tokamak, plasmas require external heating schemes. These schemes need to operate in the presence of large magnetic fields, account for high plasma temperatures, and tolerate any possible deleterious interactions with the plasma. Electro-magnetic wave heating at the ion cyclotron range-of frequencies (ICRF) wave spectrum (frequencies in the range of 10-100 MHz) is one such scheme and it will be discussed in more detail in the following subsection.

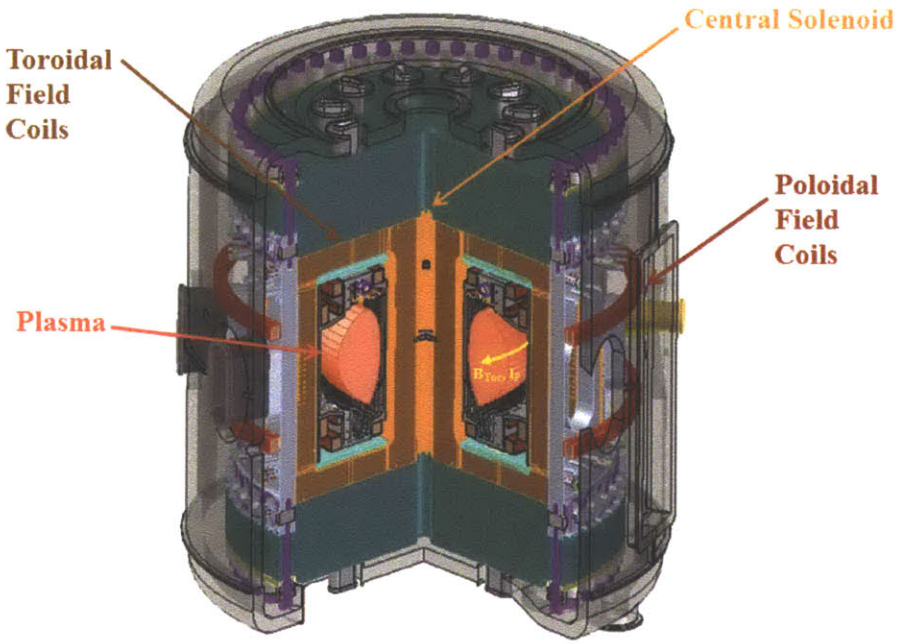

Figure 1-1: A diagram of Alcator C-Mod tokamak that shows key components.

1.1 ICRF heating of tokamak plasmas

The purpose of this section is to introduce the key concepts relevant to ICRF heating of tokamak plasmas and a more detailed theoretical treatment of waves in plasmas will be provided in Chapter 4. Auxiliary heating using ICRF waves, electro-magnetic waves in the frequency range of 10-100 MHz, is a commonly employed technique on tokamaks to reach fusion relevant plasma temperatures. The technique has been employed on Alcator C-Mod [3], DIII-D [4], NSTX [5], TFTR [6], JET [7], ASDEX Upgrade [8], Tore Supra [9], JT-60 [10], and many other tokamaks. ITER, the next generation tokamak experiment, is going to rely on 20 MW of ICRF power to accomplish its scientific mission [11].

ICRF heating relies on waves damping their power on the ions the Larmor motion of which is resonant with the wave electric field. The position of the resonance in a tokamak is determined by the magnetic field profile in the plasma. The Larmor ion frequency (f_{ci}) is given by Equation 1.1:

$$f_{ci} = \frac{q_i B}{2\pi m_i}, \tag{1.1}$$

where q_i is the ion charge, B is the magnetic field strength, and m_i is the ion mass. The radial (along the major radius direction R) profile of the magnetic field in a tokamak can be approximated by the toroidal magnetic field profile, $B \approx B_T$, which is given by Equation 1.2:

$$B_T = \frac{R_o B_{To}}{R}, \tag{1.2}$$

where R_o is the major radius on-axis location, B_{To} is the toroidal field strength at R_o, and R is the major radius location. The relation between the major radius position of the ion cyclotron resonance location (R_{ci}) and the frequency of the launched ICRF waves becomes:

$$R_{ci} = \frac{q_i B_{To} R_o}{2\pi m_i f_{ci}}. \tag{1.3}$$

We are going to demonstrate the basic principles of ICRF heating on a particular case of Alcator C-Mod tokamak: $B_{To} = 5.4\ T$, $R_o = 0.67\ m$. Figure 1-2 shows

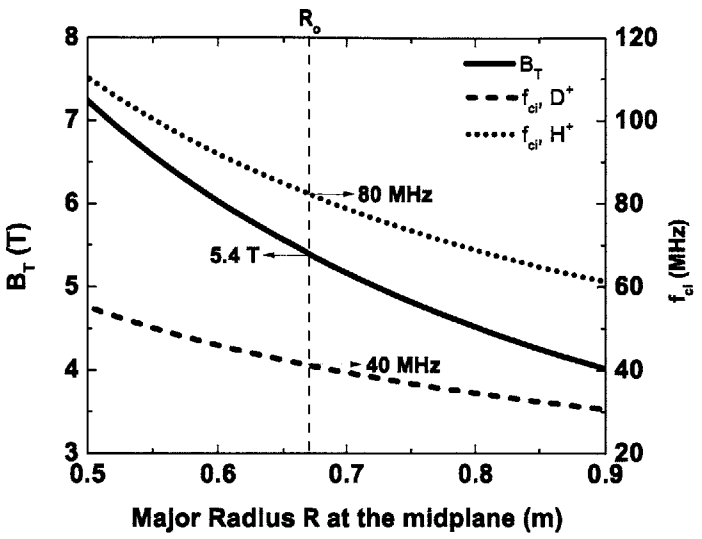

Figure 1-2: The radial profiles of the toroidal magnetic field, the deuterium ion cyclotron frequency, and the hydrogen ion cyclotron frequency on Alcator C-Mod tokamak. R_o refers to the on-axis major radius location.

the values of the ion cyclotron frequencies at the on-axis major radius position for deuterium ($f_{ci,\ D^+} \approx 40\ MHz$) and hydrogen ($f_{ci,\ H^+} \approx 80\ MHz$) ions. In order to heat the plasma at these resonance locations, the ICRF wave needs 1) to have good accessibility to that region, i.e. to be able to propagate from the launching structure to the resonance and 2) to have a wave resonance at this location in order for the wave power to be absorbed by the plasma species. A detailed overview of waves in plasmas is provided by Stix [12].

The key equation that governs the wave propagation in the plasma is called the dispersion relation and for our particular case the equation is:

$$n_\perp^2 = \frac{(R - n_{//}^2)(L - n_{//}^2)}{S - n_{//}^2}, \tag{1.4}$$

where $n_\perp$ and $n_{//}$ are the perpendicular and the parallel components of the wave index of refraction, respectively, and R, L, and S are the elements of the plasma dielectric tensor. Equation 1.4 represents the dispersion relation for the so-called fast ICRF wave, where the term "fast" refers to the wave phase velocity v_ϕ. Typically, $n_{//}$ is set by the launching structure, while $n_\perp$ governs the radial propagation of the wave. The

R, L, and S components depend on the electron and ion plasma frequencies, on the electron and ion cyclotron frequencies, on the frequency of the launched waves, and (if present) on the plasma and cyclotron frequencies of impurity ions. The complete derivation of the three terms is given in Stix [12] and the final forms are shown below:

$$R = 1 - \sum_s \frac{\omega_{ps}^2}{\omega(\omega + \Omega_s)}, \tag{1.5}$$

where ω_{ps} is the angular plasma frequency for particles of type s (electrons, main ions, or impurity ions), ω is the angular frequency of the launched waves, and Ω_s is the angular cyclotron (or Larmor) frequency for particles of type s.

$$L = 1 - \sum_s \frac{\omega_{ps}^2}{\omega(\omega - \Omega_s)}, \tag{1.6}$$

$$S = \frac{1}{2}(R + L). \tag{1.7}$$

Note that the dispersion relation 1.4 is derived for the collisionless cold plasma approximation and this assumption is valid for typical tokamak plasmas.

For the case of Alcator C-Mod the ICRF waves are launched with a typical $n_{//} = 10$. Figure 1-3 shows the dispersion relation for pure deuterium plasmas and deuterium plasmas with a 10% hydrogen minority fraction. We use a parabolic radial plasma density profile to estimate the individual terms in the dispersion relation. The frequency of the launched waves is 80 MHz. We see that there is no wave resonance at the ion cyclotron resonance location for the pure deuterium plasma. This is due to the wave electric field rotating in the direction opposite to the gyrating main ions. However, there is a wave resonance for the hydrogen minority case in the vicinity of the ion cyclotron resonance location. As the fast ICRF wave approaches the resonance location and its wave number k becomes very large ($k \to \infty$, where $k = \frac{n\omega}{c}$ and c is the speed of light), the fast wave phase velocity $v_\phi = \frac{\omega}{k}$ is significantly reduced and the wave begins to transfer its energy to the minority ions. As a result, one of the most commonly employed ICRF heating schemes in tokamaks relies on heating the

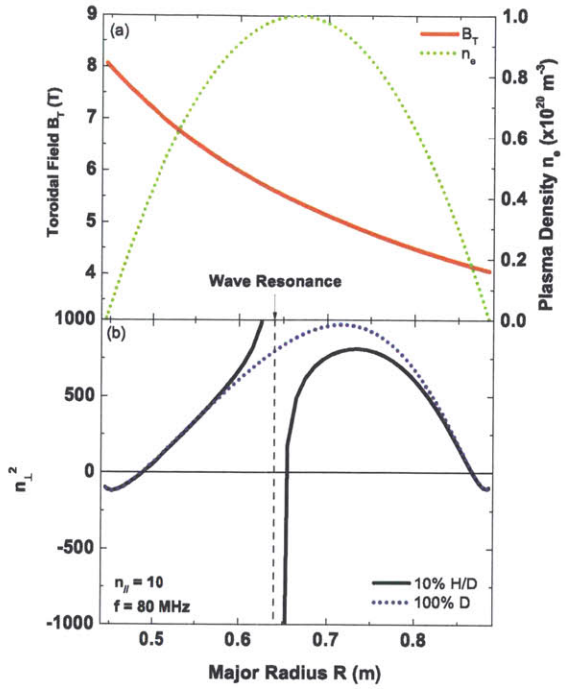

Figure 1-3: Radial profiles of (a) the toroidal magnetic field and the plasma density and (b) of the ICRF wave dispersion. The wave dispersion is shown for pure deuterium plasmas and for plasmas with 10% hydrogen minority fraction. The launched index of refraction is $n_{//} = 10$ and the launched wave frequency $f = 80\ MHz$.

minority ion species, which then collisionally heats the electron and main ion plasma species. In order to estimate the wave absorption near the ion cyclotron resonance it is necessary to include the effect of the finite electron and ion plasma temperature [13]. A detailed treatment of the fast ICRF wave absorption in the plasma core is beyond the scope of this thesis. A good summary of ICRF wave heating of tokamak plasmas can be found in [1].

Another important observation from Figure 1-3 (b) is that the perpendicular index of refraction becomes negative when the plasma density drops below $\sim 1 \times 10^{19}\ m^{-3}$. This implies that the fast ICRF wave is no longer radially propagating but is evanescent. The strength of the evanescence of the fast wave is proportional to $\frac{1}{|k_\perp|}$ and the characteristic e-folding decay length of the fast wave amplitude is typically several cm for $n_{//} \sim 10$ and $f = 80\ MHz$.

ICRF waves are launched by an antenna located in the boundary region of tokamak plasma. The plasma boundary region is defined by the region where magnetic field lines are open and are terminated by material plasma facing components (PFCs). An example of the Alcator C-Mod tokamak plasma cross section is shown in Figure 1-4. Figure 1-4 identifies the boundary plasma region, which is often called the scrape-off layer or SOL, and the core region where magnetic flux surfaces are closed. The separatrix is the flux surface that separates the core and the SOL plasmas. The plasma parameters (the plasma density n_e and the electron temperature T_e) in the boundary region in a tokamak are typically: $n_e \leq 1 \times 10^{19}\ m^{-3}$ and $T_e = 5 - 30\ eV$ [14]. This compares to $n_e \geq 1 \times 10^{20}\ m^{-3}$ and $T_e > 1\ keV$ in the plasma core. The position of the ICRF antenna in the boundary region is governed by two criteria. The first criteria demands the position of the antenna to be as close as possible to the main plasma: the ICRF wave that is used to heat the core plasma can only propagate in the high plasma density core region and is evanescent in the low plasma density boundary region. Therefore, to maximize the amount of ICRF power transmitted to the core, the length of the evanescent region between the core and the antenna need to be minimized [1]. The second criteria demands that the interaction between the antenna structure and the plasma needs to be minimized. Therefore, the position of the antenna cannot be too close to the high density core plasma. The balance between the two criteria ultimately determines the position of the ICRF antenna in the boundary plasma region and it is typically several cm radially away from the core plasma.

Figure 1-5 shows the key components of a (field-aligned) ICRF antenna on Alcator C-Mod. The ICRF waves are launched by RF currents driven along the ICRF antenna current straps at the ICRF frequency. The toroidal spacing of the straps and the phase difference between the amplitudes of the RF currents in the straps determine the launched $n_{//}$ value. The current straps are surrounded by the Faraday screen and the RF antenna box. The purpose of the RF antenna box and the Faraday screen is to protect the current straps from plasma exposure without impeding the antenna operation. The physical dimensions of the antenna and its internal structures

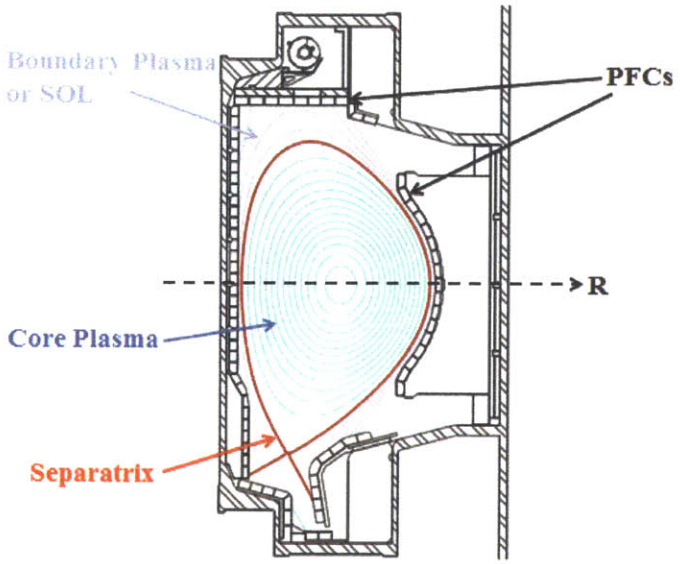

Figure 1-4: The cross section of a typical plasma discharge on Alcator C-Mod. The SOL refers to the scape-off layer region. The PFCs refer to the plasma facing components. R is the major radius direction.

are constrained by the power handling properties of the antenna material: while minimizing plasma-antenna interactions demands a minimal antenna "footprint" in a tokamak, avoiding breakdowns associated with high RF power densities and high voltages places a constraint on how small an ICRF antenna can be.

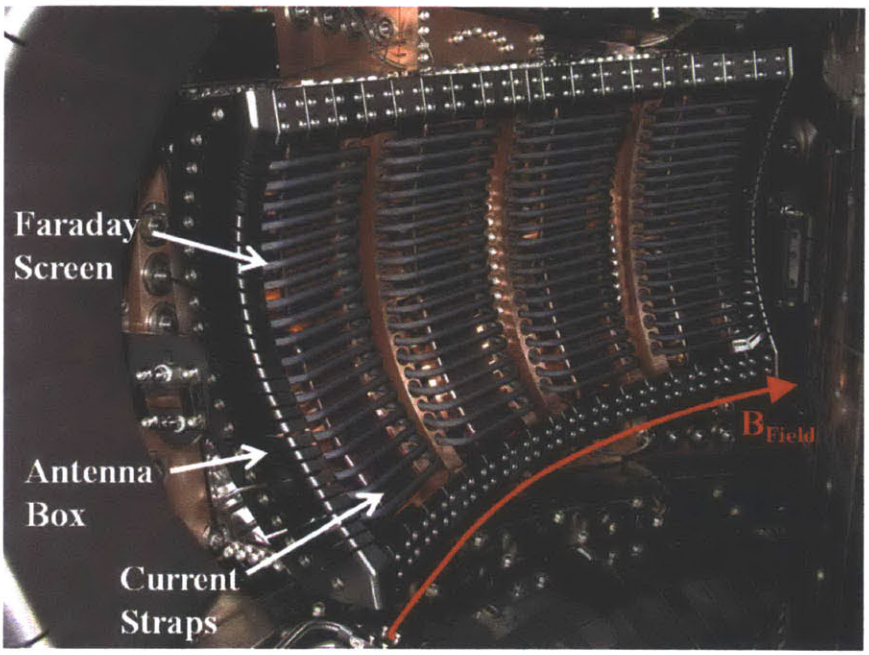

Figure 1-5: An in-vessel view of a (field-aligned) ICRF antenna on Alcator C-Mod. Major components of the antenna are shown. B_{field} refers to the direction of the magnetic field.

1.2 Tokamak operation in ICRF-heated discharges

In order to minimize the deleterious effects of plasma-material interactions on in-vessel components in a tokamak the plasma facing surfaces of the in-vessel structures (including ICRF antennas) are armored with a protective material. Some of the most important properties required of the protective material are: 1) to be able to withstand high heat loads and prevent melting; 2) to be able to withstand the bombardment by energetic particles and prevent erosion; 3) to be chemically inert and prevent retention of the species that comprise the plasma.

High-Z refractory metals, such as molybdenum (Mo) and tungsten (W), meet the above-mentioned criteria to serve as plasma-facing components (PFCs). The melting temperature of refractory metals is generally high with W having the highest melting temperature of any known material at 3700 K [15]. As a result, the refractory metals are capable of tolerating higher transient heat loads without compromising their integrity in the form of melting.

The high atomic number of the high-Z refractory metals also makes it an excellent PFC candidate that has a substantially reduced physical sputtering yield due to incident plasma ion fluxes. The low sputtering yield is due to the large mass difference between the main ion plasma species and the high-Z PFCs. This mass difference can be large by as much as a factor of $\sim$100 for the case of deuterium main ions (atomic mass of 2) and tungsten PFCs (atomic mass of 184). The underlying physical principles that govern physical ion sputtering are: collisions between incident ions and material atoms are binary and elastic, energy and momentum are conserved, and neutral atoms are bound to the surface with a binding energy E_s. Based on these assumptions we can calculate the energy transferred from incident ions to neutral surface atoms (ΔE):

$$\Delta E = E_i \frac{4M_iM_s}{(M_i + M_s)^2} \cos(\alpha)^2 = E_i \gamma \cos(\alpha)^2, \tag{1.8}$$

where E_i is the energy with which the incident ions strike the PFC surface, M_i is the mass of the incident ion, M_s is the mass of the target neutral atom ($M_s = M_{Mo} = 96$

for the case of Alcator C-Mod), α is the angle at which the incident ions strike the PFC surface, and $\gamma \equiv \frac{4M_iM_s}{(M_i+M_s)^2}$ is the maximum energy transfer coefficient. Accounting for the surface binding energy (E_s, which for the particular case of Mo is taken as the sublimation energy of 6.9 eV [16]) we see that in order to induce sputtering incident ions must have a minimum energy equal to the sputtering threshold energy E_{th}:

$$E_{th} = \frac{E_s}{\gamma \cos(\alpha)^2}. \tag{1.9}$$

If we have light hydrogenic ions sputtering much heavier high-Z PFCs, which is the case for Alcator C-Mod, then Equation 1.9 needs to be modified to account for possible reflections [17]:

$$E_{th'} = \frac{E_s}{\gamma(1-\gamma)\cos(\alpha)^2}. \tag{1.10}$$

Bohdansky [17, 18] derived an empirically-based relation for the sputtering yield Y for normal incidence ($\alpha = 0$), which we are going to use to estimate the sputtering yield:

$$Y(E_i, \alpha = 0) = QS_n(\frac{E_i}{E_{TF}})g(\frac{E_i}{E_{th}}), \tag{1.11}$$

where Q is the experimentally constrained yield factor in units of atoms/ion, S_n is the nuclear stopping function (see Equation 1.12, [19]), E_{TF} is the characteristic Thomas-Fermi energy (see Equation 1.13, [19]) and g is a threshold function (see Equation 1.14):

$$S_n(E_i/E_{TF}) = \frac{0.5\ln(1+1.2288E_i/E_{TF})}{E_i/E_{TF} + 0.1728\sqrt{E_i/E_{TF}} + 0.008(E_i/E_{TF})^{0.1504}}. \tag{1.12}$$

$$E_{TF} = 30.74\frac{M_i+M_s}{M_s}Z_iZ_s(Z_i^{2/3}+Z_s^{2/3})^{1/2}, \tag{1.13}$$

where Z_i is the projectile atomic number and Z_s is the target material atomic number.

$$g(E_i/E_{th}) = (1-(E_{th}/E_i)^{2/3})(1-E_{th}/E_i)^2. \tag{1.14}$$

Using Equation 1.11 for the case of Alcator C-Mod we can estimate the sputtering

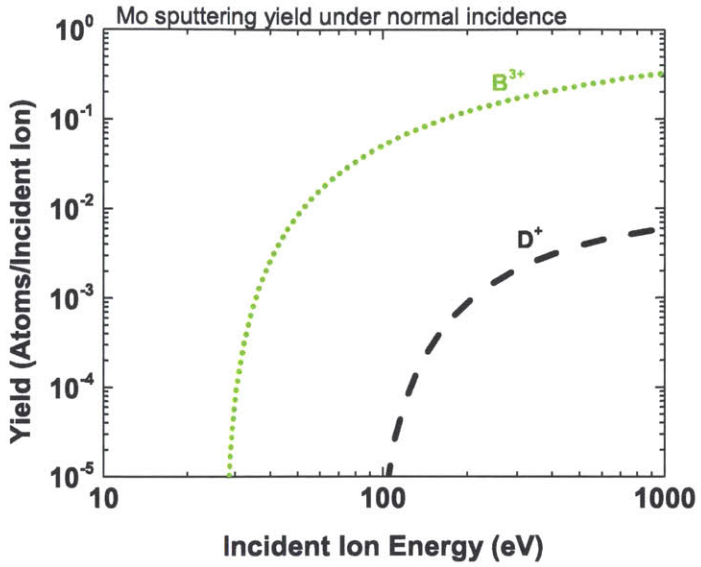

Figure 1-6: Estimated Mo sputtering yields due to normally incident D^+ and B^{3+} ions. The estimates are based on the empirical Bohdansky Equation 1.11 [17].

yield of Mo PFCs due to the bombardment by the main ion species (D^+) and the most common impurity ions (B^{3+} [20]). Figure 1-6 shows the sputtering yield of Mo due to normally incident D^+ and B^{3+} ions. We see that the ions need to strike the surface with a minimum incident energy $E_{th'}$ to induce sputtering. For the particular case of Mo sputtering by D^+ and B^{3+} ions, the threshold energies are 100 eV and 30 eV, respectively. Note that while the sputtering yield for a given incident ion energy is much greater for the incident B^{3+} ions than for the main ions, the B^{3+} ion fraction is typically 1% in the SOL plasma of Alcator C-Mod [20]. As a result, the sputtered influx of Mo atoms (Γ_{Mo}) from the surface is not always dominated by the species that induces the highest sputtering yield.

The incident ion energy E_i determines the amount of physical sputtering of the PFCs. E_i of the incident plasma ions is a sum of several components, see Equation 1.15:

$$E_i = E_{Ti} + E_{pre-sheath} + E_{sheath}, \tag{1.15}$$

where E_{Ti} is the thermal energy of the incident ions, $E_{pre-sheath}$ is the energy gain of the incident ions in the pre-sheath plasma region, and E_{sheath} is the energy gain of

the incident ions as they traverse the plasma sheath.

The thermal energy deposited by incident ions with a Maxwellian distribution is $E_{Ti} = 2T_i$ [20], where T_i is the ion temperature. If direct ion temperature measurements are not available, it is commonly assumed that $T_i = T_e$ [20]. The second component of the incident ion energy in Equation 1.15 is the ion energy gain across the pre-sheath region of the plasma. This component is a consequence of the Bohm sheath criterion [21], which requires that the main ion species enters the sheath region at its sound speed (c_s): $E_{pre-sheath} = 0.5 M_i c_s^2 = T_e$ [21].

If no direct measurements are available, the ion energy gain across the sheath region of the plasma is often estimated based on a well-established model of the plasma sheath. For example, in Ohmic plasmas the voltage drop across the plasma sheath (V_s) is often approximated (assuming $T_i = T_e$ and negligible secondary electron emission) as $|V_s| \approx 3T_e/e$, where T_e is in units of [eV] [21]. Therefore, the energy gain of incident ions of charge Z_i across the sheath is approximately $E_{sheath} = 3Z_i T_e$.

In the previous subsection we saw that in order to successfully couple ICRF power to the plasma core, the structure of the ICRF antenna/launcher needs to be as close as possible to the plasma, yet avoid deleterious plasma-antenna interactions. Experimentally, it is found that the close proximity of the core plasma to an active ICRF launcher results in a number of deleterious effects on the plasma and the plasma facing components (PFCs) through modifications of plasma-material interactions (PMIs). On Alcator C-Mod it is found that in ICRF-heated discharges sputtering of molybdenum (Mo) PFCs is enhanced and core Mo impurity contents scale with injected ICRF power [22, 23]. This high-Z impurity accumulation in the core plasma leads to the degradation of plasma fusion performance [24]. Additionally, ICRF-enhanced plasma-material interactions are suspected to cause high erosion of plasma-facing components on Alcator C-Mod [25]. JET's experience with high-Z (tungsten (W)) plasma facing components and ICRF heating shows that, for a given level of injected power, ICRF-heated plasmas suffer from higher core W levels compared to neutral beam heated plasmas [27]. Tore Supra's investigation of ICRF power effects on PMIs show that active ICRF antenna limiters experience a modification of the PMIs in

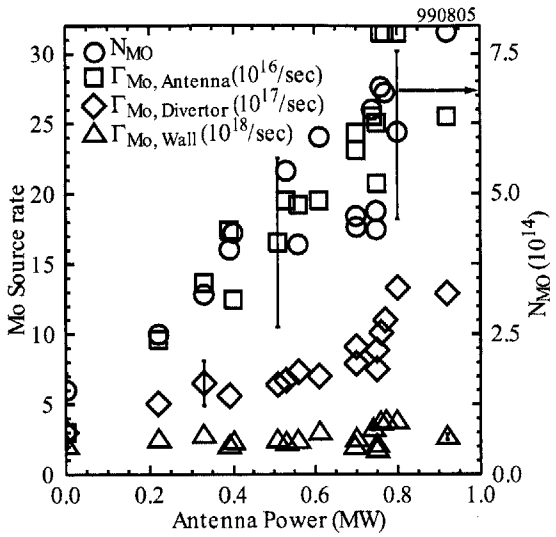

Figure 1-7: Variation of Mo source rates with ICRF power for a series of discharges at the average core plasma density $n_e \approx 2 \times 10^{20}\ m^{-3}$. Reproduced from [23].

the form of "hot spots" forming on the active antenna limiter tiles and the Faraday screen rods [26]. ASDEX Upgrade's investigation of its plasma performance in ICRF-heated discharges with W PFCs shows a result similar to JET's: for a given level of injected power ICRF-heated discharges contain higher concentration of core W impurities than neutral beam heated plasmas [28]. ASDEX Upgrade also observes that ICRF-heated discharges that use antennas with boron coated limiter tiles contain less core W impurities than discharges heated with antennas that use bare W limiter tiles [28].

For the particular case of Alcator C-Mod we find that both sputtering of plasma facing Mo surfaces and accumulation of Mo impurities in the plasma core (N_{Mo}) increase with the level of launched ICRF power [22, 23]. This result is shown in Figure 1-7. Figure 1-7 reveals that the ICRF enhancement of sputtering is non-uniform on Alcator C-Mod with different PFC areas contributing differently to the core Mo contents. The accumulation of core Mo impurities eventually leads to the degradation of the core plasma performance through increased line radiation power losses [24].

Enhanced plasma potentials (Φ_P) on open magnetic field lines in the boundary

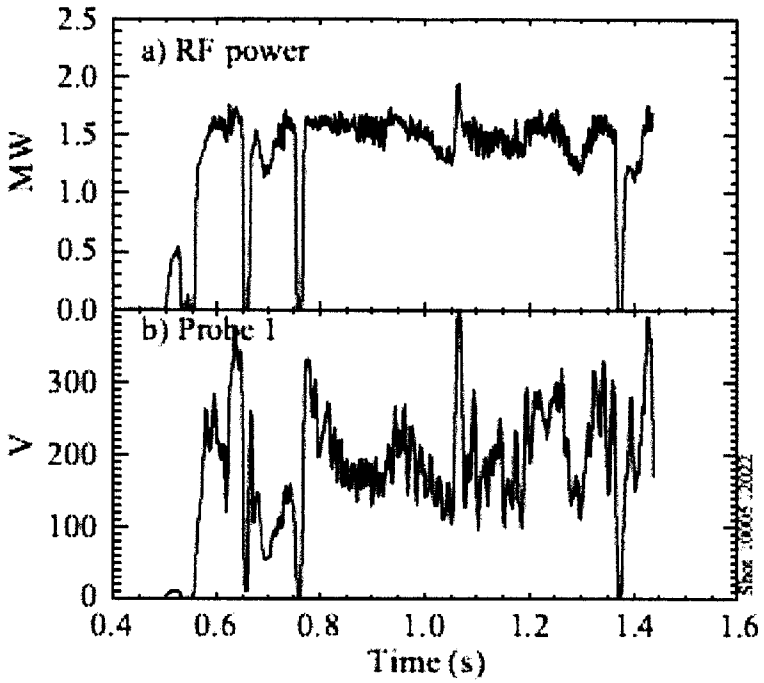

Figure 1-8: Example of variation of plasma potential in a single discharge. (a) the launched ICRF power and (b) the plasma potential. Reproduced from [23].

SOL plasma region are a leading suspected cause of the enhanced PMIs observed in ICRF-heated discharges in tokamaks. Φ_P enhancement of several hundred volts has been measured in the SOL plasmas of Alcator C-Mod in the presence of ICRF power [23, 29]. This result is shown in Figure 1-8. Note from Figure 1-6 that plasma potentials of greater than 100 V are sufficient to lead to significant sputtering of Mo PFCs by incident D^+ ions. It is generally believed that the electric field component of the ICRF waves begins to modify the voltage drop across the plasma sheath [30], i.e. the ion energy gain across the sheath is no longer given by $E_{sheath} = 3Z_iT_e$ in the presence of ICRF waves. Previous studies of ICRF wave absorption on Alcator C-Mod do reveal that electro-magnetic fields in the ICRF frequency range with the fast wave polarization are present in the low plasma density boundary regions, see Figure 1-9 [31]. However, a direct link between ICRF wave fields and plasma potential enhancement on Alcator C-Mod has yet to be experimentally demonstrated.

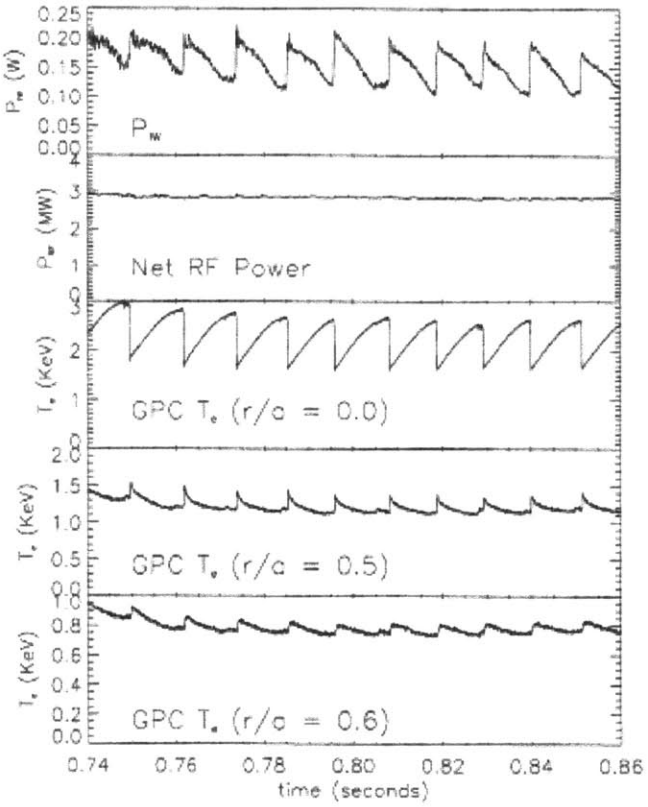

Figure 1-9: Example of variation of fast wave power in a single discharge. P_{IW} refers to the $\dot{B}$ probe mounted on the inner wall of Alcator C-Mod. T_e are the core electron temperature values at various flux surfaces. Reproduced from [31].

1.3 Thesis goals and objectives

As we saw in the previous subsection, ICRF heating of tokamak plasmas leads to a number of deleterious modifications of PMIs. Specifically, for the case of Alcator C-Mod we observe that sputtering of various PFC areas is enhanced in ICRF-heated discharges. The enhancement of the plasma potential to values greater than 100 V is implicated as the leading cause of the increased PFC erosion. The current speculation is that the ICRF wave electric fields are responsible for generating high plasma potentials in the SOL and probe measurements do reveal the existence of electro-magnetic fields in the ICRF frequency range in the SOL of ICRF-heated discharges on Alcator C-Mod. However a direct link between the ICRF waves and the enhanced plasma potential has yet to be demonstrated on Alcator C-Mod.

The main goal of this thesis is to determine what aspects of the launched ICRF power influence the plasma potential enhancement measured in the SOL of ICRF-heated plasmas on Alcator C-Mod. The key questions are: what is the correlation between local ICRF wave fields and plasma potential enhancement? Is the enhancement governed by local plasma parameters or does it depend on core plasma properties? Is ICRF enhancement of the plasma potential local to the active antenna or does it also take place non-locally? A secondary objective is to explore what effects these enhanced plasma potentials can have on plasma-material interactions in tokamak plasmas. Can ICRF-enhanced plasma potentials account for the observed modifications in PMIs on Alcator C-Mod? How can we minimize the effect of ICRF power on plasma-material interactions?

In order to answer these questions the existing diagnostics on Alcator C-Mod require an extensive upgrade. The plasma potential measurements need to be carried out over a more extensive spatial coverage to determine how localized with respect to the active antenna the enhancement is. A new plasma potential measuring technique needs to be developed to measure the potentials in the high plasma density regions of the SOL. Radially scanning probes need to be installed to determine the cross-field plasma potential profiles. Localized simultaneous measurements of the plasma

potential and the ICRF wave fields need to be carried out to determine what role (if any) the ICRF power plays in enhancing the plasma potential in the SOL regions. A detailed description of the relevant diagnostic tools and techniques used for our study is provided in the following section.

Chapter 2

Diagnostics description: methods and techniques

In order to determine the underlying mechanisms that control plasma potential enhancement on open magnetic field lines in the SOL of ICRF-heated discharges on Alcator C-Mod, a number of diagnostics were used to quantify critical local plasma parameters. The primary diagnostics include: 1) Langmuir probes for local plasma density (n_e) and electron temperature (T_e) measurements; 2) emissive probes for local plasma potential (Φ_P) measurements; 3) $\dot{B}$ probes for local ICRF wave field measurements; and 4) ion sensitive probes (ISPs) for Φ_P measurements in high n_e plasma regions inaccessible to emissive probe measurements. In the following sections we are going to introduce the four probes and describe their principles of operation.

2.1 Langmuir probes

One of the simplest and most robust methods to diagnose the boundary plasmas are Langmuir probes [32, 33]. The probe, which is an electrically isolated conductor (typically molybdenum (Mo) or tungsten (W) metals) is physically inserted into the plasma. An electric current is measured ($I_{Langmuir\ Probe}$) as a function of the voltage applied to the probe surface ($V_{Langmuir\ Probe}$), hence, the plot of I vs. V is often referred as the I-V curve of a Langmuir probe, see Figure 2-1. In Figure 2-1 I_{sat}

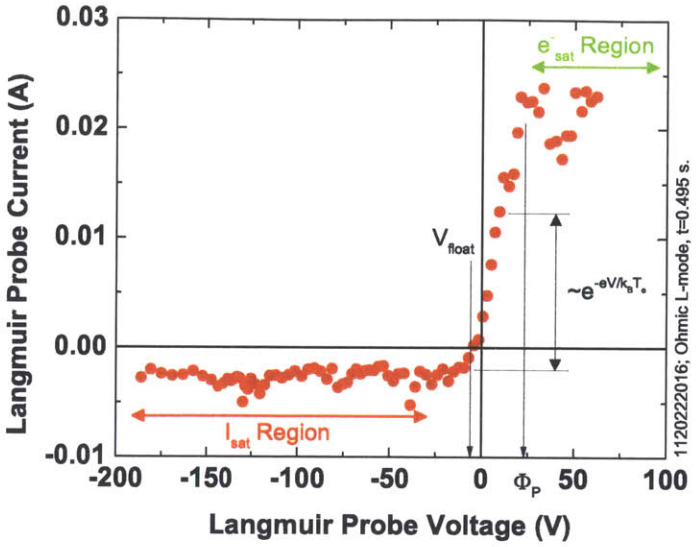

Figure 2-1: A typical I-V curve obtained in an Ohmic L-mode discharge on Alcator C-Mod in the vicinity of a limiter plasma facing surface. The voltage is referenced with respect to the grounded vacuum vessel.

refers to the ion saturation current obtained when the probe voltage is much lower than the plasma potential Φ_P. The I_{sat} operating region corresponds to the condition when the vast majority of electrons are energetically disallowed from being collected. V_{float} refers to the probe floating potential, the potential at which the probe current is zero. e^-_{sat} refers to the electron saturation current obtained when the probe voltage is greater than Φ_P. The e^-_{sat} operating region corresponds to the condition when the electrons are no longer repelled by the probe bias and any further increase in the applied voltage only affects the energy of the collected electrons but not their current [33]. The electron temperature T_e is responsible for the exponential I-V dependence of the curve between the I_{sat} and e^-_{sat} regions. k_B is the Boltzmann constant T_e is in units of eV.

Accounting for the sheath that forms between the bulk plasma and the probe surface allows us to estimate two fundamental local plasma properties, n_e and T_e, from the I-V curve. The electron temperature is obtained by fitting an exponential function to the part of the I-V curve bounded by the I_{sat} and e^-_{sat} regions: $(I_{probe} - I_{sat}) \sim e^{-\frac{eV_{probe}}{k_B T_e}}$. An alternative method is to take $\ln(I_{probe} - I_{sat})$: the electron temperature

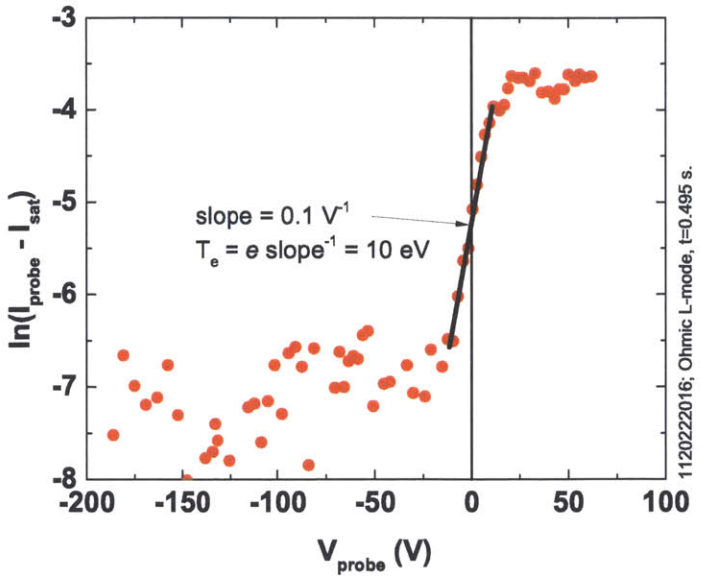

Figure 2-2: Determination of the electron temperature from the I-V plot of a Langmuir probe. The data is from Figure 2-1.

is the inverse of the slope of the linear region between the ion saturation and the electron saturation regions [32, 33] as demonstrated in Figure 2-2.

The electron temperature, in turn, determines the ion sound speed (c_s) in the plasma [34]:

$$c_s = 1 \times 10^4 \sqrt{\frac{\gamma Z T_e}{\mu}}, \tag{2.1}$$

where γ is the adiabatic index, Z the ion charge state, and μ is the ion mass in the units of the proton mass. Once we know the ion sound speed, the plasma density is measured from the I_{sat} value according to Equation 2.2:

$$n_e = \frac{I_{sat}}{0.5 q_e c_s A_{probe}}, \tag{2.2}$$

where q_e is the magnitude of the electron charge, and A_{probe} is the probe area that is perpendicular to the background magnetic field. For the example shown in Figure 2-1 we find: $V_{float} \sim -5\ V$ and $T_e \sim 10\ eV$. Accounting for the probe area perpendicular to the magnetic field ($A_{probe} = 7.5 \times 10^{-7}\ m^2$) we find that $n_e \sim 2 \times 10^{18}\ m^{-3}$.

According to the standard Langmuir probe theory [32, 33], the plasma potential can also be estimated as: $\Phi_P = V_{float} + 3T_e/e$, which is $\sim 25\ V$ for the case shown in Figure 2-1.

2.2 Emissive probes

The plasma potential (Φ_P) is the most important quantity to measure in understanding enhanced sheaths and sputtering of high-Z metals. The plasma potential is the DC electrostatic potential difference between the local quasi-neutral plasma and the surrounding "ground" of the plasma-facing components, thus setting to first order the incident ion energy at material surfaces. Emissive probes are routinely used to directly measure Φ_P in magnetized plasmas, including tokamak plasmas on Alcator C-Mod [23, 29], CASTOR [36], and Phaedrus-T [37].

When an electrically floating object is placed in a plasma a sheath potential drop develops between the plasma and the surface to enforce ambipolarity at the surface. In particular the sheath must electrostatically repel nearly all the plasma electrons, which have a much higher thermal velocity than the plasma ions. Therefore, the material's surface floating potential is set by a combination of the sheath potential and the plasma potential. However, if the surface actively emits electrons at a sufficient rate then it is possible to completely balance the incident electron flux density and the sheath potential drop will vanish. Thus the surface's floating potential will be equal to the plasma potential [38]. The electron emission is achieved by heating the probe to very high temperatures and the electron emission from the probe surface is given by the Richardson-Dushman equation [39]:

$$J_{e-} = A_G T^2 e^{-\frac{W_e}{k_B T}}, \tag{2.3}$$

where J_{e-} is the electron emission current density in units of $[\frac{A}{m^2}]$, A_G is the (material specific) Richardson emission constant units of $[\frac{A}{m^2 K^2}]$, T is the surface temperature in units of [K], W_e is the probe material work function in units of [eV], and k_B is the Boltzmann constant in units of $[\frac{eV}{K}]$. Equation 2.3 remains valid as long as the probe temperature remains below the melting temperature of the probe material, therefore, it is desirable to use an emissive filament with a very high melting temperature, such as tungsten (W). Once the probe electron emission flux becomes equal to or greater than the incident electron flux from the plasma, the probe begins to float at or near the

Material	A_G $[\frac{A}{m^2K^2}]$	W_e [eV]
Pure W	6.0×10^5	4.3-5.2
Thoriated W	3.0×10^4	2.6

Table 2.1: The Richardson emission constant and work function for pure and thoriated tungsten [15].

plasma potential [38]. The uncertainty between the floating potential of a hot emissive probe and the plasma potential is within $\sim \frac{T_e}{e}$ volts, where T_e is in [eV] [38]. It is common to use thoriated tungsten to decrease the work function and dramatically increase the emission current density for a given temperature. The values of the Richardson emission constant and the work function for pure and thoriated tungsten are listed in Table 2.1 [15].

Figure 2-3 shows a diagram of two emissive probe configurations commonly used in magnetized plasmas. The probe is usually a thin wire element with a very high melting temperature, typically tungsten. An aperture is used to expose only the hottest part of the filament to plasma: plasma exposure of the cold part of the filament and the supporting electrodes leads to underestimation of the plasma potential [40]. The element is heated ohmically by passing either DC or AC current through the filament: the electric current then determines the operating temperature of the probe. The DC current is the preferred heating method in a steady-state plasma device, while the AC current is favored in tokamaks where disruption-induced $\mathbf{J} \times \mathbf{B}$ forces may break a DC current-heated filament. Simplified DC and AC circuit diagrams used to heat the emissive filament and read out the floating potential of the filament are shown in Figure 2-4. The indicated output voltage readouts are approximately equal to the floating potential of the emissive filament and the error is determined by the voltage drop across the filament. The filament resistance is typically $< 1\ \Omega$ and the current value (either DC or root mean square (rms)) is typically 2-3 A; therefore, the error in the floating voltage estimate is typically 2-3 V.

A demonstration of how an emissive probe is used to determine the plasma potential in a magnetized plasma is shown in Figure 2-5. We used an emissive probe of design (b) as shown in Figure 2-3 and the probe filament (tungsten wire, diameter

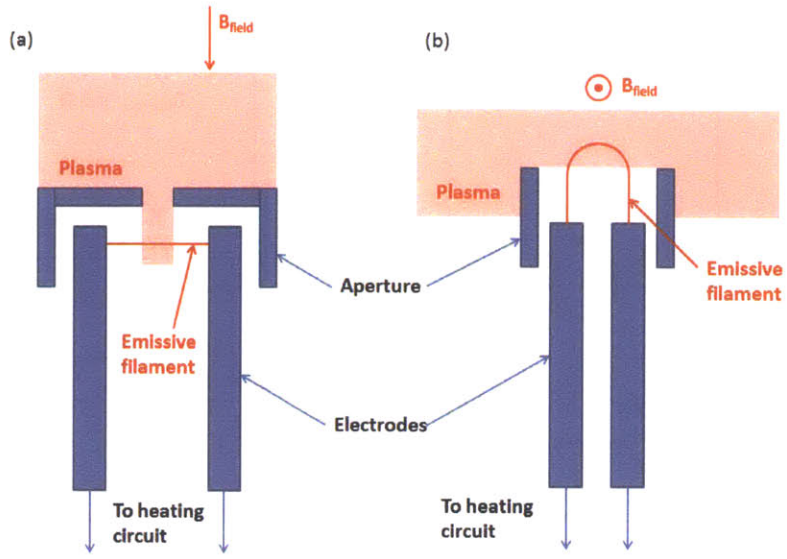

Figure 2-3: Common emissive probe configurations used for plasma potential measurements in magnetized plasmas. The orientation of the filament is perpendicular to the magnetic field.

$d_{wire} = 125\ \mu m$) was heated by a DC current source. The experiment was conducted in a magnetized linear helicon plasma device, DIONISOS, [55]. The plasma parameters were: argon main ion species (+1 charge state), $B = 0.04\ T$, $P_{Ar} = 0.21\ Pa$, $P_{RF\ source} = 300\ W$, $T_e = 10\ eV$, $n_e = 4 \times 10^{16}\ m^{-3}$. Note the sudden transition in the probe floating potential when the DC current through the probe filament exceeds 2 A. Before the transition, the floating potential is approximately -5 V and remains approximately independent of the current through the filament. After the transition the floating potential becomes 35-40 V and also remains independent of the current through the filament. The transition between the two floating voltage regimes happens when the electron flux emitted by the probe surface is equal to the electron flux incident from the plasma. As the current through the filament (and, hence, its temperature and electron emission) is increased past the transition point, the *net* electron collection at the surface remains unchanged: any excess emitted electrons are reflected back to the surface to preserve the ambipolarity condition. Once the floating potential of the emissive probe saturates and becomes independent of the probe surface temperature, we reach the condition where the probe floating potential

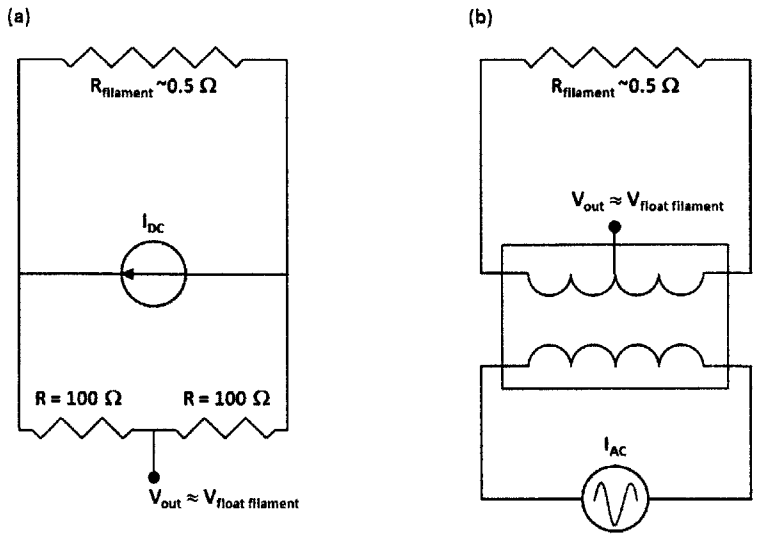

Figure 2-4: Simplified diagrams for (a) DC and (b) AC circuits used to heat an emissive filament and read out the floating potential of the filament.

becomes approximately equation to the plasma potential. For our specific case we have $\Phi_P = 35 - 40\ V$.

Equation 2.3 shows that the electron emission current density is determined by the operating temperature of the emissive filament, which, for our probe design, is a function of the current (either DC or rms) through the filament. Figure 2-6 shows the electron emission current density and the corresponding maximum allowable plasma density at which the probe can still operate as a plasma potential diagnostic. The estimated curves in Figure 2-6 are plotted for $T_e = 10\ eV$ and $T_e = 100\ eV$, which is a typical electron temperature range in the SOL tokamak plasmas [14]. The maximum allowable plasma density $n_{e,\ max}$ is given by Equation 2.4:

$$n_{e,\ max} = \frac{J_{e-}}{0.25 q_e v_{e,\ th}}, \tag{2.4}$$

where $v_{e,\ th}$ is the electron thermal speed [34]:

$$v_{e,\ th} = 4.2 \times 10^5 \sqrt{T_e}\ [m/s]. \tag{2.5}$$

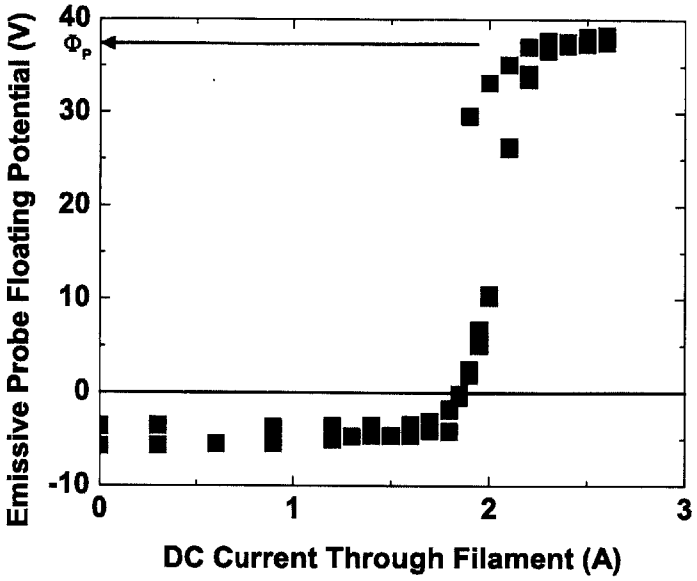

Figure 2-5: The floating potential of an emissive probe filament as a function of the DC current through the filament. The plasma potential is taken as the floating potential when the floating potential saturates and becomes independent of the current through the filament.

We see that the filament temperature needs to be in the range of 2000-2200 K for the emissive probe to function as a plasma potential diagnostic in the SOL plasma in the vicinity of an ICRF antenna, i.e. $n_e \leq 1 \times 10^{18}\ m^{-3}$ and $T_e = 10\ eV$. A more detailed design of the emissive probes implemented on Alcator C-Mod is provided in the following chapter.

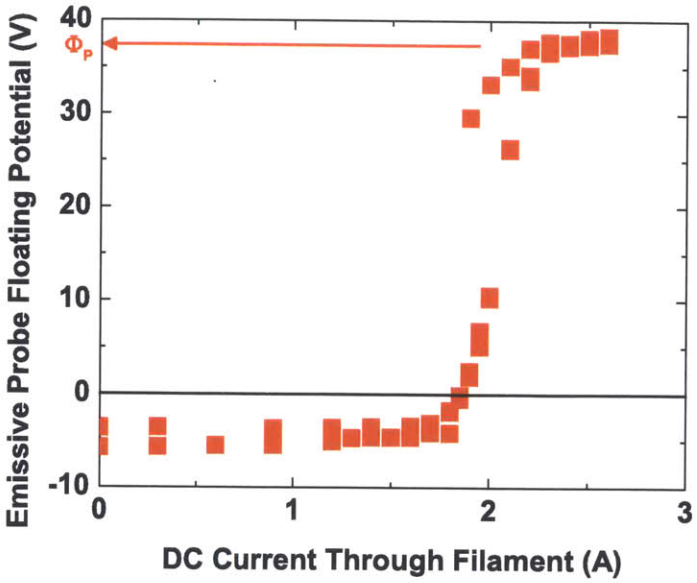

Figure 2-5: The floating potential of an emissive probe filament as a function of the DC current through the filament. The plasma potential is taken as the floating potential when the floating potential saturates and becomes independent of the current through the filament.

We see that the filament temperature needs to be in the range of 2000-2200 K for the emissive probe to function as a plasma potential diagnostic in the SOL plasma in the vicinity of an ICRF antenna, i.e. $n_e \leq 1 \times 10^{18}\ m^{-3}$ and $T_e = 10\ eV$. A more detailed design of the emissive probes implemented on Alcator C-Mod is provided in the following chapter.

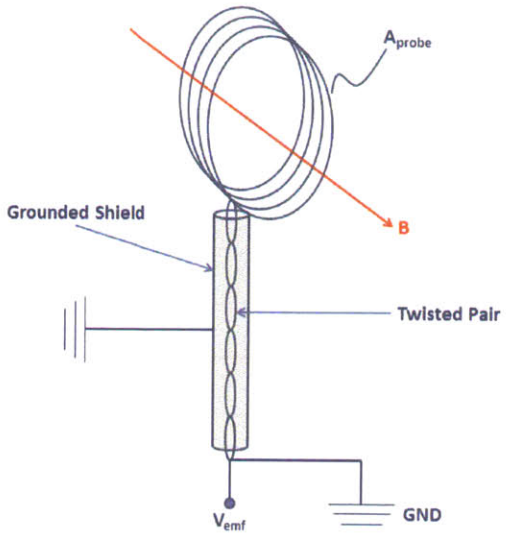

Figure 2-7: A diagram that shows key components of a $\dot{B}$ probe. A_{probe} is the area enclosed by the probe. B is the magnetic field component normal to the area enclosed by the probe. V_{emf} is the EMF voltage. GND is the ground.

2.3 $\dot{B}$ probes

$\dot{B}$ probes are commonly employed in tokamaks to measure time varying magnetic fields [31, 32, 41]. The nature of the measured quantity is implied in the name "B-dot", where the dot symbol refers to the time derivative of the quantity under the dot. The probe consists of one or more loops of a conducting wire, see Figure 2-7, and relies on Faraday's Law for operation [32]:

$$V_{emf} = -N A_{probe} \frac{dB}{dt}, \tag{2.6}$$

where V_{emf} is the electromotive force (EMF) voltage, N is the number of wire loops, A_{probe} is the area enclosed by the wire loop that is perpendicular to the magnetic field, and $\frac{dB}{dt}$ is the time derivative of the magnetic field within the area enclosed by the probe. Integrating the induced V_{emf} signal either digitally or through an integrating circuit allows us to reconstruct the magnetic field signal from its time derivative.

Since we are interested in using $\dot{B}$ probes to detect B fields oscillating at the ICRF

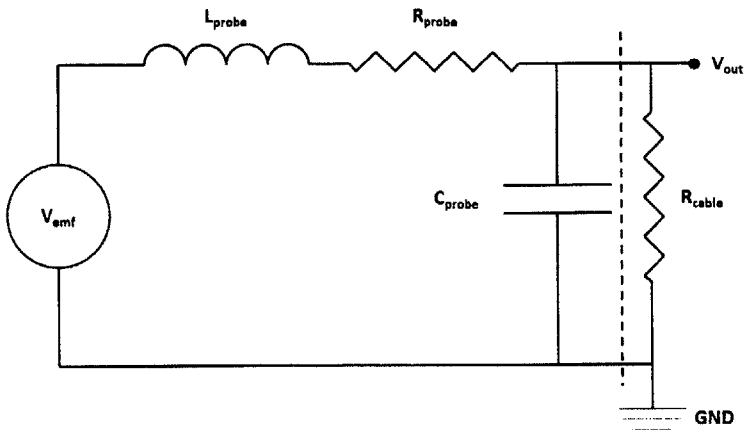

Figure 2-8: A lumped-element circuit used to analyze the response of a $\dot{B}$ probe to an oscillating RF wave.

frequency (50-80 MHz) with the wave length much larger than the probe dimension, we can use a lumped-element circuit approach to determine the probe RF response [41]. Figure 2-8 shows a lumped-element circuit diagram used to analyze the $\dot{B}$ probe response.

The probe voltage output (V_{out}) is related to V_{emf} for a sinusoidally oscillating B field according to Equation 2.7 [41]:

$$V_{out} = \frac{V_{emf}e^{i\theta}}{[(1-\omega^2 L_{probe}C_{probe} + \frac{R_{probe}}{R_{cable}})^2 + (\omega R_{probe}C_{probe} + \frac{\omega L_{probe}}{R_{cable}})^2]^{1/2}}, \tag{2.7}$$

where ω is the angular frequency of the ICRF wave, L_{probe} is the probe self-inductance, C_{probe} is the probe capacitance, R_{probe} is the probe RF resistance, R_{cable} is the cable/load resistance, and θ is the phase shift [41].

$$\theta = tan^{-1}\left[\frac{\omega R_{probe}C_{probe} + \frac{\omega L_{probe}}{R_{cable}}}{1-\omega^2 L_{probe}C_{probe} + \frac{R_{probe}}{R_{cable}}}\right]. \tag{2.8}$$

Equations 2.7 and 2.8 may be approximated as:

$$V_{out} \approx \frac{V_{emf}e^{i\theta}}{[1+(\frac{\omega L_{probe}}{R_{cable}})^2]^{1/2}} \tag{2.9}$$

and

$$\theta \approx tan^{-1}\left[\frac{\omega L_{probe}}{R_{cable}}\right] \tag{2.10}$$

provided that the circuit elements satisfy the following conditions: $R_{probe} \ll R_{cable}$, $\omega \ll \omega_{c,\ LC} \equiv \frac{1}{\sqrt{L_{probe}C_{probe}}}$, and $\omega \ll \omega_{c,\ RC} \equiv \frac{1}{R_{probe}C_{probe}}$. The last two relations place a constraint on the values of the probe capacitance and inductance: $C_{probe} \ll \frac{1}{\omega R_{probe}}$, and $C_{probe} \ll \frac{1}{\omega^2 L_{probe}}$. A more detailed design of the $\dot{B}$ probe implemented on Alcator C-Mod is provided in the following chapter.

2.4 Ion sensitive probes

In Section 2.2 we mentioned that, for the case of high density plasmas, emissive probes can no longer supply enough electrons to overcome the electron flux incident from the plasma on the probe surface. As a result, emissive probes no longer float at the plasma potential. This shortcoming and a short lifetime of emissive probes in tokamak plasmas served as a motivation to explore other, more robust probes for plasma potential measurements in the SOL plasmas of Alcator C-Mod. Ion sensitive probes (ISPs), which are sometimes called Katsumata, plug, or baffle probes [42, 43], overcome these two shortcomings.

Since the original work by Katsumata in the 1960's [42], ISPs have been extensively studied and applied in magnetized plasmas. Examples of various iterations of the ISP use are: 1) ion temperature measurements in the Large Helical Device (LHD) divertor [44]; 2) ion temperature measurements in the boundary plasma of the JFT-2M tokamak [45]; 3) ion temperature measurements in the linear plasma device PSI-2 [46]; 4) plasma potential measurements on the CASTOR tokamak [47, 48]; 5) ion temperature measurements in the scrape-off layer (SOL) of ASDEX Upgrade [49]; 6) plasma potential measurements in a magnetized Q-machine [50]; 7) perpendicular ion temperature in the MIX 1 mirror machine [51]; 8) plasma potential in the linear helicon plasma device DIONISOS [52]; 9) plasma potential in the SOL of Alcator C-Mod [53]; and 10) ion temperature distribution in DIONISOS [54].

The ISP was studied extensively at MIT's Plasma Science and Fusion Center on a linear magnetized plasma device, DIONISOS [55, 52] (Figure 2-9) to determine its applicability as a plasma potential diagnostic. The magnetic field was a constant $B = 0.04\ T$ and the working gas was argon at neutral gas pressure $P_{Ar} = 0.26\ Pa$. The RF source was a 3 kW Apex 3013 RF generator from Advanced Energy and the RF power was coupled to the plasma via a Nagoya III antenna [56] through a matching network. The operating RF frequency was 13.56 MHz. The plasma density ranged from $\sim 1 \times 10^{16}\ m^{-3}$ in the low density regime to $\sim 1 \times 10^{18}\ m^{-3}$ in the high density helicon mode. The diameter of the extracted plasma column was 5

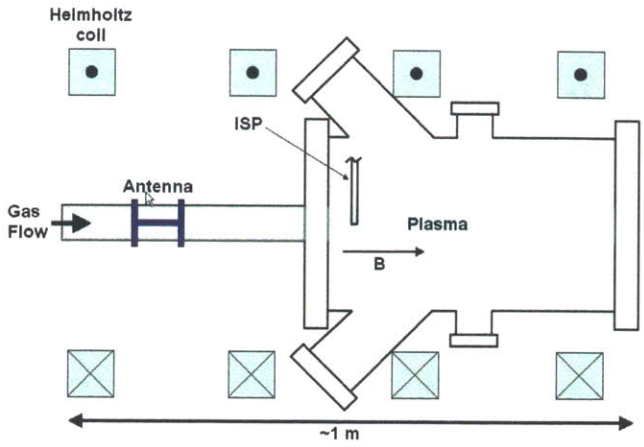

Figure 2-9: A schematic of the DIONISOS experiment [55].

cm. The electron temperature ranged from 7 eV in the helicon mode to 10-15 eV in the lower density modes, implying that the electron gyro-radius was $\sim 0.2\ mm$. The helicon mode required incident RF power (P_{RF}) to be greater than 1200 W. The basic plasma parameters (T_e and n_e) in DIONISOS plasma are plotted as a function of injected RF power in Figure 2-10. The plasma potential in the DIONISOS plasma was independently measured with a hot floating emissive probe at the same location and plasma conditions as the ISP measurements.

Key components of the ISP are shown in Figure 2-11: these are the probe wall and collector electrodes electrically isolated from each other by a series of insulators. The collector is recessed behind the probe entrance by a distance h, which is comparable to the ion gyroradius of the main plasma species. The probe entrance was positioned at the center of the plasma column with the collector surface aligned parallel to the magnetic field.

We are now going to outline a novel technique that we developed to measure the plasma potential in magnetized high density plasmas with an ISP [52]. The plasma potential can be determined by examining a current-voltage (I-V) characteristic of the probe collector as a function of the wall (not the collector) potential. In the simplest picture no ion is electrostatically allowed to enter the probe volume once the

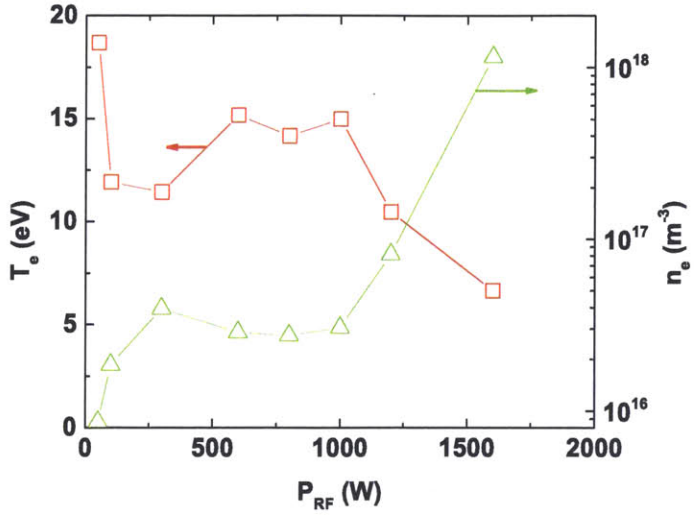

Figure 2-10: Electron temperature (T_e) and plasma density (n_e) in DIONISOS as a function of injected RF power (P_{RF}).

wall potential is raised above the plasma potential, therefore, Φ_P can be determined as the wall potential at which the collected current vanishes. Figure 2-12 shows two typical I-V curves (the positive current corresponds to the electron collection) where the wall and the collector were both swept simultaneously with a constant bias ($V_{BIAS} = V_{WALL} - V_{COLL}$) between them. The plasma potential, determined by the emissive probe, was ~15 V. The collector current remains in the ion collection regime at all times when the bias voltage is positive ($V_{WALL} > V_{COLLECTOR}$) by 5-10 V. The current drops to zero once the wall potential is raised above the plasma potential and the ions are no longer electrostatically allowed to enter the probe volume. If the bias voltage is negative ($V_{WALL} < V_{COLLECTOR}$) one often measures substantial electron current for $V_{WALL} < \Phi_P$, but which also goes to zero when $V_{WALL} > \Phi_P$. Note that the electron current far exceeds the e^- current expected from the classical gyromotion as the collector recess distance h is typically tens of electron gyroradii. A more detailed examination of the key I-V features of the ISP is provided later in this section. Using this technique, we verified Φ_P measurements against emissive probe results in DIONISOS over a wide range of densities and plasma regimes (Figure 2-13). The main source of error in the ISP measurements is due to the uncertainty of the

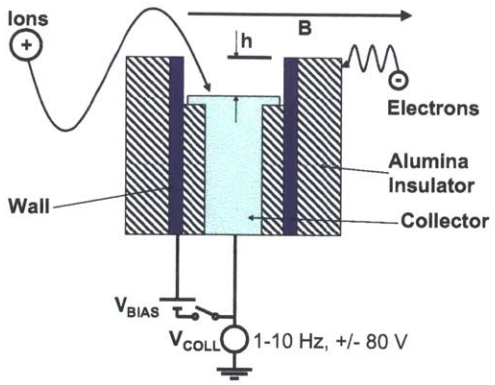

Figure 2-11: A schematic of the ISP used on DIONISOS. h = recess height; solid - conductor, hashed - insulator; cylindrical symmetry.

"knee" location in the collected current in the vicinity of $V_{WALL} = \Phi_P$. The width of the knee is typically ~5 V, meaning that the plasma potential measurements between the two probes are in good agreement.

We further examine the ion and electron saturation currents on the probe collector at fixed wall voltages. Figure 2-14 shows several I-V curves at four different constant wall voltages: V_{WALL} = -20, -10, +10, and +25 V. The I_{sat} and $I_{e-\ sat}$ regions are also shown. We observe that both the ion and electron saturation currents drop to zero once the wall voltage exceeds the plasma potential (Figure 2-15). This result is consistent with the results in Figure 2-12. Note that the maximum measured electron current far exceeds the current expected from a simple gyro-motion of the electrons – the recess distance of the collector is tens of electron gyroradii, yet the electron current remains much greater than the ion current. It is sometimes speculated in the literature that the source of the electrons at the collector surface is due to secondary electron emission from the wall [51]. However, our results show that the electron collection disappears for $V_{WALL} \geq \Phi_P$ and $I_{WALL} = I_{e-\ SAT}$, i.e. at the maximum primary electron flux to the wall, implying that the source of the electrons is not secondary emissions from the wall.

The high ($> 1\ mA$) measured collector I_{sat} current in the ISP appears to exceed the maximum allowed space-charge limited current if only ions exist in the probe volume [57, 58]. A 1-D estimate of the Child-Langmuir current limit (I_{CL}) is given

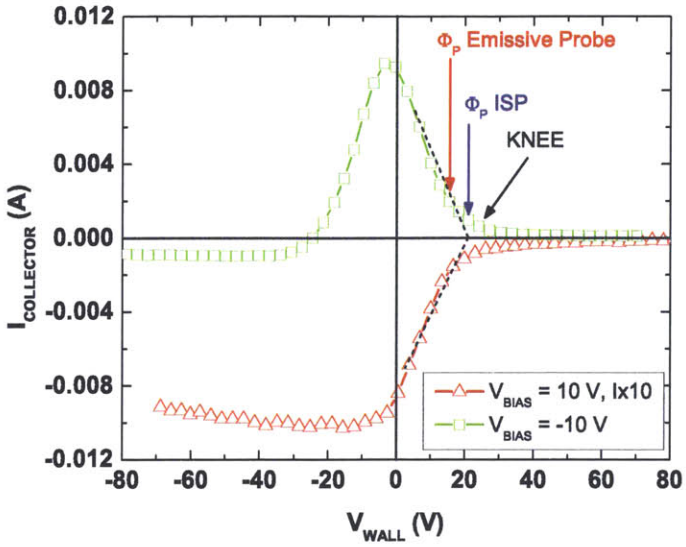

Figure 2-12: ISP collector current as a function of the wall potential for two cases: $V_{WALL} > V_{COLLECTOR}$ (red triangles), and $V_{WALL} < V_{COLLECTOR}$ (green squares). The positive current corresponds to the electron collection. $P_{RF} = 1600\ W$, $h = -5\ mm$.

by Equation 2.11:

$$I_{CL} = A\frac{4\epsilon_o}{9}\frac{(\Phi_P - V_{COLLECTOR})^{3/2}}{h^2}\sqrt{\frac{2q_i}{m_i}} \tag{2.11}$$

where A is the collector area, ϵ_o is the permeability of free space, q_i is the particle charge state, and m_i is the particle mass. For the DIONISOS case of singly charged argon ions (atomic mass 40) collected between a potential difference of 40 V, over a distance of 5 mm, and collected over a circular electrode of 5 mm in diameter gives $I_{CL} \sim 1.7\ \mu A$. The estimated I_{CL} value is three orders of magnitude lower than the measured collector I_{sat} current. The Child-Langmuir current limit is enhanced by treating the problem in 2 dimensions and by considering the non-zero velocity of the ions [59, 60], however, the total enhancement in $I_{COLLECTOR}$ due to these effects is still less than one order of magnitude. It seems necessary to involve electrons in the probe volume, perhaps by $\mathbf{E} \times \mathbf{B}$ drift, to explain the results. Such a mechanism is outlined below.

The classical principle of operation of the ISP probe is based on the large difference

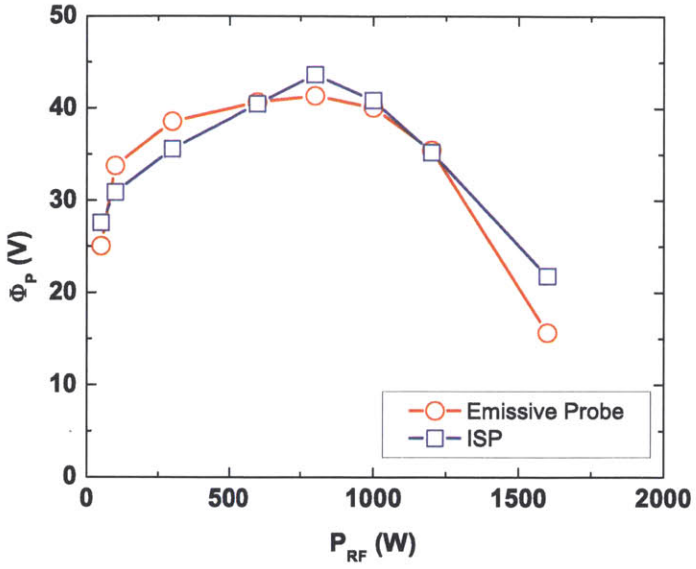

Figure 2-13: Comparison of plasma potential measurements between ISP and emissive probe in DIONISOS as a function of RF power.

between the electron and ion larmor radii ($\rho_{ion}/\rho_{e-} \sim 50$ in deuterium main ion plasmas with equal ion and electron temperatures) in magnetized plasmas. With the plasma facing surface normal of the collector oriented perpendicular to the background magnetic field, as shown in Figure 2-11, the collector current due to electrons ($I_{e-\ sat}$) is significantly reduced as the collector recess distance h becomes greater than $\sim 10\rho_{e-}$. A point is reached when $I_{e-\ sat}$ becomes equal to the collector current due to ions I_{sat} and, in this case, the floating potential of the collector is taken as being equal to the plasma potential. However, experimentally it is found that in most cases $I_{e-\ sat} > I_{sat}$ even for $h \sim \rho_{ion} \gg 10\rho_{e-}$ [47, 48, 52] and the floating potential of the recessed collector shows little dependence on h. In fact, the current collection in the ISP is consistent with the $\mathbf{E} \times \mathbf{B}$ drift of electrons inside the volume bounded by the wall, the collector, and the surrounding plasma [61]. These drifts follow equipotential surfaces inside the probe volume and, depending on the voltage difference between the wall, the collector, and the plasma, may allow for electron collection on surfaces where $h \gg 10 \times \rho_{e-}$, see Figure 2-16. When the wall voltage is below the plasma potential, ions are electrostatically allowed to enter the ISP volume and the net positive charge

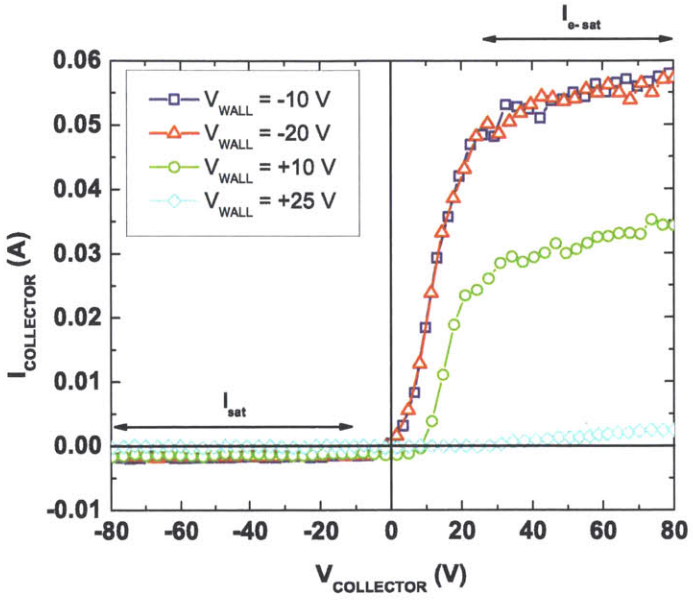

Figure 2-14: ISP collector current as a function of the collector potential at four different constant wall potentials. $P_{RF} = 1600\ W$, $h = -5\ mm$.

accumulation results in an electric field that induces $\mathbf{E} \times \mathbf{B}$ drifts toward the collector surface, as depicted in Figure 2-16 (a). Depending on the collector voltage, either ions or electrons are collected by the collector electrode. The I_{sat} collector current that far exceeds the Child-Langmuir limit is also consistent with the $\mathbf{E} \times \mathbf{B}$ electron drift inside the ISP volume, as the electrons neutralize the positive ion charge and reduce the effective distance h in Equation 2.11 across which bare positive charges must travel. [61]. However, when the wall voltage is above the plasma potential, no ions are allowed to enter the ISP volume and, hence, the resulting electric field structure no longer supports the $\mathbf{E} \times \mathbf{B}$ drifts needed for the electrons to reach the collector surface. This case is depicted in Figure 2-16 (b) and now neither ions nor electrons can reach the collector.

Note that the development of the ISP as a plasma potential diagnostic on DION-ISOS was followed by an extensive use of the probe on Alcator C-Mod to study plasma potentials in Ohmic [61, 62] and ICRF-heated discharges [53]. A more detailed design of the ISP implemented on Alcator C-Mod is provided in the following chapter.

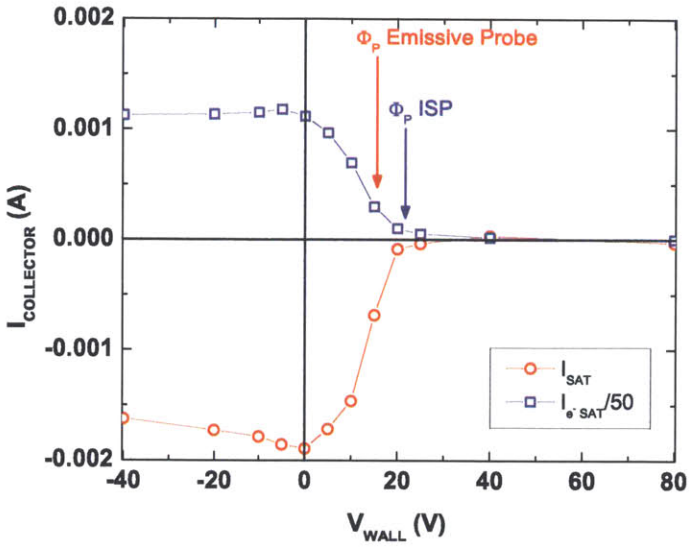

Figure 2-15: ISP ion and electron saturation currents as a function of the wall potential. $P_{RF} = 1600\ W$, $h = -5\ mm$.

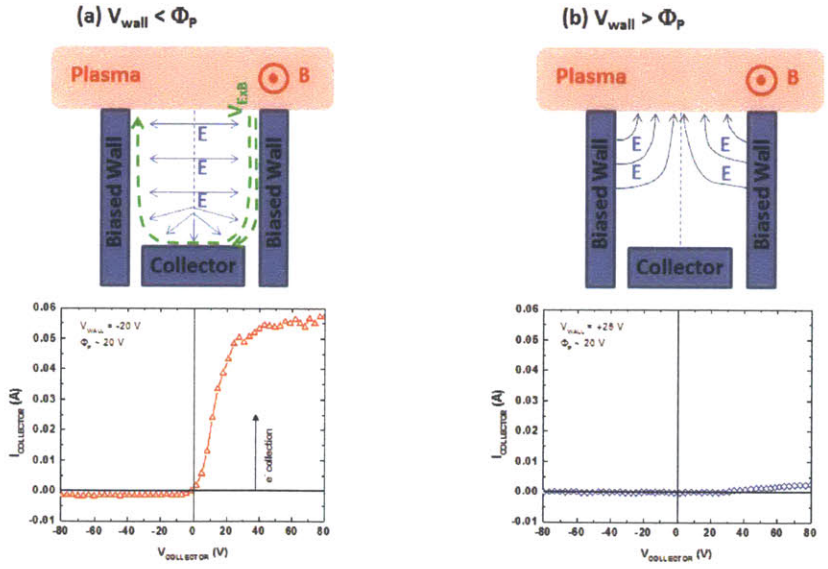

Figure 2-16: A diagram that shows ISP's principle of operation in two different regimes: (a) when $V_{wall} < \Phi_P$ and (b) when $V_{wall} > \Phi_P$.

Chapter 3

Diagnostics description: implementation on Alcator C-Mod

Various combinations of the primary diagnostics, described in the previous section, were mounted on two radially (along the major radius direction R) scanning probes, the Surface Science Station (S^3) and the A-port Scanning Probe (ASP), and several stationary probe stations on the sides of the A-B split limiter. Additionally, several secondary diagnostics were used in conjuction with the primary diagnostic sets to quantify the effects of ICRF power on Φ_P enhancement. A fish eye view of Alcator C-Mod is shown in Figure 3-1.

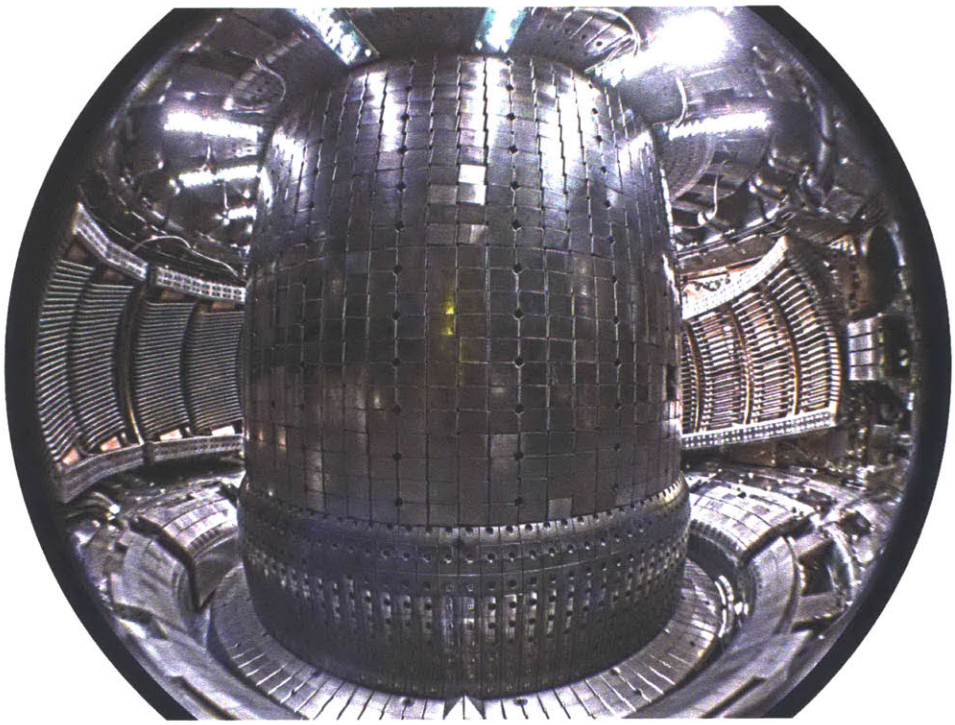

Figure 3-1: A fish eye view of Alcator C-Mod. The image was taken from the horizontal B-port. Image courtesy of Michael Garrett.

3.1 Alcator C-Mod tokamak

Alcator C-Mod is a medium size tokamak, which utilizes very high toroidal magnetic fields (up to 9 T) to confine its plasma. C-Mod's on-axis major radius (R_o) is 0.67 m, its minor radius (a) is 0.22 m, its standard on-axis toroidal field is 5.4 T, and its standard plasma current is 1.0 MA [63]. C-Mod's plasma facing components (PFCs) are made entirely of high-Z molybdenum (Mo) tiles and the tokamak relies on boronization for wall conditioning [64]. The key in-vessel plasma facing structures are the inboard and outboard limiters and the lower and upper divertors. The tokamak can operate with a variety of plasma shapes, such as the lower single null (LSN), the inner wall limited (IWL), and the upper single null (USN) configurations. The key in-vessel plasma facing structures and the poloidal cross sections of typical plasma configurations are shown in Figure 3-2. The in-vessel structures themselves are armored with protective Mo tiles, the typical dimension of which is 2.5 $\times$ 2.5 cm^2. The individual tiles are clearly seen in Figure 3-1. A standard plasma discharge duration is typically 1-2 s followed by a period of 15-30 min between discharges. As a result of the short discharge duration and the much longer period between the discharges, it is sufficient for the Mo PFCs on Alcator C-Mod to rely only on inertial cooling to prevent PFC melting.

The in-vessel access is provided through ten port sections, with three ports in each section. The three ports in each section are: the horizontal port, the vertical port on the top of the vessel, and the vertical port on the bottom of the vessel. The ten port sections are label: "A", "B", "C", "D", "E", "F", "G", "H", "J", and "K". These are spaced 36^o apart toroidally. The top cross sectional view (at the midplane) of Alcator C-Mod is shown in Figure 3-3. The key in-vessel components and primary diagnostics are highlighted. The toroidal direction (ϕ) is referenced with respect to the middle of the A-port and the direction of increasing ϕ is clockwise as viewed from the top.

Auxiliary heating power is provided primarily by ICRF heating through three ICRF antennas: two two-strap antennas at the D and E ports and one four-strap

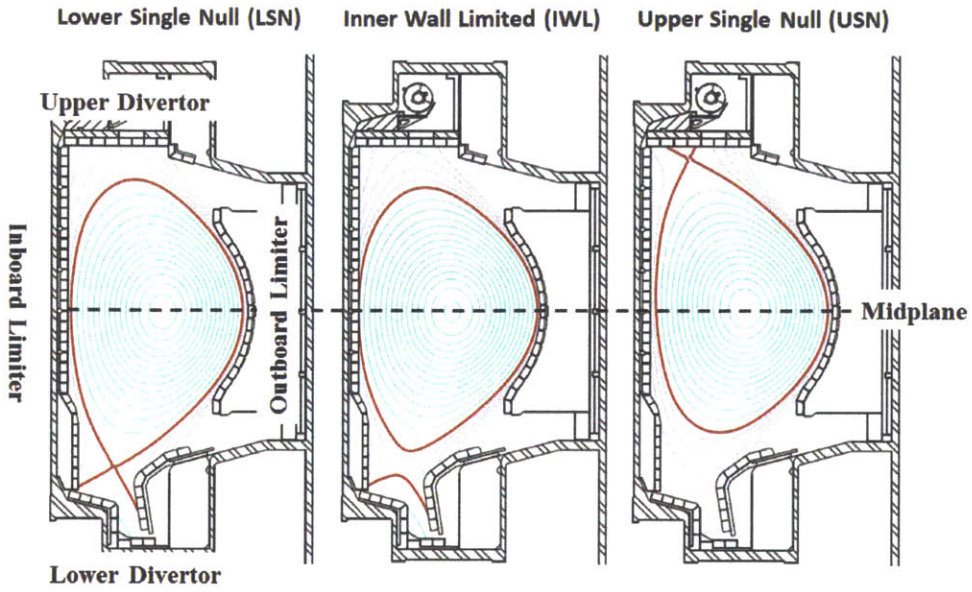

Figure 3-2: Poloidal cross sections of typical plasma configurations on Alcator C-Mod. Key in-vessel plasma facing structures are also labeled.

antenna at the J port, see Figure 3-3. The D, E, and J antennas operate at 80.5 MHz, 80.0 MHz, and 78.0 MHz, respectively, with the J antenna also capable of operating at 50 MHz. The dominant heating scheme is the hydrogen or helium-3 minority heating in deuterium main ion plasma species. The three antennas are capable of coupling up to 6 MW of ICRF power. The D- and E-antennas are capable of operating only in dipole antenna strap phasing (0, π). The J-port antenna is capable of operating in dipole (0, π, 0, π) and monopole (0, 0, 0, 0) antenna strap phasing. Up to 2011 the J antenna was in the form of a toroidally aligned (TA) antenna and in 2011 the J antenna was reconfigured to the field-aligned (FA) configuration [65].

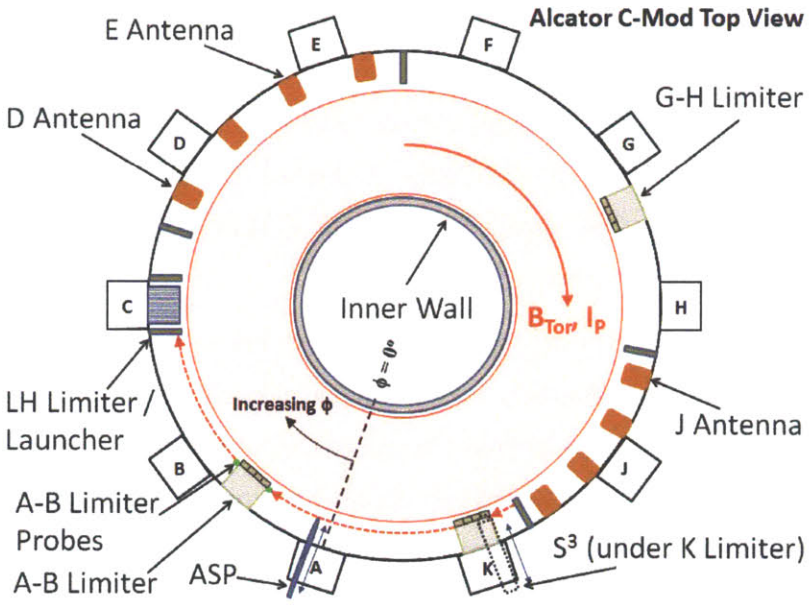

Figure 3-3: A diagram showing the top view of Alcator C-Mod. Key tokamak components and diagnostics are shown.

3.2 Emissive probes on Alcator C-Mod

As it was stated in Section 2.2 the emissive filament temperature is controlled by the electric current (either DC or rms) that passes through the filament. In tokamaks it is generally preferred to use an AC-heated emissive probe in order to minimize $J \times B$ forces on the filament during disruptions. The time scale for a typical disruption on Alcator C-Mod is $\sim$1 ms [66], which places the lower operating frequency bound on the AC circuit drive at $\gg$1 kHz. The operating frequency that is greater than 100 kHz introduces large inductive losses in the circuit elements. As a result, a desirable operating frequency range for the AC-driven emissive probe power supply is 10-100 kHz. The operating frequency for the Alcator C-Mod emissive probe power supplies was chosen to be 1 MHz/16 = 62.5 kHz. A detailed diagram of the circuit board used to drive emissive probes installed on Alcator C-Mod is provided in the Appendix section of the thesis, Figure A-2.

Figure 3-4 shows the temperature of the emissive filament wire as a function of the RMS current. We used a 2.5 cm long piece of the thoriated tungsten wire ($d_{wire} = 125\ \mu m$), which is a typical length of the filament used in our study. The filament temperature was measured with an optical pyrometer from Leeds and Northrup Company, Serial No: 1877250, Cat. No: 863 6-C [67]. Figures 2-6 and 3-4 show that it is sufficient to use the RMS current values of 2-2.5 A to make the emissive probe function as a plasma potential diagnostic in the SOL plasmas near ICRF antenna structures where $n_e \leq 1 \times 10^{18}\ m^{-3}$.

The steady-state operating temperature distribution along the filament of length L and diameter d is determined by balancing the Ohmic input power (P_Ω) with the power losses through radiation (P_γ) and conduction (P_κ) across the two ends of the filament, see Figure 3-5. Our goal is to determine the length of the hot region L_{hot} where the electron emission current density is equal to or higher than the electron current density incident on the filament from the plasma. L_{hot} is then used to constrain the size of the aperture ($L_{aperture} \leq L_{hot}$) that limits the part of the filament that is exposed to the plasma. The total length of the filament (L) is taken as 2.54

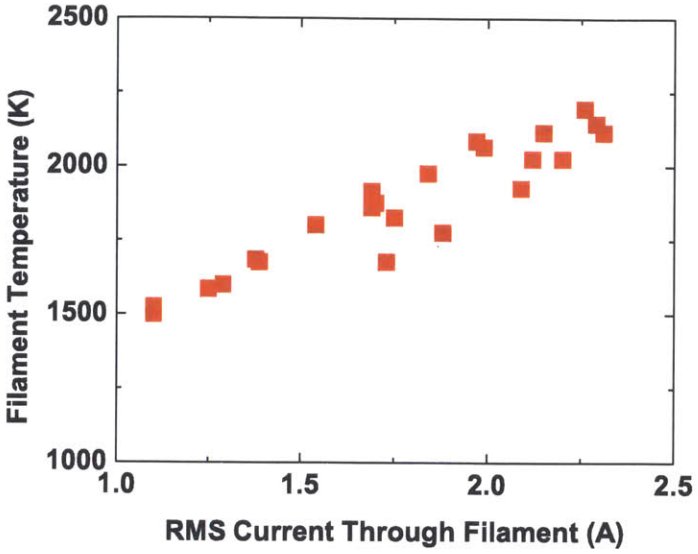

Figure 3-4: The measured emissive filament temperature as a function of the RMS current through the filament.

cm and is constrained by the space limitation for in-vessel components on Alcator C-Mod. For the case of the emissive probe the space limitation is characterized by the linear dimension of a single in-vessel tile, which is typically 2.5 cm.

The Ohmic input power is determined by Equation 3.1:

$$P_\Omega = \frac{I^2 L \eta}{\pi (d/2)^2}, \tag{3.1}$$

where I is either the DC or rms current through the filament, in units of [A], and η is the resistivity of the filament, in units of $[\Omega m]$. The resistivity is a strong function of the filament temperature $T_{filament}$ and for the particular case of tungsten it is given by Equation 3.2:

$$\eta_W = 4.8 \times 10^{-8}[1 + (T - 273)4.8297 \times 10^{-3} + (T - 273)^2 1.1663 \times 10^{-6}]\ [\Omega m], \tag{3.2}$$

where T is in degrees K [68]. η ranges from $2.5 \times 10^{-7}\ \Omega m$ to $1.1 \times 10^{-6}\ \Omega m$ for the filament temperature range from 1000 to 3000 K for tungsten, see Figure 3-6 [68].

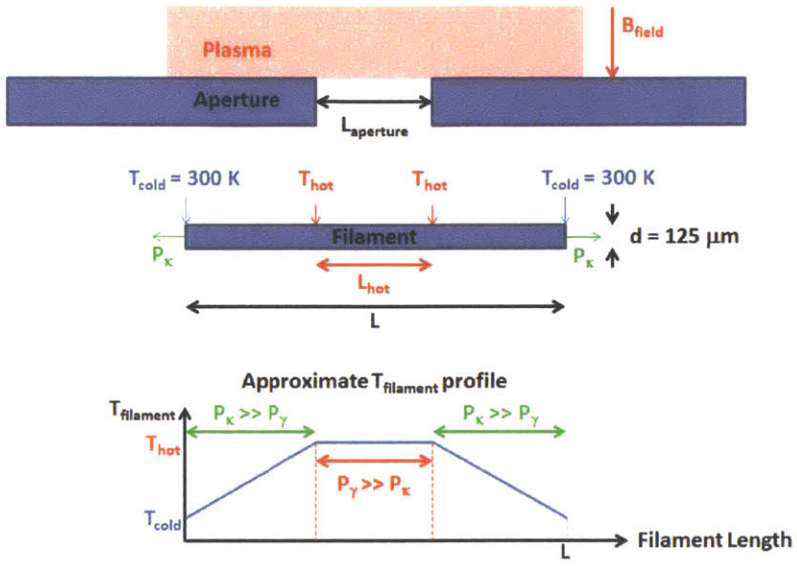

Figure 3-5: A diagram that shows the simplified arrangement used to estimate the temperature profile along the emissive filament.

The radiation power loss is given by Equation 3.3:

$$P_\gamma = L\pi d\epsilon\sigma T_{filament}^4, \tag{3.3}$$

where ϵ is the temperature-dependent filament emissivity ($\epsilon = 0.3$ for tungsten at 2000-3000 K [15]) and $\sigma = 5.67 \times 10^{-8}\ \frac{W}{m^2K^4}$ is the Stefan-Boltzmann constant. Note that the emissivity of a tungsten filament changes with age/use but it is generally in the range of $\epsilon = 0.3 - 0.4$ [69]. The conduction power losses are given by Equation 3.4:

$$P_\kappa = \kappa\nabla T_{filament}\pi(d/2)^2, \tag{3.4}$$

where κ is the thermal conductivity ($\kappa_W \sim 100\ \frac{W}{mK}$ at 2000 K, [15]) and $\nabla T_{filament} \approx \frac{\Delta T}{\Delta L}$, $\Delta T = T_{hot} - T_{cold}$, $\Delta L = \frac{L - L_{hot}}{2}$.

The strong temperature dependence of the radiated power ($P_\gamma \propto T^4$) allows us to make simplifying assumptions about the temperature profile along the filament: the hot region of the filament is dominated by radiative losses while conduction power losses dominate along the cold parts of the filament, see Figure 3-5. Using this

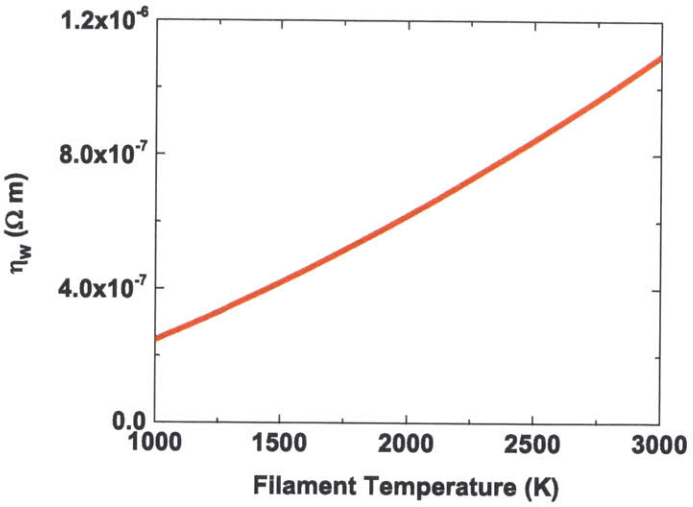

Figure 3-6: The resistivity of tungsten as a function of temperature [68].

assumption we obtain the length of the hot region from Equation 3.5:

$$L_{hot} = L - 2\Delta L = L - 2\sqrt{\frac{\kappa \Delta T \pi (d/2)^2}{I^2 \eta}}. \tag{3.5}$$

For the case of our tungsten wire ($L = 0.025\ m$, $T_{hot} = 2000\ K$, $T_{cold} = 300\ K$, $I_{rms} = 2\ A$, $\eta = \frac{\eta(300\ K)+\eta(2000\ K)}{2} = 3.3 \times 10^{-7}\ \Omega m$) we obtain $L_{hot} = 0.017\ m$. To be conservative we used an aperture length of $L_{aperture} = 0.008\ m = 0.5 L_{hot}$.

3.3 $\dot{B}$ probes on Alcator C-Mod

A 34 AWG copper wire (diameter $\varnothing = 1.6 \times 10^{-4}\ m$) was used to construct $\dot{B}$ probes for Alcator C-Mod probe stations. The RF probe resistance of the wire can be estimated from: $R_{probe} = \frac{\eta l}{\pi \varnothing \delta}$, where η is the DC resistivity of the probe wire ($\eta_{Cu} = 2 \times 10^{-8}\ \Omega\ m$ at room temperature) and δ is the skin depth of the probe material at frequency ω ($\omega = 2\pi \times 80\ MHz = 5.0 \times 10^{8}\ rad/s$). The skin depth at 80 MHz can be estimated as: $\delta = \sqrt{\frac{2\eta}{\omega\mu}}$, where μ is the magnetic permeability of the probe wire. For a good conductor, such as copper, the magnetic permeability is that of vacuum: $\mu = \mu_o = 4\pi \times 10^{-7}\ H/m$. Therefore, the skin depth of copper at 80 MHz is: $\delta = 8 \times 10^{-6}\ m$. A typical length of wire (l) used to construct a single $\dot{B}$ probe is ~0.1 m. Therefore, the RF resistance of a single $\dot{B}$ probe for our case is: $R_{probe} = 0.5\ \Omega$. Since our cable resistance is $R_{cable} = 50\ \Omega$, the condition $R_{probe} \ll R_{cable}$ is satisfied. The probe capacitance was measured directly and was typically 1 nF satisfying the assumption $C_{probe} \ll \frac{1}{2\pi \times 80 \times 10^6\ [rad/s] \times 0.5\ [\Omega]} = 4\ nF$.

Equation 2.9 allows us to optimize the signal-to-noise ratio ($S/N \equiv \left|\frac{V_{out}}{\dot{B}}\right|$) of a $\dot{B}$ coil with a fixed probe area (of loop diameter D) at a fixed ICRF operating frequency: S/N is maximized when the $\dot{B}$ coil uses an optimal number of turns N_{max}. The N_{max} is obtained by differentiating S/N with respect to the number of turns N and setting the value of the derivative to zero. The inductance of the probe L_{probe} with N loops is taken as: $L_{probe} \approx N^2 L_o$ [70], where L_o is the inductance of a single loop:

$$L_o = \frac{D\mu}{2}[\ln(\frac{8D}{\varnothing}) - 2]. \tag{3.6}$$

$$S/N = \frac{N A_{probe}}{[1 + (\frac{\omega N^2 L_o}{R_{cable}})^2]^{1/2}} \tag{3.7}$$

and

$$\frac{d(S/N)}{dN} = \frac{1 - (\frac{\omega N^2 L_o}{R_{cable}})^2}{[1 + (\frac{\omega N^2 L_o}{R_{cable}})^2]^{3/2}} = 0. \tag{3.8}$$

The final result is:

$$N_{max} = \sqrt{\frac{R_{cable}}{\omega L_o}}. \tag{3.9}$$

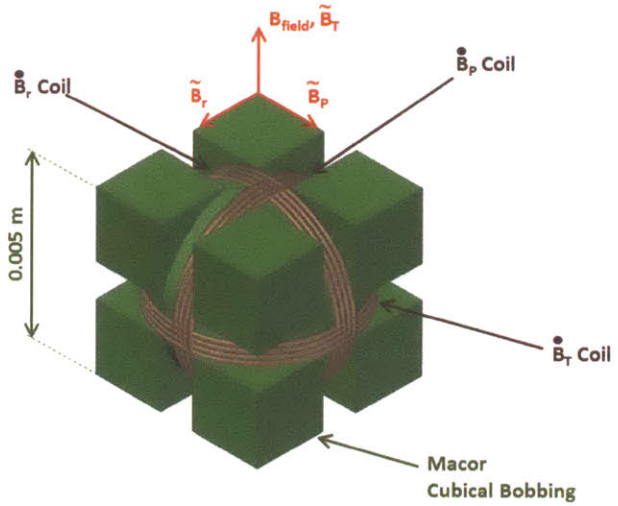

Figure 3-7: Details of the three-directional $\dot{B}$ probe used on Alcator C-Mod. The orientation of the three coils with respect to the local direction of the magnetic field is also shown. "T" refers to the direction along the magnetic field. "r" refers to the radial direction. "P" refers to the poloidal direction. $\widetilde{B}$ refers to the oscillating magnetic field amplitude of the RF wave.

For our specific case, the diameter of the $\dot{B}$ loop and, hence, the probe's area is constrained by the size of the aperture (7.5 mm) and we used $D = 5.1\ mm < 7.5\ mm$. This gives us $L_o = 10\ nH$ and, for $\omega = 2\pi \times 80 \times 10^6\ rad/s$, $N_{max} = 3.2$. The final design used four-turn $\dot{B}$ coils to account for a possible operation of the J antenna at 50 MHz, which increases N_{max}. Figure 3-7 shows the geometry of the three-dimensional $\dot{B}$ probe used in our studies and the directional definitions of the three coils with respect to the orientation of the local magnetic field. "T" refers to the direction along the magnetic field, "r" refers to the radial direction, and "P" refers to the poloidal direction. The $\dot{B}_T$ coil is used to quantify local fast ICRF wave fields ($\tilde{B}_T$) and the $\dot{B}_P$ coil is used to quantify local slow ICRF wave fields ($\tilde{B}_P$). Refer to Section 3.6, Figure 3-18 for a detailed description of the $\dot{B}$ probe position inside Alcator C-Mod.

The oscillating voltage signal, which is proportional to the local RF wave fields, is rectified to a DC voltage and then digitized. Two different circuit elements were used to achieve AC-to-DC conversion of the $\dot{B}$ signal. Prior to the Summer 2012

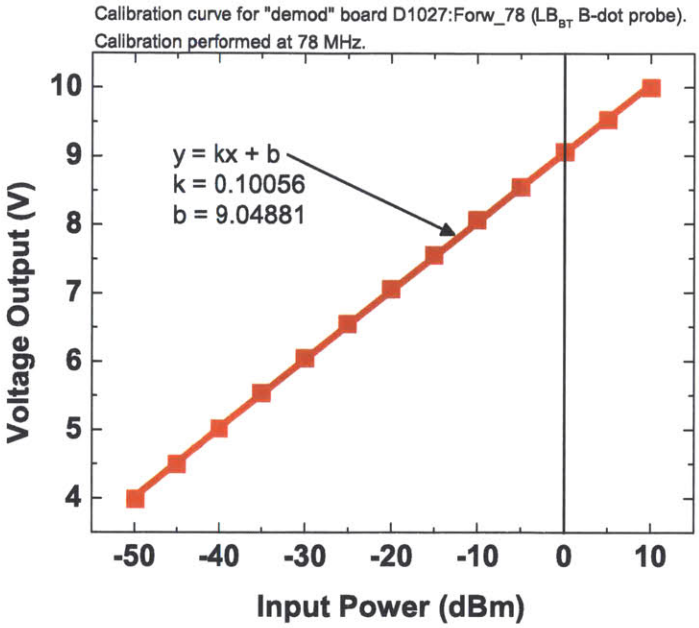

Figure 3-8: A calibration curve for a "demod" board used to convert an oscillating $\dot{B}$ signal into a DC voltage signal.

experimental campaign we used amplitude/phase detectors (or "demod" boards). These were extensively used on Alcator C-Mod for $\dot{B}$ signal rectification [31]. A typical calibration curve for these "demod" boards is shown in Figure 3-8: the DC voltage response is linear as a function of the input RF power. The calibration shown in Figure 3-8 was performed at 78 MHz, which corresponds to the operating frequency of the J antenna, and shows little variation between 78.0 and 80.5 MHz. A detailed diagram of the circuit board used to operate $\dot{B}$ probes installed on Alcator C-Mod is provided in the Appendix section of the thesis, Figure A-3.

During the Summer 2012 experimental campaign the rectification of the $\dot{B}$ signals was accomplished using zero-bias Schottky diode detectors, model number DZM020AA, from Herotek, Inc. The DC voltage response of the detector is an exponential curve with an offset as a function of the input RF power, see Figure 3-9. The calibration was performed at 80 MHz and the response of the detectors shows little variation between 78.0 and 80.5 MHz. Both the "demod" board and the Schottky crystal output voltages were digitized at 50 kHz.

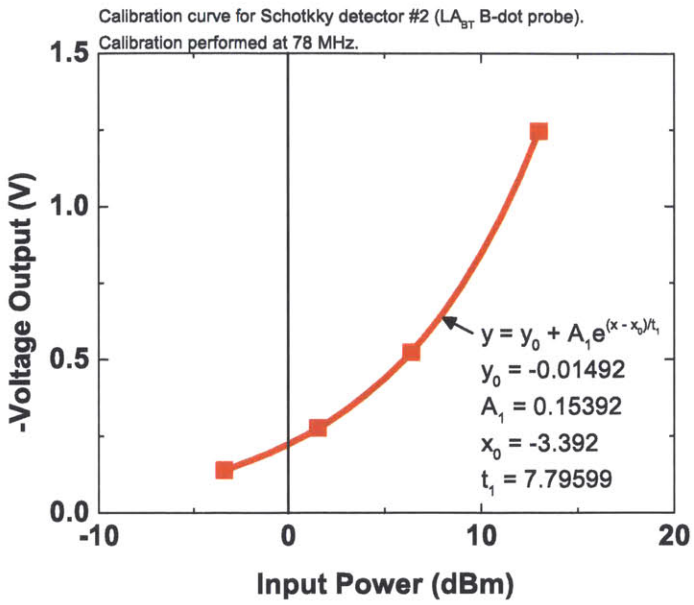

Figure 3-9: A calibration curve for a Schottky diode used to convert an oscillating $\dot{B}$ signal into a DC voltage signal.

Once we know the absolute power density of the RF signal collected by the $\dot{B}$ probes ($P_{\dot{B}}$), the magnetic ($\widetilde{B}$) and electric ($\widetilde{E}$) RF field amplitude can be estimated from the magnitude of the Poynting vector $\langle S \rangle$:

$$\langle S \rangle = \frac{P_{\dot{B}}}{N A_{probe}}, \tag{3.10}$$

$$\widetilde{E} = \sqrt{\frac{2\langle S \rangle}{c\epsilon_o}}, \tag{3.11}$$

and

$$\widetilde{B} = \sqrt{\frac{2\mu_o \langle S \rangle}{c}}. \tag{3.12}$$

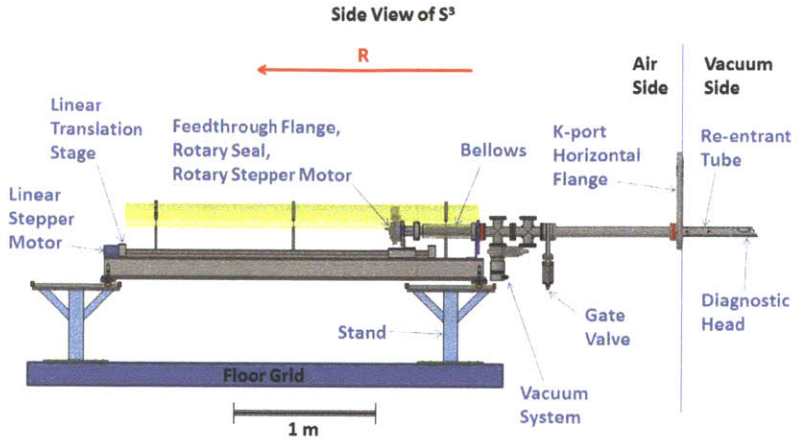

Figure 3-10: A side view of S^3 and its main components. The diagram shows fully inserted S^3 positioned at $R = 0.75\ m$ local radial position.

3.4 Surface Science Station (S^3)

A novel versatile diagnostic, the Surface Science Station or S^3, was developed and installed on Alcator C-Mod to study PMIs [64]. The key components of the S^3 diagnostic are a re-entrant tube, a removable diagnostic head, a vacuum rotary seal, a stainless steel bellows, a linear translation stage, two stepper motors (for linear and rotary motion), and a vacuum flange with multiple electrical feedthroughs, see Figure 3-10. The diagnostic is equipped with a dedicated vacuum system isolated by a gate valve from the Alcator C-Mod vacuum vessel. The vacuum system is capable of reaching the pressure of $1 \times 10^{-9}\ Torr$, well below the operating vacuum pressure of Alcator C-Mod ($\sim 1 \times 10^{-8}\ Torr$).

The S^3 is installed at the horizontal K port, with the center of the re-entrant tube located below the midplane at $Z = -0.220\ m$, see Figure 3-11. The re-entrant tube is aligned along the major radius direction. The outer diameter of the re-entrant tube is 57.15 mm (2.25") and is constrained by the diameter of the flange opening through the horizontal K-port flange, see Figure 3-11. The toroidal angular position of the S^3 is $\phi = 321.7^o$ where the angle is referenced with respect to the middle of the A-port, with the angle increasing in the clockwise direction as viewed from the top of the vacuum vessel. The linear translation speed of the diagnostic is typically

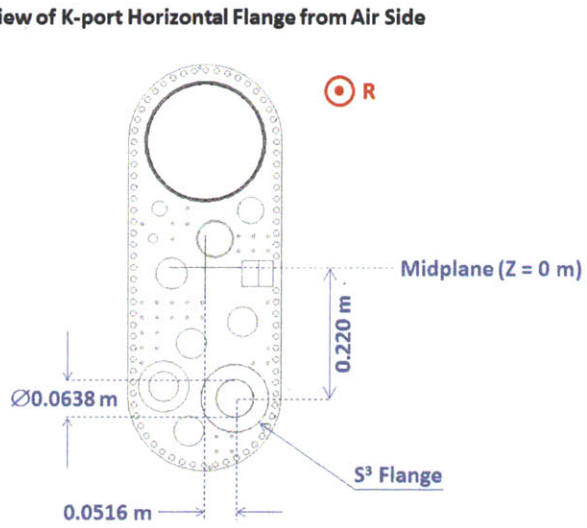

Figure 3-11: A view of the K-port horizontal flange from the air side. The location of the S^3 flange opening is shown.

~1 mm/s, which allows to change the radial probe position only between plasma discharges while keeping the radial position of the probe fixed for the duration of plasma discharges. The major radius position of the S^3 is known to within +/-0.5 mm and the uncertainty is limited by the resolution of the linear position voltage encoder.

In order to study plasma potential enhancement, the diagnostic head was equipped with an emissive, an ion sensitive and a Langmuir probe, see Figures 3-12 and 3-13. The plasma facing side of the diagnostic head is armored with a Mo cap the shape of which is aligned to the local poloidal magnetic field of a standard C-Mod plasma discharge ($I_P = 1\ MA$, $B_T = 5.4\ T$, lower single null (LSN) shape). Two apertures are used to define the area of the probes that is exposed to the plasma. The apertures allow plasma entrance only from the electron diamagnetic direction, which, for the toroidal magnetic field in the clockwise direction (as viewed from the top of the vessel), is vertically up at the midplane. The radial and vertical position of the Mo cap radially nearest to the tokamak central axis ($R = 0\ m$) is referred to as the "origin" point, see Figures 3-12 and 3-13. The positions of the three S^3 probes refer to the midpoints of the probe areas exposed to plasma and are referenced with respect

Point	R [m]	Z [m]	ϕ [degree]
Origin	Varies	-0.245	321.7
Emissive Probe	R_{Origin} + 0.031	Z_{Origin} + 0.033	ϕ_{Origin}
Langmuir Probe	R_{Origin} + 0.033	Z_{Origin} + 0.033	ϕ_{Origin}
ISP	R_{Origin} + 0.013	Z_{Origin} + 0.010	$R_{Origin}\phi_{Origin}$ - 0.006 [m]

Table 3.1: In-vessel positions (R, Z, and ϕ) of the S^3 origin, Langmuir, ISP, and emissive probes.

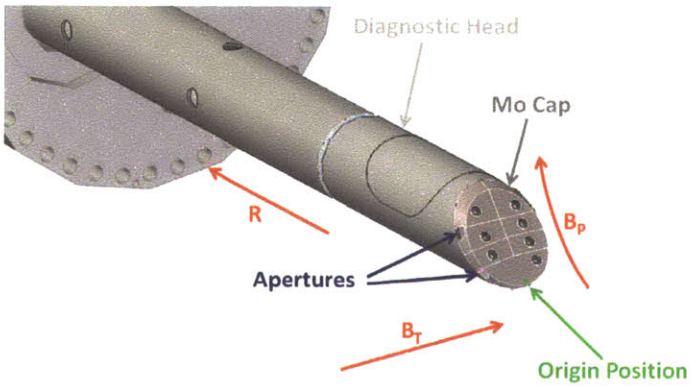

Figure 3-12: A close-up view of the S^3 diagnostic head with a protective Mo cap.

to the origin. Table 3.1 lists the positions of the origin and the three probes. The length of the emissive filament is constrained by the diameter of the re-entrant tube and the shape of the local poloidal magnetic field and is 2.5 cm. The length of the hot part of the filament and the size of the aperture opening is 7.6 mm. The Langmuir probe is located radially 2 mm behind the emissive probe to avoid direct magnetic field connection between the two probes ($R_{Langmuir\ probe} = R_{emissive\ probe} + 2\ mm$), see Table 3.1. The projected area (along the magnetic field) of the Langmuir probe that is exposed to plasma is $A_{probe} = 7.6\ mm \times 1\ mm = 7.6 \times 10^{-6}\ m^2$, see Figure 3-14. The relevant dimensions of the ISP are also shown in Figure 3-14.

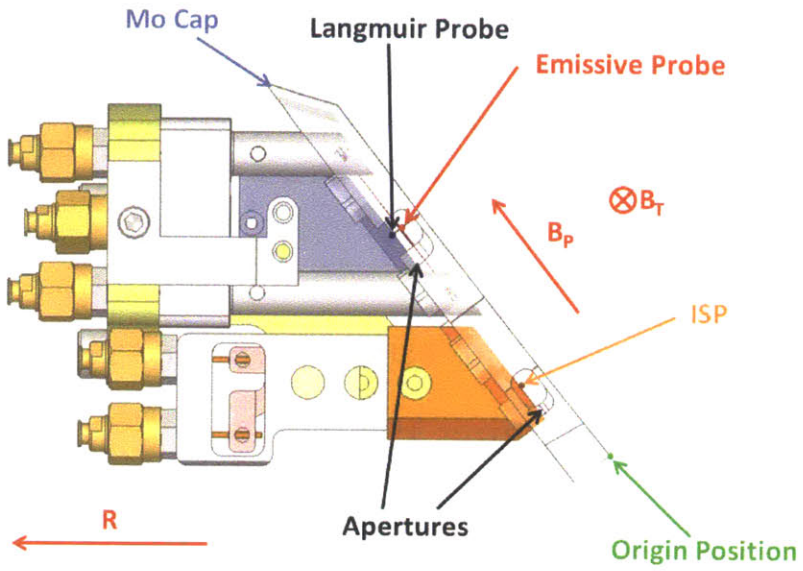

Figure 3-13: A detailed view of the Langmuir, ISP, and emissive probes on the S^3. The *Mo* cap is shown with a transparent outline.

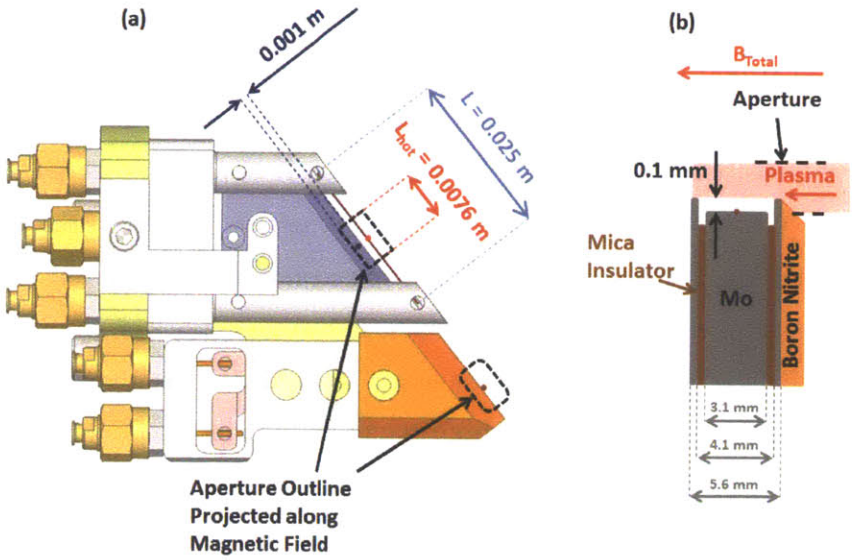

Figure 3-14: Relevant dimensions of the S^3 Langmuir, ISP, and emissive probes.

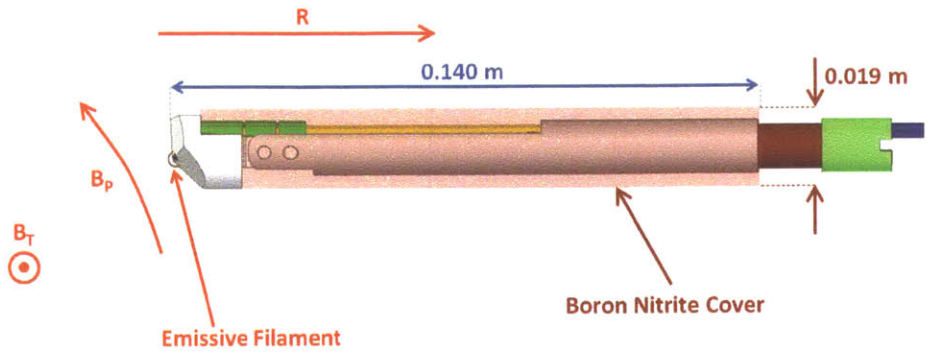

Figure 3-15: A diagram showing the ASP emissive probe head and its key dimensions.

3.5 A-port Scanning Probe

Another radially scanning diagnostic, the A-port Scanning Probe or ASP, was also used to study Φ_P enhancement on Alcator C-Mod [31]. Similarly to the S^3, the ASP contains a removable probe head. A new ASP probe head, armed with an emissive and two Langmuir probes, was designed and installed for the current study. Unlike the S^3 the ASP is much smaller in diameter (0.019 m in diameter, see Figure 3-15), contains four electrical feedthroughs, and is capable of up to three probe plunges within one flat-top period (~1 s) of a typical plasma discharge. The ASP is positioned at the horizontal A port, with the center of its re-entrant tube located 0.111 m above the midplane at the in-vessel toroidal angular position $\phi_{ASP} = 3.12^o$. Figure 3-16 shows the origin position of the ASP emissive probe head. Note from Figure 3-16 that only the hottest 1/3 of the total emissive filament length is exposed to the plasma, with the remaining length housed inside insulating ceramic tubes to prevent electrical and thermal contact with the Mo head tip. The in-vessel positions of the origin, emissive, and Langmuir probes are listed in Table 3.2. Note, that unlike the S^3 emissive probe, which is exposed to plasma only from the electron diamagnetic direction, the ASP emissive probe is exposed to plasma from both the electron and ion diamagnetic directions.

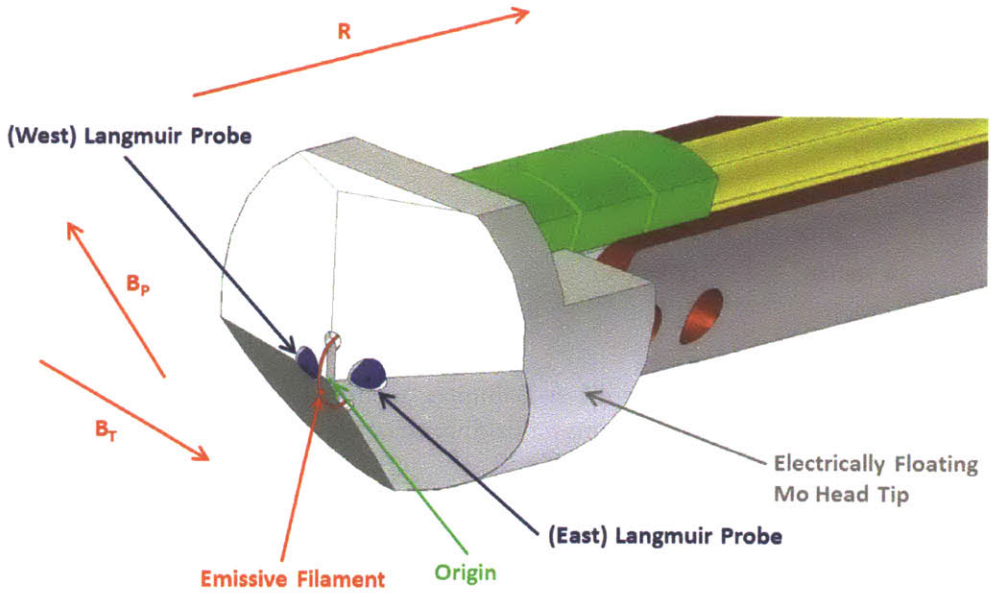

Figure 3-16: A close-up view of the *Mo* tip of the ASP emissive probe head. The tip is electrically floating and contains one emissive and two Langmuir probes.

Point	R [m]	Z [m]	ϕ [degree]
Origin	Varies	0.111	3.12
Emissive Probe	R_{Origin} - 0.001	Z_{Origin}	ϕ_{Origin}
West Langmuir Probe	R_{Origin}	Z_{Origin}	$R_{Origin}\phi_{Origin}$ - 0.002 [m]
East Langmuir Probe	R_{Origin}	Z_{Origin}	$R_{Origin}\phi_{Origin}$ + 0.002 [m]

Table 3.2: In-vessel positions (R, Z, and ϕ) of the ASP origin, Langmuir, and emissive probes.

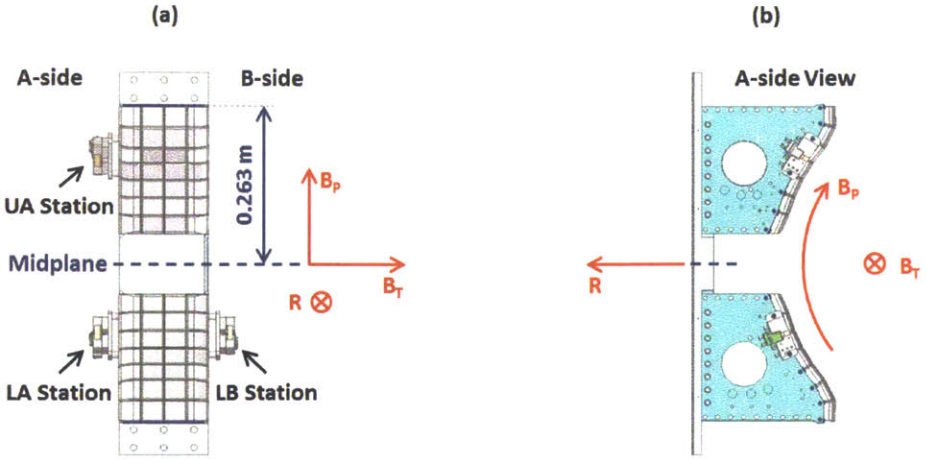

Figure 3-17: Views of the split A-B limiter mounted on the outer wall of Alcator C-Mod. (a) View along the major radius direction. (b) View along the toroidal magnetic field direction, A-port side.

3.6 Stationary A-B limiter probe stations

A combination of emissive, $\dot{B}$, and ISP probes were installed on probe stations mounted at fixed in-vessel locations on the sides of the split A-B limiter. Each probe station contained three (orthogonally aligned) $\dot{B}$ probes, one emissive, and one ISP probe. The probe station names are LB, LA, and UA and refer to the lower B, lower A, and upper A sides of the A-B limiter, see Figure 3-17. The midpoint of the emissive filaments is used as the "origin" position of the three stations. The in-vessel coordinates of the three origin points and the offset distances of the $\dot{B}$ and ISP probe centers along the R and Z coordinates are listed in Table 3.3. Note that only the LB station was used in the Summer/Fall 2009 experimental campaign and only the LA and UA stations were used in the Summer/Fall 2012 experimental campaign.

A detailed view of a single A-B limiter probe station (LA) is provided in Figure 3-18. The length of the emissive filament (0.025 m) is aligned to the direction of the local poloidal magnetic field of a standard Alcator C-Mod discharge ($I_P = 1\ MA$, $B_T = 5.4\ T$, LSN discharge shape). The length of the exposed part of the emissive filament (L_{hot}) is 7.6 mm. The three-directional $\dot{B}$ probe is housed inside a boron nitrite probe holder. The orientation of the $\dot{B}$ probes inside the holder is field-aligned

Point	R [m]	Z [m]	ϕ [degree]
LB Origin	0.911	-0.119	30.4
LB Emissive Probe	R_{Origin}	Z_{Origin}	ϕ_{Origin}
LB ISP	R_{Origin} + 0.003	Z_{Origin} - 0.001	ϕ_{Origin} + 0.3
LB $\dot{B}$ Probe	R_{Origin} - 0.006	Z_{Origin} + 0.003	ϕ_{Origin} + 0.1
LA Origin	0.911	-0.119	16.6
LA Emissive Probe	R_{Origin}	Z_{Origin}	ϕ_{Origin}
LA ISP	R_{Origin} + 0.003	Z_{Origin} - 0.001	ϕ_{Origin} - 0.3
LA $\dot{B}$ Probe	R_{Origin} - 0.006	Z_{Origin} + 0.003	ϕ_{Origin} - 0.1
UA Origin	0.879	0.179	16.6
UA Emissive Probe	R_{Origin}	Z_{Origin}	ϕ_{Origin}
UA ISP	R_{Origin} + 0.002	Z_{Origin} + 0.002	ϕ_{Origin} - 0.3
UA $\dot{B}$ Probe	R_{Origin} - 0.007	Z_{Origin} - 0.004	ϕ_{Origin} - 0.1

Table 3.3: In-vessel positions (R, Z, and ϕ) of the A-B limiter probe stations.

to a standard tokamak discharge configuration on Alcator C-Mod: $B_{T_o} = 5.4\ T$, $I_P = 1\ MA$ and the edge safety factor $q_{95} = 3.7$. The variation of the q_{95} values that were explored on Alcator C-Mod in the current study ($q_{95} = 3.3 - 5.1$) represents a deviation of the angle between the unit normal vector to the probe area and the magnetic field line of a few degrees. The corresponding error in the RF field amplitude measurement due to this misalignment is less than 20%. The outline of the $\dot{B}$ probe coil, as housed in the probe holder, is shown in Figure 3-18 (a). Note that the LA and UA probe stations are exposed to plasma incident from the electron diamagnetic direction (vertically up at the midplane) and the LB probe station is exposed to plasma incident from the ion diamagnetic direction only.

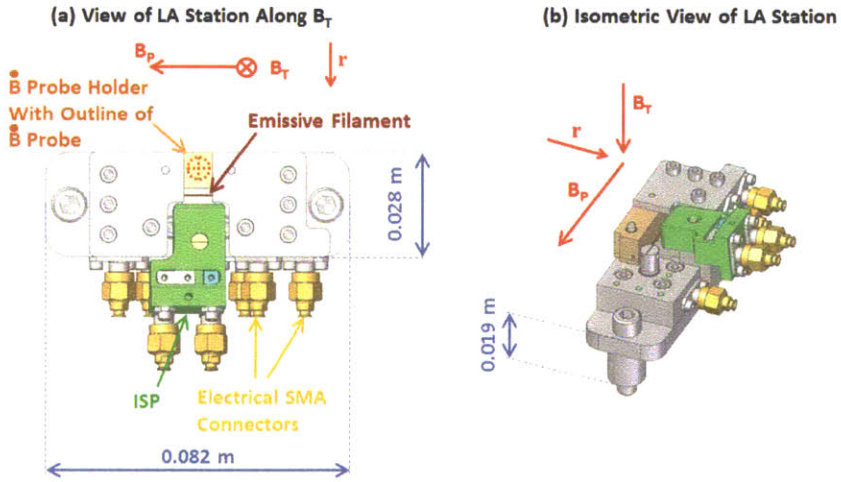

Figure 3-18: (a) A view of the LA probe station along the toroidal magnetic field direction. (b) An isometric view of the LA probe station with one half of the probe cover removed. "r" is the local minor radius direction.

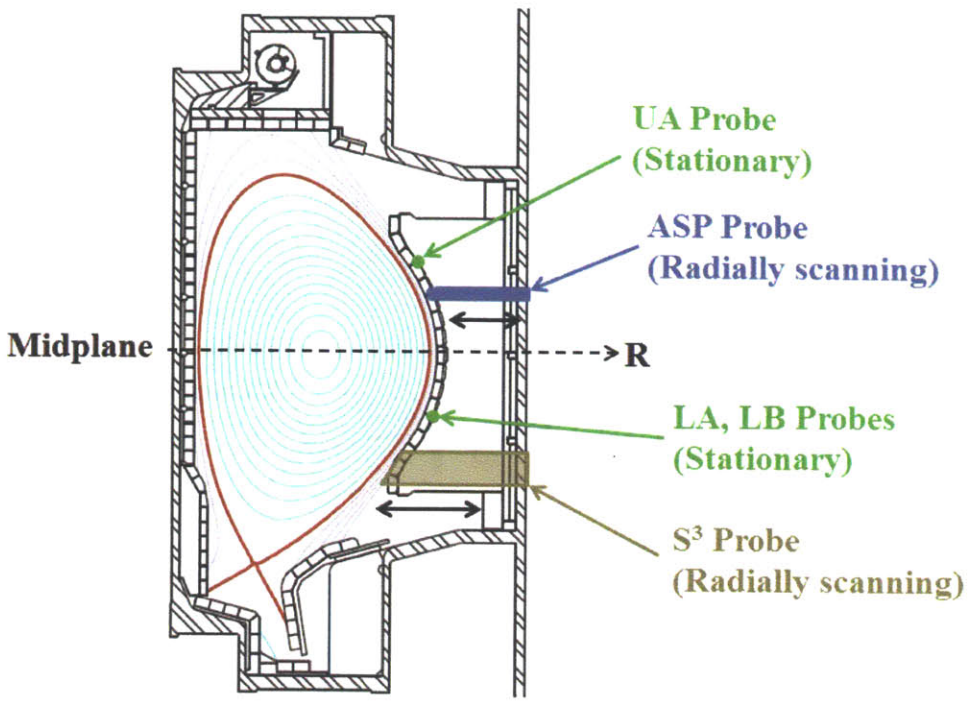

Figure 3-19: A poloidal cross sectional view of Alcator C-Mod. The poloidal locations of the primary diagnostics are shown.

3.7 Primary diagnostics

The poloidal cross sectional view of the Alcator C-Mod vessel and the poloidal positions of the primary diagnostics are shown in Figure 3-19. The top cross sectional view (at the midplane) of Alcator C-Mod with the primary in-vessel components and diagnostics is shown in Figure 3-20. A detailed top cross sectional view (projected to the midplane) of the A-B limiter and the primary diagnostic stations is shown in Figure 3-21, where d refers to the characteristic radius of the plasma facing limiter tip ($d \approx 1\ cm$). The fold-out views (along R) of the outer wall, together with the key in-vessel components and the primary diagnostics, are shown in Figures 3-22 and 3-23 for the cases of the toroidally and field-aligned J antennas, respectively. The red lines in Figures 3-22 and 3-23 are local magnetic field lines for $B_{To} = 5.5\ T$ and $I_P = 0.8\ MA$.

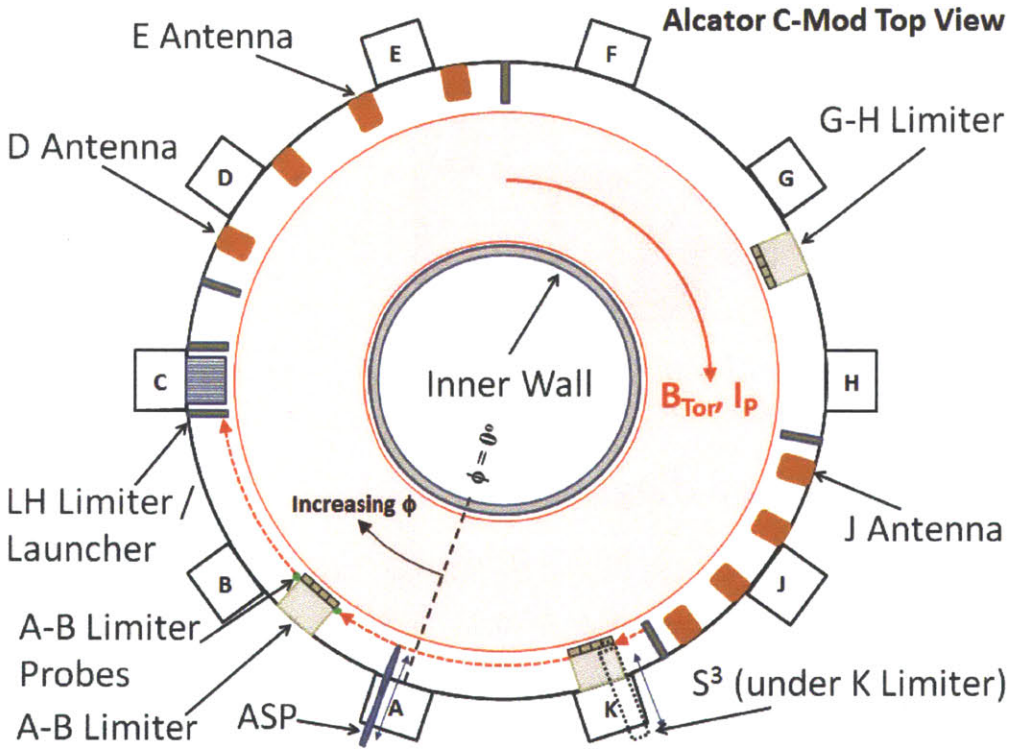

Figure 3-20: A diagram showing the top view of Alcator C-Mod. Key tokamak components and diagnostics are shown.

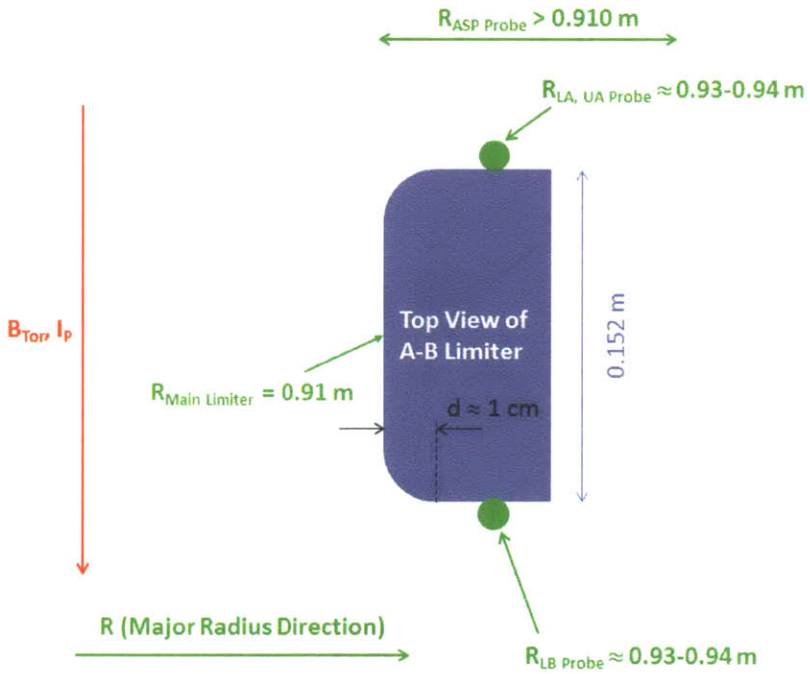

Figure 3-21: A detailed top cross sectional view (projected to the midplane) of the A-B limiter with the surrounding primary diagnostics. UA, LA, and LB probe stations are stationary. ASP probe station is radially scanning.

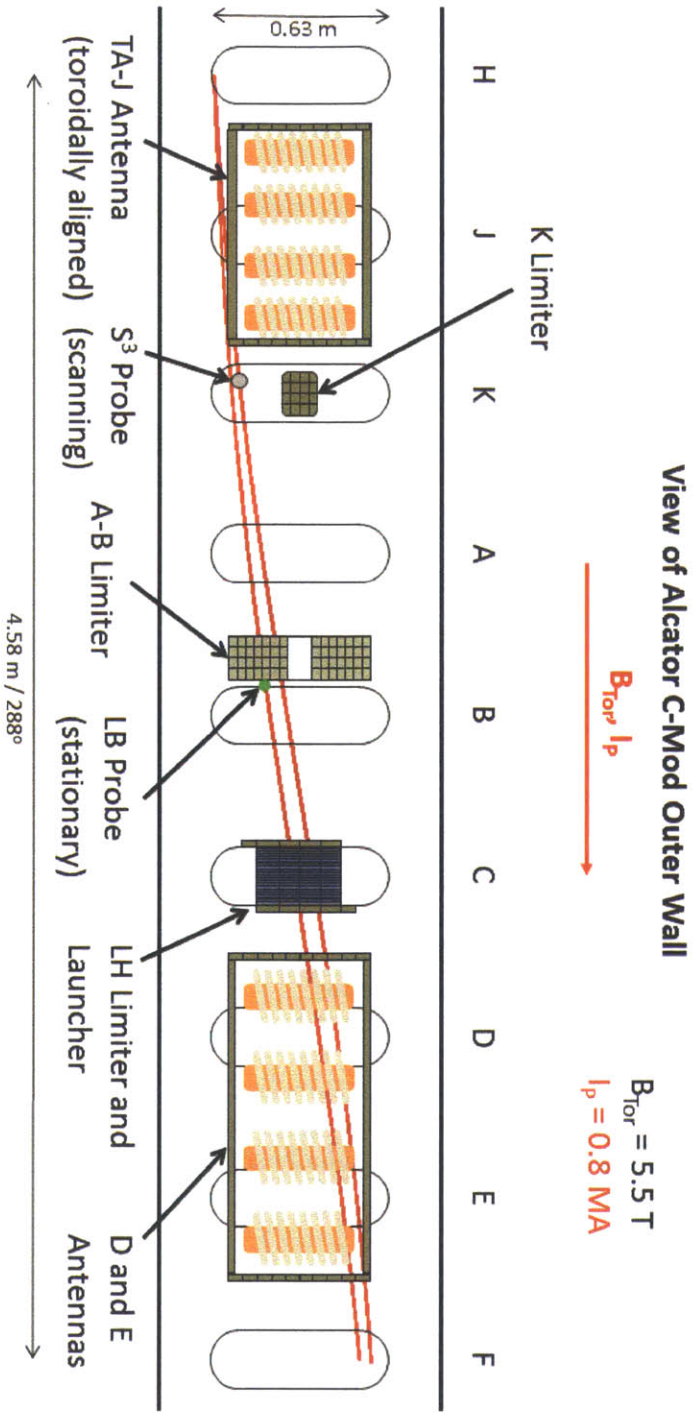

Figure 3-22: The probe arrangement used to characterize plasma potential enhancement with the J antenna in the toroidally-aligned (TA) configuration. Red lines show local magnetic field lines for the case of $B_{Tor} = 5.5\ T$ and $I_P = 0.8\ MA$.

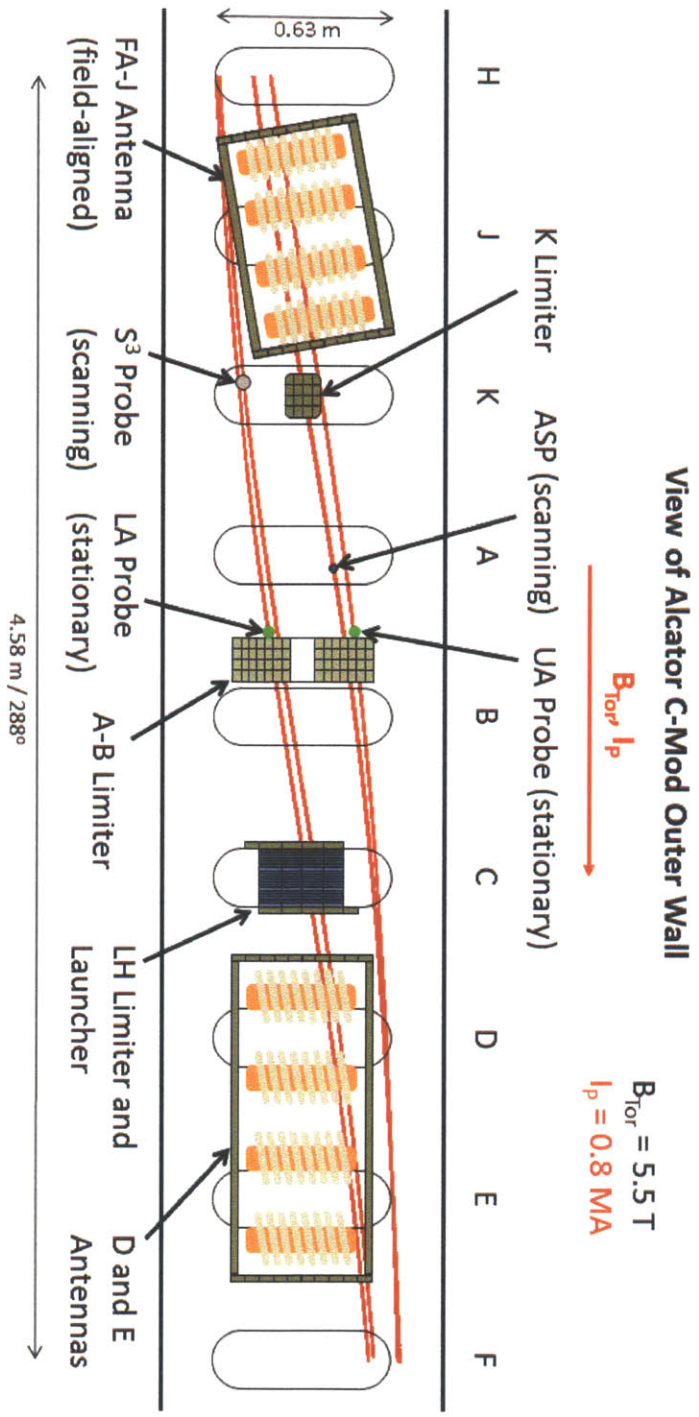

Figure 3-23: The probe arrangement used to characterize plasma potential enhancement with the J antenna in the field-aligned (FA) configuration. Red lines show local magnetic field lines for the case of $B_{Tor} = 5.5\ T$ and $I_P = 0.8\ MA$.

3.8 Secondary diagnostics

In addition to the primary diagnostics which were designed and installed specifically to study ICRF-induced plasma potential enhancement on Alcator C-Mod, we also used a number of secondary diagnostics. Some of the most commonly used of these include fixed Langmuir probes installed in the outer divertor regions [63], a gas puff imaging (GPI) system at the outboard midplane [71], a visible spectrometer (Chromex) with localized views of multiple limiter locations [20], and a multi-horn reflectometer at the outboard midplane [72]. EFIT was used to reconstruct equilibrium magnetic flux surfaces and to map magnetic field lines between probes and in-vessel surfaces [73].

Chapter 4

ICRF-enhanced plasma potentials: theoretical background

It has been long known that ICRF heating produces enhanced plasma potential and impurity production in the plasma boundary of tokamaks [23, 29]. In the simplest view, the fundamental mechanism for the enhanced sheaths potentials is the interaction of the electric field oscillations associated with the RF waves and the boundary/sheath region. The coupled response of the boundary must include a mechanism to "rectify" the AC E-field oscillations into a DC sheath potential [30]. The electron repelling DC sheath potential begins to accelerate positively charged ions toward the surface, which in turn are suspected to produce enhanced impurity sources through physical sputtering. Thus theoretical considerations must deal with the various permutations of RF-field polarization, RF power propagation and sheath response; which will be addressed in this chapter.

4.1 Waves in plasmas

Plasmas are a quasi-neutral collection of unbounded positively and negatively charged particles [21, 74]. As a results of the availability of free charges, plasmas are capable of supporting electromagnetic oscillations [21]. Although individual charges in a plasma are unbounded to each other, any significant separation of positive and negative

charges results in a generation of electric fields that begin to attract the separated charges. Accounting for the finite mass of the charged particles results in a collective oscillatory motion of all the charged particles: these are plasma waves [21]. Ignoring the electron thermal motion ($T_e = 0$) the electron plasma oscillations are given by Equation 4.1:

$$\omega_{pe} = \sqrt{\frac{n_e q_e^2}{m_e \epsilon_o}} \; [rad/s], \tag{4.1}$$

which reduces to $f_{pe} = 9.0\sqrt{n_e}$ $[Hz]$, where n_e is in units of [m^{-3}]. Similarly for the ion plasma wave oscillations:

$$\omega_{pi} = \sqrt{\frac{n_e q_i^2}{m_i \epsilon_o}} \; [rad/s], \tag{4.2}$$

which, for the case of deuterium ions, becomes $f_{pi} = 0.15\sqrt{n_e}$ $[Hz]$. The plasma ion density is assumed to be equal to the plasma electron density, i.e. the plasma is quasi-neutral.

When plasmas are placed in a static magnetic field, such as the case for tokamak plasmas, the mobility of the charged particles in the plasma remains unbounded only along the static magnetic field lines and becomes constrained by the Larmor motion across the field lines. The large difference between the parallel and perpendicular (to B field) charge mobilities is responsible for the large number of possible electromagnetic oscillations in magnetized plasmas [21]. The key quantities that determine the nature of electromagnetic oscillations in magnetized plasmas are the electron (Ω_e) and ion (Ω_i) gyro (also known as Larmor or cyclotron) frequencies:

$$\Omega_e = \frac{q_e B}{m_e} \; [rad/s], \tag{4.3}$$

$$\Omega_i = \frac{q_i B}{m_i} \; [rad/s], \tag{4.4}$$

For the case of electrons, Equation 4.3 becomes: $f_{\Omega_e} = 2.8 \times 10^{10}$ B $[Hz]$, where B is in [T] [34]. For the case of deuterium ions, Equation 4.4 is reduced to: $f_{\Omega_i} = 7.6 \times 10^6$ B $[Hz]$.

Accounting for the coupling between plasma and gyro frequencies introduces a number of so-called hybrid oscillations. The upper hybrid (UH) oscillations are given by Equation 4.5:

$$\omega_{UH}^2 = \Omega_e^2 + \omega_{pe}^2 \ [(rad/s)^2]. \tag{4.5}$$

The lower hybrid (LH) oscillations are given by Equation 4.6:

$$\frac{1}{\omega_{LH}^2} = \frac{1}{\Omega_i^2 + \omega_{pi}^2} + \frac{1}{|\Omega_i \Omega_e|} \ \left[\frac{1}{(rad/s)^2}\right]. \tag{4.6}$$

In order to determine how electromagnetic perturbations (or waves) propagate (or disperse) in plasmas, it is necessary to solve time-dependent Maxwell's equations:

$$\nabla \times \mathbf{E} = -\frac{\partial \mathbf{B}}{\partial t}, \tag{4.7}$$

$$\nabla \times \mathbf{B} = \mu_o \mathbf{J} + \frac{1}{c^2}\frac{\partial \mathbf{E}}{\partial t}, \tag{4.8}$$

where μ_o is the vacuum permeability, $\mathbf{J}$ is the plasma current density, and c is the speed of light in vacuum. Ohm's law is also needed to link $\mathbf{J}$ and $\mathbf{E}$:

$$\mathbf{J} = \bar{\bar{\sigma}} \cdot \mathbf{E}, \tag{4.9}$$

where $\bar{\bar{\sigma}}$ is the plasma conductivity tensor.

Several approximations are often applied to obtain an algebraic solution that preserves key physics of wave propagation in plasmas. 1) The thermal motion of the electrons and ion is ignored, i.e. the plasma is assumed to be "cold" with $T_e = 0$ and $T_i = 0$. 2) The charged particle motion is assumed to be collisionless and fluid-like. 3) The magnetic and electric wave field amplitudes are assumed to be small so as not to significantly perturb the background plasma properties that govern the wave propagation. The background plasma conditions are assumed to be static. 4) The wave oscillations are assumed to be periodic of the form $e^{[i(\mathbf{k}\cdot\mathbf{r}-\omega t)]}$, where $\mathbf{k}$ is the wave vector, $\mathbf{r}$ is the position vector, ω is the angular wave frequency, and t is time.

After performing Fourier analysis in space ($\nabla = i\mathbf{k}$) and time ($\frac{\partial}{\partial t} = -i\omega$) on the

two Maxwell's equations and Ohm's law and introducing the wave index of refraction ($\mathbf{n} = \frac{c\mathbf{k}}{\omega}$), we eventually obtain the wave dispersion relation:

$$\mathbf{n} \times \mathbf{n} \times \mathbf{E} + \bar{\bar{\epsilon}} \cdot \mathbf{E} = 0, \tag{4.10}$$

where we introduced the dielectric tensor $\bar{\bar{\epsilon}} \equiv \bar{\bar{I}} + \frac{ic^2\mu_o}{\omega}\bar{\bar{\sigma}}$. μ_o is the vacuum permeability.

We are interested to know how electromagnetic waves launched from the boundary plasma regions propagate across the magnetic field lines to the plasma core. Therefore, it is convenient to decompose the index of refraction vector into its parallel ($\mathbf{n}_{//}$) and perpendicular $\mathbf{n}_\perp$ components, all directions are with respect to the background magnetic field. The dispersion relation now takes the following form:

$$\begin{bmatrix} \epsilon_\perp - n_{//}^2 & -i\epsilon_x & n_\perp n_{//} \\ i\epsilon_x & \epsilon_\perp - n_{//}^2 - n_\perp^2 & 0 \\ n_\perp n_{//} & 0 & \epsilon_{//} - n_\perp^2 \end{bmatrix} \cdot \mathbf{E} = 0, \tag{4.11}$$

where $\epsilon_\perp$, $\epsilon_{//}$, and ϵ_x are the components of the dielectric tensor $\bar{\bar{\epsilon}}$:

$$\bar{\bar{\epsilon}} = \begin{bmatrix} \epsilon_\perp & -i\epsilon_x & 0 \\ i\epsilon_x & \epsilon_\perp & 0 \\ 0 & 0 & \epsilon_{//} \end{bmatrix}. \tag{4.12}$$

Equation 4.11 and following assumes a Cartesian coordinate system with $\mathbf{B}$ along the $\mathbf{z}$ direction and (without loss of generality, because of rotational symmetry about $\mathbf{B}$) $\mathbf{k}_\perp$ along the $\mathbf{x}$ direction.

The goal of the derivation is to solve for the quantity that governs the cross field wave propagation between the RF antenna and the plasma core, i.e. $n_\perp$. In order to obtain a non-trivial solution of Equation 4.11 the determinant of the 3 $\times$3 matrix must be zero. The final result is a quadratic equation for $n_\perp^2$ of the form:

$$A(n_\perp^2)^2 + Bn_\perp^2 + C = 0. \tag{4.13}$$

The coefficients of Equation 4.13 are:

$$A = \epsilon_{//}((n_{//}^2 - \epsilon_\perp)^2 - \epsilon_x^2), \tag{4.14}$$

$$B = (n_{//}^2 - \epsilon_\perp)(\epsilon_{//} + \epsilon_\perp) + \epsilon_x^2, \tag{4.15}$$

$$C = \epsilon_\perp. \tag{4.16}$$

The solution for $n_\perp^2$ has two roots, which correspond to two possible wave modes:

$$n_\perp^2 = \frac{-B \pm \sqrt{B^2 - 4AC}}{2A}, \tag{4.17}$$

where the "+" root corresponds to the so-called slow wave (SW) and the "-" root is the fast wave (FW). The terms "slow" and "fast" refer to the magnitude of the perpendicular wave phase velocity $v_{\phi\perp} = \frac{\omega}{k_\perp}$.

A detailed derivation of the dielectric tensor components can be found in [12] and the final results are provided below:

$$\epsilon_\perp = 1 - \sum_s \frac{\omega_{ps}^2}{\omega^2 - \Omega_s^2}, \tag{4.18}$$

$$\epsilon_{//} = 1 - \sum_s \frac{\omega_{ps}^2}{\omega^2}, \tag{4.19}$$

$$\epsilon_x = \sum_s \frac{\Omega_s \omega_{ps}^2}{\omega(\omega^2 - \Omega_s^2)}, \tag{4.20}$$

where the summation is carried over all charged species (electrons, main ions, and, if present, impurity ions).

One other important quantity that needs to be considered is the polarization of the ICRF wave in the plane of the ion Larmor orbit. For the case of a Cartesian coordinate system ($\mathbf{E} = (E_x, E_y, E_z)$), where the background magnetic field is along z and $\mathbf{E_x}$ points along $\mathbf{k}$, the ion Larmor orbit lies in the X-Y plane. Therefore, the polarization for the perpendicular electric field components is defined as $\frac{E_x}{E_y}$. Using the middle row from the matrix in Equation 4.11 the equation for the wave polarization

becomes:

$$\frac{E_x}{E_y} = i\frac{\epsilon_\perp - n_{//}^2 - n_\perp^2}{\epsilon_x}. \tag{4.21}$$

The polarization for the parallel electric field component can be obtained from the last row of the matrix in Equation 4.11:

$$\frac{E_x}{E_z} = -\frac{n_{//}n_\perp}{\epsilon_{//} - n_\perp^2}. \tag{4.22}$$

Now that we have defined all of the relevant quantities of an electromagnetic wave, we are going to examine the wave's interaction with the plasma sheath.

4.2 ICRF wave – plasma sheath interactions

The interaction of the ICRF waves with the plasma sheath has been extensively studied theoretically in both idealized one- and two-dimensional geometries [75, 76, 77, 78, 79, 80]. Two key conditions must be met in order for the ICRF waves to enhance the plasma potential on open magnetic field lines in tokamaks. First, a standard (electron repelling) plasma sheath has to form in the presence of a large static magnetic field. This implies that the grazing angle (θ) between the magnetic field lines and the surface tangent must be $\theta \gtrsim 1^o$ to avoid any ion gyroradii effects on the formation of the sheath [81]. And second, there must be a non-zero oscillating parallel electric field ($\tilde{E}_{//} \neq 0$) at the plasma-sheath boundary because in this case the RF E-field is parallel to the E-field produced by a standard thermal sheath and therefore can directly affect the potential structure. From a practical point of view we are also primarily interested in rectified DC E-fields perpendicular to surfaces since these control incident ion energy and therefore sputtering. Because of the large difference in the ion and electron mobility, the cycle-averaged current response to $\tilde{E}_{//}$ at the surface becomes dominated by the electron current and in order to preserve the cycle-averaged ambipolarity condition (*net* current into the surface is equal to zero) an additional RF-enhanced electron repelling DC potential develops across the plasma sheath [30].

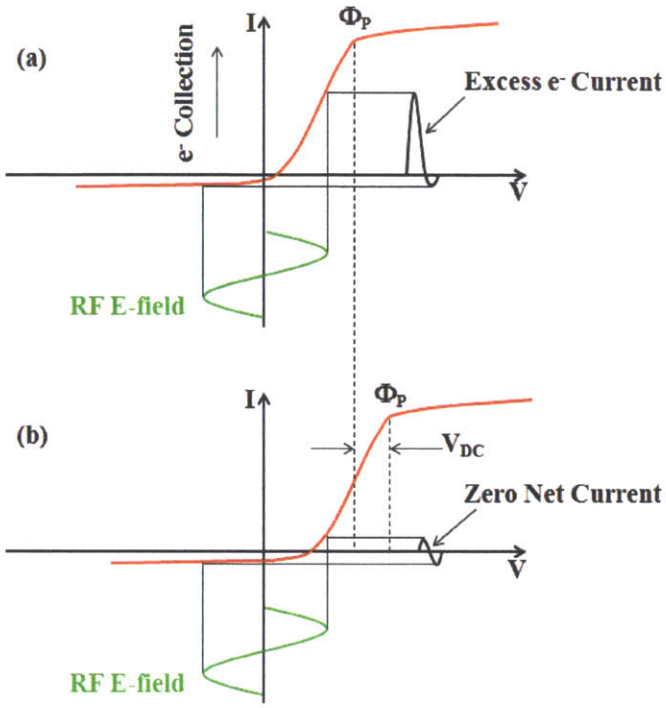

Figure 4-1: A diagram that demonstrates the generation of an ICRF-induced electron repelling DC potential (V_{DC}) across the plasma sheath in response to an oscillating electric field $\tilde{E}_{//}$. (a) before rectification and (b) after rectification. The reference voltage is the surface/wall potential.

A diagram that demonstrates the above-described mechanism is shown in Figure 4-1. The I-V curve refers to the current collection at a surface as a function of the voltage applied across the plasma sheath. Note that the reference potential in this diagram is the surface/wall potential, therefore, the RF-induced electron repelling DC potential (V_{DC}) across the plasma sheath is positive. While the first condition ($\theta \gtrsim 1^o$) is met by most plasma facing surfaces in contact with the SOL plasma in tokamaks, the fulfillment of the second condition depends on the details of the launched ICRF wave polarization.

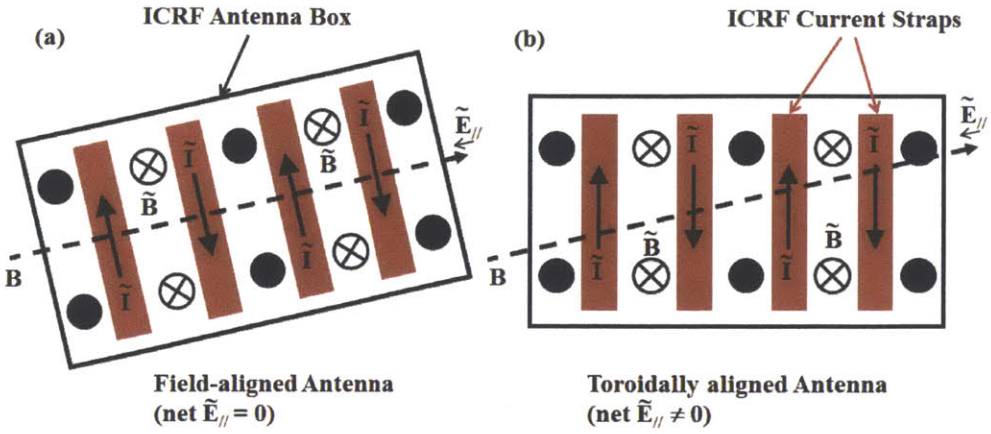

Figure 4-2: A diagram that shows a basic principle by which slow ICRF waves are launched by an ICRF antenna. $\tilde{I}$ refers to the RF current flowing along the antenna straps, B is the background static magnetic field, $\tilde{E}_{//}$ is the parallel component of the electric RF fields generated by $\tilde{I}$, and $\tilde{B}$ are the magnetic RF fields generated by $\tilde{I}$.

4.3 Slow wave-plasma sheath interaction

One way to meet the $\tilde{E}_{//} \neq 0$ condition is to directly launch a propagating ICRF wave with a non-zero $\tilde{E}_{//}$ component, which, in our case, is the slow wave. Even though a typical (toroidally aligned or TA) ICRF antenna is designed to launch fast ICRF waves, a mismatch between the antenna geometry and the background static magnetic field results in generation of slow ICRF waves, see Figure 4-2. For the misaligned case (Figure 4-2 (b)) the net $\tilde{E}_{//}$ across multiple antenna straps is not zero and results in the excitation of slow wave fields at the active antenna. Once launched, the propagation properties of the slow ICRF wave are determined by its dispersion relation [12]. In order to determine the dispersion relation of a launched slow wave, it is necessary to know the plasma density profile at the antenna.

The radial plasma density profile is shown for a typical (L-mode) discharge on Alcator C-Mod in Figure 4-3. Using the plasma density profile in Figure 4-3, it is now possible to determine the slow wave dispersion in the vicinity of the ICRF antenna, see Figure 4-4 for several typical values of launched $n_{//}$. The cross field propagation of the slow ICRF wave is limited to the low density region, the plasma

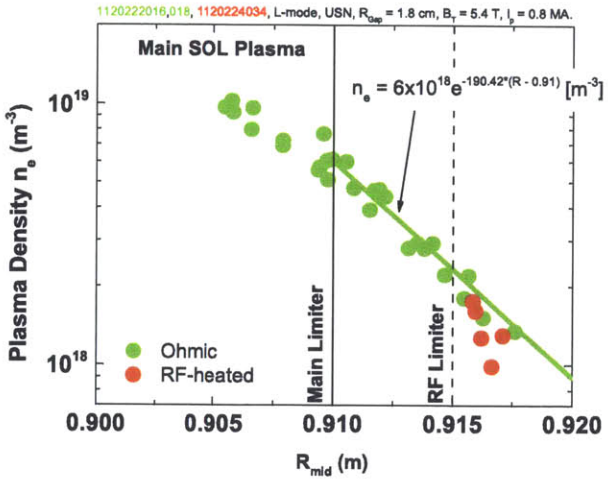

Figure 4-3: An experimentally determined radial plasma density profile in the vicinity of the main limiter on Alcator C-Mod. L-mode discharge. The separatrix is located at $R_{mid} = 0.892\ m$.

density that is below its value at the lower hybrid resonance ($n_{LH} \approx \frac{m_i \epsilon_o}{q_e^2}(\omega^2 - \Omega_i^2)$, $n_{LH} = 2.5 \times 10^{17}\ m^{-3}$ for $f = 80\ MHz$. As can be seen from Figure 4-4, the slow ICRF wave becomes deeply evanescent in the high density plasma regions ($n_e > n_{LH}$) with the characteristic e-fold decay length ($\frac{1}{|k_\perp|}$) less than 1 mm.

It is possible to obtain a simplified algebraic form of the slow wave dispersion relation by considering the launched wave frequency in the vicinity of the ion cyclotron frequency ($\omega \sim \Omega_i$). This condition leads to the following orderings: $n_\perp^2 \sim \epsilon_{//}$, $n_\perp^2 \gg \epsilon_\perp$, $n_\perp^2 \gg \epsilon_x$. The cold plasma dispersion relation for the slow *ICRF* wave is provided by Equation 4.23 [79]:

$$n_\perp^2 = (1 - \frac{n_{//}^2}{\epsilon_\perp})\epsilon_{//}. \tag{4.23}$$

Figure 4-5 shows the details of the slow ICRF wave dispersion in the propagating region. Note several key features of the dispersion curves. 1) The slow wave becomes evanescent in very low plasma density regions. The dispersion relation becomes that of an electromagnetic wave in vacuum: $n_\perp^2 + n_{//}^2 = 1$. The perpendicular wave vector

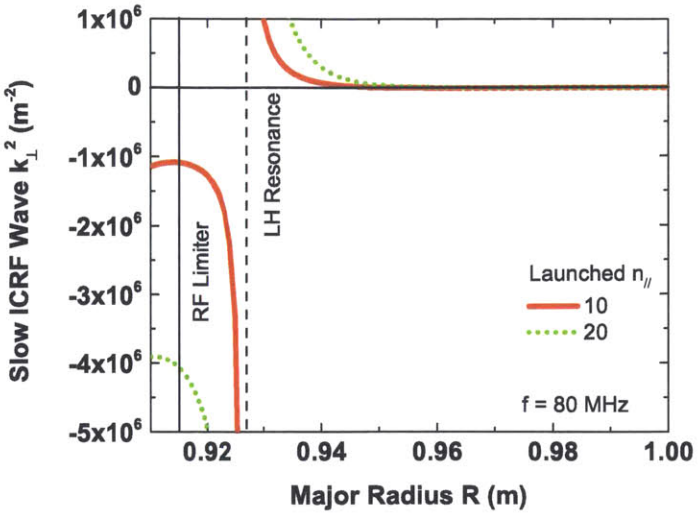

Figure 4-4: A typical cold wave dispersion relation for a slow ICRF wave launched at the low field side of a typical Alcator C-Mod discharge. $B_{To} = 5.4\ T$, $R_o = 0.67\ m$, launched $n_{//} = 10$ (solid curve) and 20 (dotted curve), launched $f = 80\ MHz$. The main limiter is located at $R = 0.910\ m$. Deuterium plasma. The plasma density profile is shown in Figure 4-3. LH Resonance refers to the lower hybrid resonance location.

shows an asymptotic behavior: $k_\perp^2 \rightarrow (1 - n_{//}^2)(\frac{\omega}{c})^2$. 2) The point at which the slow wave propagation transitions to that of a vacuum wave is given by the condition $n_\perp^2 = 0$ or $\epsilon_{//} = 0$. Using the expression $\epsilon_{//} = 1 - \frac{\omega_{pe}^2}{\omega^2}$ [79] it is possible to find the plasma density value at that cut-off. $f_{pe} = 9\sqrt{n_e} = 80 \times 10^6\ Hz$ or $n_e = 7.9 \times 10^{13}\ m^{-3}$. Note that this value is independent of $n_{//}$. 3) The slow wave dispersion relation in the propagating region ($7.9 \times 10^{13}\ m^{-3} < n_e < 2.5 \times 10^{17}\ m^{-3}$) may be approximated even further as: $n_\perp^2 \approx (1 - n_{//}^2)\epsilon_{//} \rightarrow (\frac{\omega_{pe}}{\omega} n_{//})^2$ for the case of $n_{//} \gg 1$. The approximate solutions are plotted in Figure 4-5. The asymptotic values given by Equation 4.24

$$n_\perp^2 = (\frac{\omega_{pe}}{\omega} n_{//})^2 \tag{4.24}$$

are a good representation of the slow ICRF wave dispersion relation over a wide section of the propagation region away from the lower hybrid resonance and the low density cut-off.

Plasma potential enhancement due to the slow ICRF wave in low density plasma

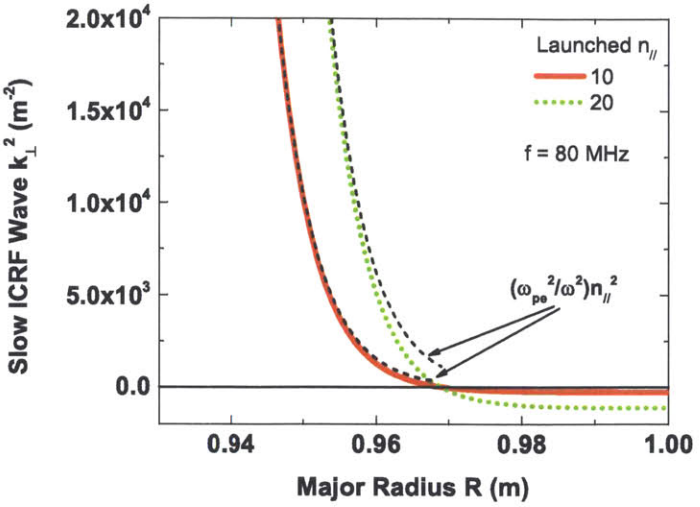

Figure 4-5: Slow ICRF wave dispersion relation in the region of propagation. $B_{To} = 5.4\ T$, $R_o = 0.67\ m$, launched $n_{//} = 10$ (solid curve) and 20 (dotted curve), launched $f = 80\ MHz$. The main limiter is located at $R = 0.910\ m$. Deuterium plasma. The plasma density profile is shown in Figure 4-3. Black dashed lines are asymptotic values.

regions (where the slow ICRF wave is allowed to propagate) has been extensively studied theoretically [75, 76, 77]. Once generated in a low plasma density region the slow waves propagate in the form of resonance cones or RC's [84]. The RC's travel nearly along the background magnetic field with a small, but finite, cross-field extent: $\frac{k_\perp}{k_{//}} \sim \frac{\omega}{\omega_{pe}} \ll 1$. When the RC's reach material surfaces, the parallel electric field component of the slow wave begins to interact with the plasma sheath. The plasma sheath is generally modeled as a thin vacuum-like region of thickness Δ with a normalized dielectric constant $\epsilon_{sh} \sim 1$. The RF-rectified voltage drop across the sheath (Φ_{RF}) can be estimated according to:

$$\Phi_{RF} = -\Delta \epsilon_{//} \tilde{E}_{//}, \tag{4.25}$$

where the relation between Φ_{RF} and Δ is constrained by the Child-Langmuir Law (Equation 2.11):

$$\Delta \sim \Phi_{RF}^{3/4}. \tag{4.26}$$

The final solution reveals that the slow wave rectification mechanism has a threshold appearance with the dimensionless rectification parameter Λ_o – when Λ_o is above unity strong Φ_P enhancement ($e\Phi_P \gg 3T_e$) is now allowed [76, 77]. Λ_o is expressed in terms of local plasma parameters according to Equation 4.27:

$$\Lambda_o = -\frac{\lambda_{de}\epsilon_{//}}{a}|\frac{\alpha e V_o}{T_e}|^{3/4}, \tag{4.27}$$

where λ_{de} is the electron Debye length, $\epsilon_{//} \equiv 1 - \frac{\omega_{pe}^2}{\omega^2}$, ω_{pe} is the electron plasma frequency, ω is the operating ICRF antenna frequency, a is the parallel (to static B field) scale length of the RC launching structure (the toroidal width of the current strap), α is a numerical factor of order unity, e is the elementary charge, V_o is the RF source voltage at the antenna, and T_e is the local electron temperature. Note that V_o is *not* the RF voltage that is directly driven on the current straps but is a result of a non-zero $\tilde{E}_{//}$: $V_o \equiv \int \frac{\tilde{\mathbf{E}}_{//}\cdot\mathbf{B}}{|B|}dl$, where the integral is taken along the magnetic field in front of the active antenna [76]. When the RF-sheath parameter satisfies $\Lambda_o \ll 1$ then the ICRF-induced voltage across the sheath (Φ_{RF}) is negligible and may be approximated as $|\Phi_{RF}| \sim |V_o|\Lambda_o^4$. In the opposite extreme ($\Lambda_o \gg 1$) the ICRF-induced voltage becomes comparable to the source voltage: $|\Phi_{RF}| \sim |V_o|$. Since $\lambda_{de} \sim n_e^{-1/2}$, $\omega_{pe} \sim n_e^{1/2}$, and $|V_o| \sim P_{RF}^{1/2}$, where n_e is the local electron density and P_{RF} is the launched ICRF power, we may recast Equation 4.27 as:

$$\Lambda_o \sim n_e^{1/2} P_{RF}^{3/8}, \tag{4.28}$$

which provides a convenient form to test Equation 4.27 experimentally. Note that the electron temperature dependence does not appear in Equation 4.28: it is experimentally found that the electron temperature in the vicinity of the ICRF antenna is typically 10-20 eV and shows little variation with ICRF power or core plasma paramaters.

To summarize, the key (and testable) findings of the slow wave theory are listed below. 1) Slow ICRF waves, that are directly launched by the active antennas,

propagate primarily along the background static magnetic field lines in the form of resonance cones or RC's. This condition localizes slow sheath rectification mechanism to magnetic field lines that directly intercept active ICRF antenna structures. 2) Slow waves only propagate in the low density region. For the case of Alcator C-Mod and its ICRF antennas ($f = 80\ MHz$), this region is bounded by $7.9 \times 10^{13}\ m^{-3} < n_e < 2.5 \times 10^{17}\ m^{-3}$. 3) The interaction between the RC's and the plasma sheath may be quantified by a dimensionless RF-sheath parameter Λ_o defined by Equation 4.27, which depends on both local plasma density and RF power such that a threshold is expected in order to obtain a strongly enhanced sheath for impurity generation.

4.4 Fast wave-plasma sheath interaction

The fast wave, which is used for ICRF core plasma heating, does not have an RF E-field parallel ($\tilde{E}_{//}$) to the static magnetic B-field; rather the RF E-field is in the plane perpendicular to the B-field. However, it is still capable of enhancing the plasma potential on open magnetic field lines in contact with conducting surfaces in the SOL region [78, 79, 80]. The mechanism involves reflection of fast waves incident on conducting material surfaces: as long as the surface plane is neither parallel ($\mathbf{s} \cdot \mathbf{b} \neq 0$, where $\mathbf{s}$ is the unit vector normal to the surface and $\mathbf{b}$ is the unit vector parallel to the total magnetic field), nor perpendicular ($\mathbf{s} \times \mathbf{b} \neq 0$) to the total magnetic field both an incident and a reflected RF E-field are necessary to satisfy the conducting boundary condition ($\sum \tilde{\mathbf{E}}_\mathbf{t} = 0$, where the sum includes the tangential components of the incident and reflected RF electric fields ($\tilde{\mathbf{E}}_\mathbf{t}$)). The conducting boundary condition can be recast as $\mathbf{s} \times \tilde{\mathbf{E}} = 0$. By the necessity of producing a component of the RF E-field parallel to B in reflection, a slow wave becomes excited at the surface. Stated another way, a FW incident on a conducting boundary will effectively convert some of the RF fast-wave power into a slow wave. Once a slow wave is excited by this process, the usual DC rectification of the slow wave (parallel) electric field takes place. A simple 2-D case that demonstrates the above-described fast-to-slow wave coupling mechanism is shown in Figure 4-6.

It was shown in the Introduction Section of the thesis that fast ICRF wave heating requires a non-zero concentration of minority ions in the core plasma to form a wave-plasma resonance that is necessary for wave absorption and heating (Figure 4-7). Note from Figure 4-7 that the two dispersion relations (with and without the minority ions in the plasma core) converge to each other away from the ICRF resonance.

Using the experimentally determined radial plasma density profile in the shadow of the main limiter (Figure 4-3) it is possible to obtain the fast wave dispersion relation near the antenna. Figure 4-8 shows the fast wave dispersion relation for typical values of the launched $n_{//}$. The cross field propagation of the fast wave is only allowed for small values of $n_{//}$ (< 10). However, the evanescent of the fast waves in the vicinity of

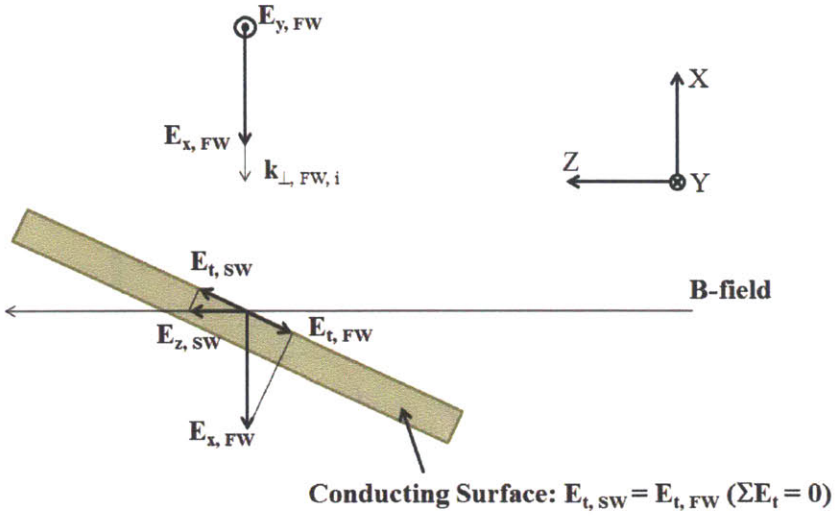

Figure 4-6: A simple 2-D case that demonstrates the principle of fast-to-slow wave coupling at a conducting surface. Note that only the E_x component of the incident FW contributes to the reflected SW.

the ICRF antenna is not as strong as the case for the slow waves ($\frac{1}{|k_\perp|_{,\ SW}} < 1\ mm$): the characteristic e-fold length of the evanescent fast wave is typically several cm for launched $n_{//} \sim 10$.

Similarly to the slow wave it is possible to obtain a simplified algebraic form of the fast wave dispersion relation by considering the launched wave frequency in the vicinity of the ion cyclotron frequency ($\omega \sim \Omega_i$). This condition leads to the following orderings: $n_\perp^2 \sim \epsilon_\perp$, $n_\perp^2 \sim \epsilon_x$, and $n_\perp^2 \ll \epsilon_{//}$. The cold plasma dispersion relation for the fast *ICRF* wave is provided by Equation 4.29 [79]:

$$n_\perp^2 = \frac{\epsilon_x^2 - (n_{//}^2 - \epsilon_\perp^2)^2}{n_{//}^2 - \epsilon_\perp}. \tag{4.29}$$

Note several key features of the dispersion curves shown in Figure 4-8. 1) The fast ICRF wave dispersion becomes that of a vacuum electromagnetic wave in the very low plasma density region: $n_\perp^2 + n_{//}^2 = 1$. The vacuum wave with a real $n_{//} > 1$ value is evanescent in the cross field direction as $n_\perp^2 < 0$. 2) The transition between the vacuum region and the propagating region is defined by $n_\perp = 0$ and corresponds to the condition $\epsilon_x + \epsilon_\perp = n_{//}^2$. 3) For a particular case of $n_{//} = 10$ or higher the

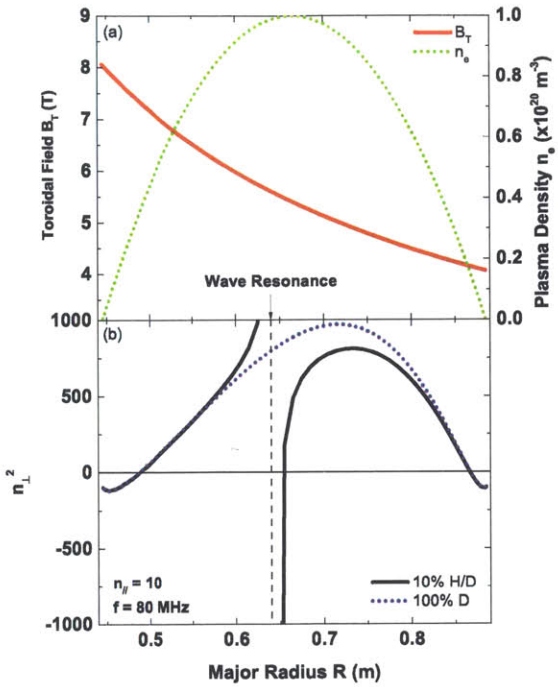

Figure 4-7: Radial profiles of (a) the toroidal magnetic field and the plasma density and (b) of the ICRF wave dispersion. The wave dispersion is shown for pure deuterium plasmas and for plasmas with 10% hydrogen minority fraction. The launched index of refraction is $n_{//} = 10$ and the launched wave frequency $f = 80\ MHz$.

vacuum region extends over the entire plasma boundary region occupied by the ICRF antenna. As a result, the fast wave must first tunnel across the vacuum region (1-2 cm in radial extent on Alcator C-Mod) before it becomes propagating in the high density core region. The characteristic e-folding length of the fast wave evanescence in the vacuum region is $\frac{1}{|k_\perp|} = \frac{c}{|n_\perp|\omega}$, which is several cm long for typical launched $n_{//}$ values of 10-20. As a result, most of the launched ICRF power tunnels into the core plasma region.

In order to solve for the plasma potential enhancement in the case of the fast-to-slow wave coupling theory the sheath, once again, is modeled as a thin vacuum-like region of thickness Δ. The sheath modifies the conducting boundary condition $\mathbf{s} \times \tilde{\mathbf{E}} = 0$ to the form:

$$\mathbf{s} \times \mathbf{E} = \nabla \left(\frac{\Delta}{\epsilon_{sh}} D_n^{(sh)} \right), \tag{4.30}$$

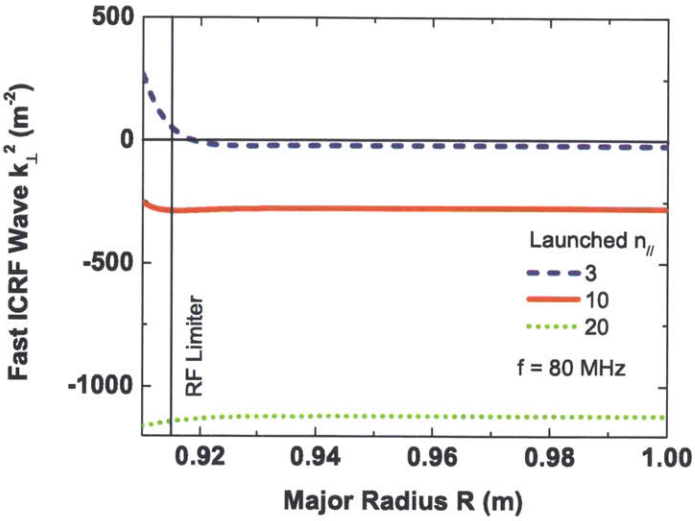

Figure 4-8: A typical cold wave dispersion relation for a fast ICRF wave launched at the low field side of a typical Alcator C-Mod discharge. $B_{To} = 5.4\ T$, $R_o = 0.67\ m$, launched $n_{//} = 3$ (dashed blue curve), 10 (solid curve), and 20 (dotted curve), launched $f = 80\ MHz$. The main limiter is located at $R = 0.910\ m$. Deuterium plasma. The plasma density profile is shown in Figure 4-3.

where $D_n^{(sh)}$ is the component of the displacement vector $\mathbf{D}$ normal to the surface. The RF-rectified plasma potential can now be obtained as: $\Phi_{RF} = -\Delta D_n^{(sh)}$.

One generally has to resort to a numerical solution, however, it is possible to obtain a limiting form of the resulting slow wave $\tilde{E}_{//}$ for the case of a fast wave propagating in vacuum and coupling to an electrostatic slow wave [79], a case that is characteristic of fast waves propagating in the low density plasmas in the shadow of the limiters:

$$\left|\tilde{E}_{//}\right| \propto \left|\tilde{E}_{FW}\right|_i (|n_\perp|_{FW,i} - |n_\perp|_{FW,r}) B_\perp B_T, \tag{4.31}$$

where $|n_\perp|_{FW,i}$ is the magnitude of the perpendicular (to the background magnetic field) component of the index of refraction of the incident fast wave, $|n_\perp|_{FW,r}$ is the magnitude of the perpendicular component of the index of refraction of the reflected fast wave, $B_\perp$ is the perpendicular (to the surface) component of the background magnetic field and B_T is the toroidal component of the background magnetic field ($B_T \approx B$). Using Equation 4.31 and the cold plasma dispersion relation we can reconstruct the expected radial profile of the excited slow wave and, hence, the ex-

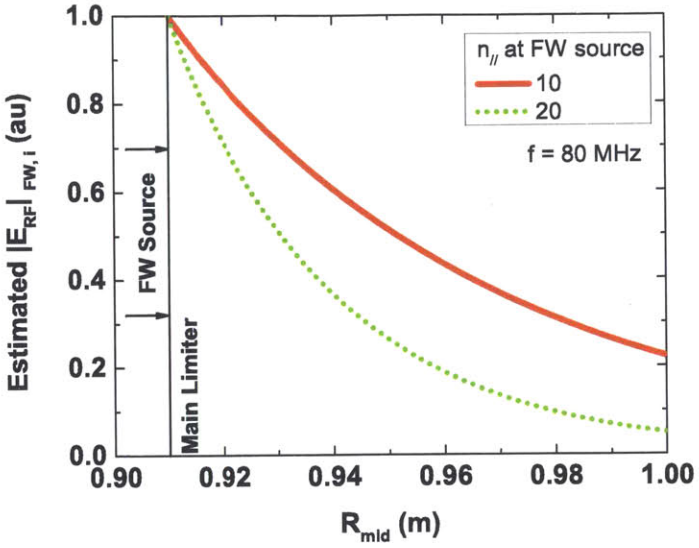

Figure 4-9: An estimated FW electric field amplitude radial profile incident into the limiter shadow on Alcator C-Mod.

pected radial profile of FW rectification in the limiter shadow of Alcator C-Mod. To estimate the cold plasma dispersion we used a realistic radial plasma density profile measured in the shadow of Alcator C-Mod plasma, see Figure 4-3. We also used a realistic toroidal magnetic field profile: $B_{To} = 5.4\ T$, $R_o = 0.67\ m$, $B_T = \frac{B_{To}R_o}{R_{mid}}$. The fast wave is assumed to be incident from the main plasma direction ($R_{mid} < 0.91\ m$), which is characteristic of launched FWs that are scattered or otherwise unabsorbed in the core plasma. The $n_{//}$ spectra at the limiter are typical of those launched by Alcator C-Mod ICRF antennas. The shape of the profiles is an exponential curve that peaks at its source: $|E_{RF}|_{FW,i} \propto e^{-|k_\perp|R_{mid}}$, see Figure 4-9. The radial shape of the excited $\tilde{E}_{//}$ and, hence, Φ_{RF} does not necessary follow the shape of $|E_{RF}|_{FW,i}$, as the surface geometry and the reflected fast wave amplitude must also be accounted (Equation 4.31).

Equation 4.31 is a simple approximation of the fast wave rectification mechanism, yet it provides several key insights into how rectification in the presence of fast waves takes place in a tokamak. The product $B_\perp B_T$ shows that in the vicinity of a rapidly changing surface geometry, such as the plasma facing side of the main limiters, we expect to find large gradients in the plasma potential enhancement. The potential

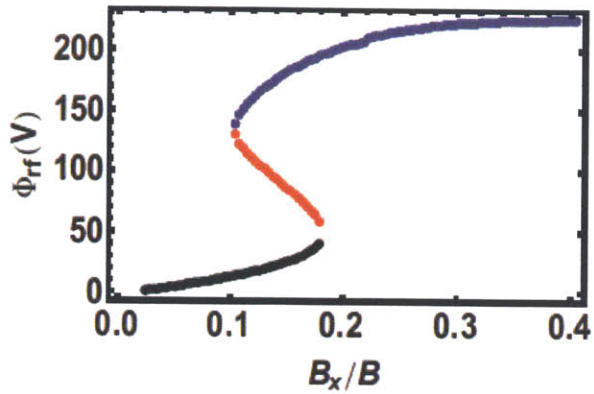

Figure 4-10: An example of the FW-rectified plasma potential (Φ_{RF}) dependence on the magnetic field component normal to the surface $B_x = B_\perp$. The local parameters were: $f = 60\ MHz$, $|n_\perp| = 30$, $n_e = 2 \times 10^{18}\ m^{-3}$, $T_e = 10\ eV$, $B = 3\ T$, and $|E_{FW}| = 2\ kV/m$. Different colors correspond to different solution branches of the Φ_P vs. B_x relation. The figure is reproduced from [79] with the permission of the authors.

would be at its lowest on field lines, which are nearly tangential to the material surface ($b_\perp = 0$, $b_\perp \equiv B_\perp/B_T$) and would exhibit a maximum on field lines which are nearly normal to the surface ($b_\perp = 1$), see Figure 4-10. The physical mechanism responsible for generating larger potentials for the nearly normal magnetic field geometry is due to the larger electric field amplitude of the excited slow wave, as shown in Figure 4-11.

Multiple additional features of the fast wave rectification mechanism are obtained once one carries out a complete numerical solution for $\tilde{E}_{//}$ [79]. These include an appearance of multi-root solutions, for example in Φ_P vs. $\tilde{E}_{FW}$ (Figure 4-12), Φ_P vs. local n_e (Figure 4-13), and Φ_P vs. $|n_\perp|$ (Figure 4-14) dependencies [79]. Experimentally, one would expect to observe threshold-like dependencies in the vicinity of a multi-root solution, as multiple values of the plasma potential are theoretically allowed for a given experimental condition. The physical reason for the appearance of a multi-root solution is due to the resonant response of the plasma inductance and the sheath capacitance to $\tilde{E}_{//}$ [79].

To summarize, the key (and testable) findings of the fast wave rectification theory are listed below. 1) The fast wave E-field does not directly cause sheath rectifica-

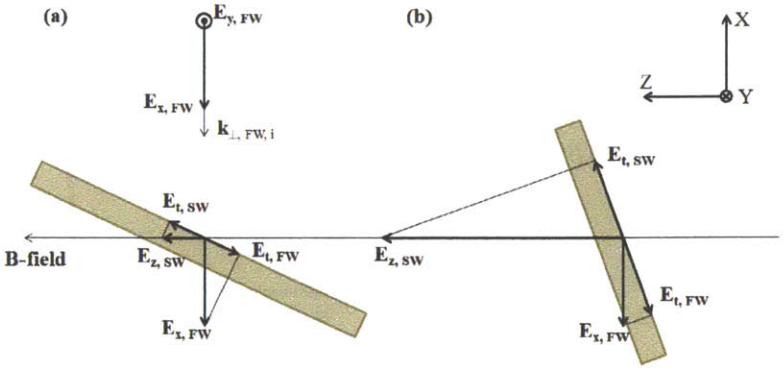

Figure 4-11: Demonstration of the effect of the angle between the surface normal and the magnetic field. (a) for B-field nearly tangential to the surface and (b) for B-field nearly normal to the surface.

tion, the fast wave must first couple to a slow wave at a conducting surface and the slow wave E-field is then responsible for sheath rectification. 2) The fast wave rectification is expected to affect regions that do not necessarily magnetically map to active antennas, yet are accessible to unabsorbed/reflected fast waves from the plasma core. 3) The FW-rectified plasma potentials are expected to peak in regions with the strongest FW E-field amplitude. These are typically surfaces that are closest to the plasma core, the region where fast waves can propagate. 4) The surface geometry with respect to the background magnetic field is expected to play a role in determining the strength of the FW-induced plasma potentials as the details of the fast-to-slow wave E-field coupling depend on the angle between the static magnetic field and the surface normal. 5) The FW-induced plasma potential is expected to increase with an increase in the perpendicular index of refraction of the fast wave. Therefore, discharges heated with fast waves with a strongly upshifted wave spectrum are expected to have the highest enhancement of the plasma potential.

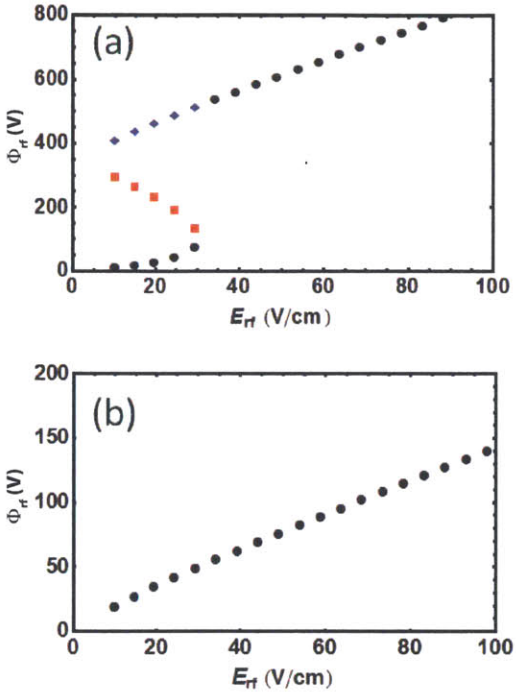

Figure 4-12: Examples of the FW-rectified plasma potential dependence on the FW electric field strength for (a) $|n_\perp| = 30$ and (b) $|n_\perp| = 100$. The local parameters were: $f = 80\ MHz$, $B = 3.9\ T$, $T_e = 10\ eV$, and $n_e = 6 \times 10^{18}\ m^{-3}$. Different colors correspond to different solution branches of the Φ_P vs. $\tilde{E}_{FW}$ relation. The figure is reproduced from [80] with the permission of the authors.

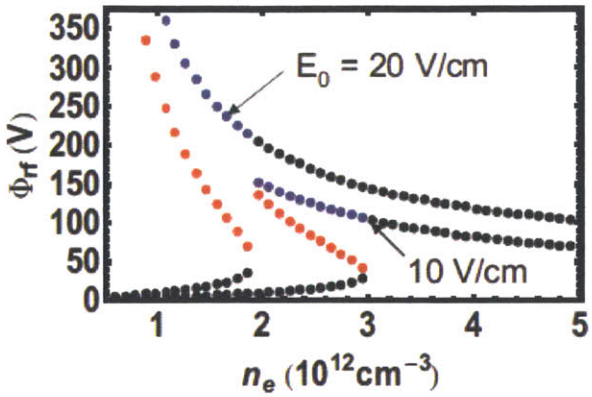

Figure 4-13: An example of the FW-rectified plasma potential as a function of the local plasma density. The local parameters were: $f = 60\ MHz$, $|n_\perp| = 30$, $T_e = 10\ eV$, $B = 3\ T$, and $\frac{B_\perp}{B} = 0.2$. Different colors correspond to different solution branches of the Φ_P vs. n_e relation. The figure is reproduced from [79] with the permission of the authors.

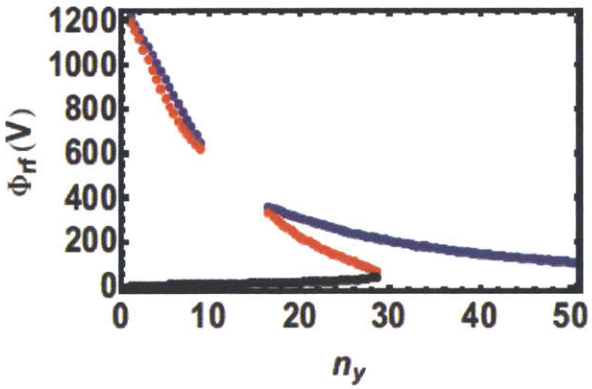

Figure 4-14: An example of the FW-rectified plasma potential as a function of the FW spectrum. $n_y = |n_\perp|$. The local parameters were: $f = 60\ MHz$, $n_e = 2 \times 10^{18}\ m^{-3}$, $T_e = 10\ eV$, $B = 3\ T$, $\frac{B_\perp}{B} = 0.2$, and $|E_{FW}| = 2\ kV/m$. Different colors correspond to different solution branches of the Φ_P vs. n_y relation. The figure is reproduced from [79] with the permission of the authors.

Chapter 5

ICRF-enhanced potentials: experimental results on slow-wave rectification

An extensive survey of plasma potential enhancement in ICRF-heated deuterium plasmas was carried out on Alcator C-Mod over several run campaigns. Measurements were made in the SOL on the outboard side of the core plasma on magnetic field lines that both directly mapped and did not map to active antennas. Plasma discharges were heated with toroidally- and field-aligned ICRF antennas (Figures 5-1 and 5-2). Studies were performed several days after machine boronization [64] to minimize the impact of boron films on the plasma sheath formation and/or probe function. Significant plasma potential enhancement ($\Phi_P > 100\ V$, all potential measurements are with respect to the grounded vacuum vessel) is observed both on those field lines that magnetically map and those that do not map to active ICRF antennas. These potentials are high enough to induce sputtering of Mo PFCs by incident deuterium ions [82]. For comparison, plasma potentials in Ohmic discharges in the vicinity of the main limiter are typically $\sim$10 V or less.

Slow waves directly launched by the active antennas propagate primarily along the static magnetic field lines [76]. As a result, magnetic mapping relation between the probes and active antennas is a key property that distinguishes what type of sheath

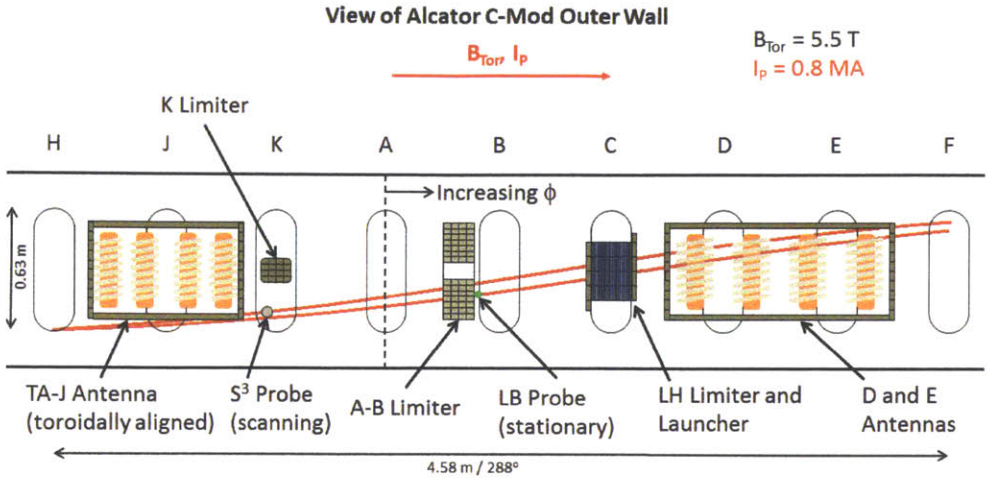

Figure 5-1: The probe arrangement used to characterize plasma potential enhancement with the J antenna in the toroidally-aligned (TA) configuration.

rectification, slow-wave vs. fast-wave induced, takes place. At this point several definitions are introduced that describe the magnetic mapping relation between active ICRF antennas and the probes. A probe is designated as "mapped" to some part of an antenna if first, the magnetic flux tube the probe is on can be directly traced/mapped to the antennas, and second, there is no physical object that blocks free travel of plasma from the antenna to the probe. An example of the mapped probe is the S^3 which is mapped to the corner of the TA-J antenna as shown in Figure 5-1. Note that the S^3 probe is no longer mapped to the FA-J antenna, as the field lines now pass either below or in front of the antenna. However, most locations in the SOL do not have direct magnetic connection to active ICRF antennas, i.e. field lines traced from these locations cannot be followed continuously to the antennas. The "unmapped" probes reside on field lines that, when continuously traced, never intercept active ICRF antennas. As an example, the ASP and UA probe stations are unmapped to the D and E antennas (Figure 5-2). The third and final group of field lines is the "blocked" group. The probes are blocked when the field lines are traced from the probes to active ICRF antennas, but happen to intercept a passive limiter structure before reaching the antenna. As an example, the ASP and UA probe stations are blocked to the FA-J antenna (Figure 5-2). Refer to Figures 3-19, 3-20, and 3-21 for

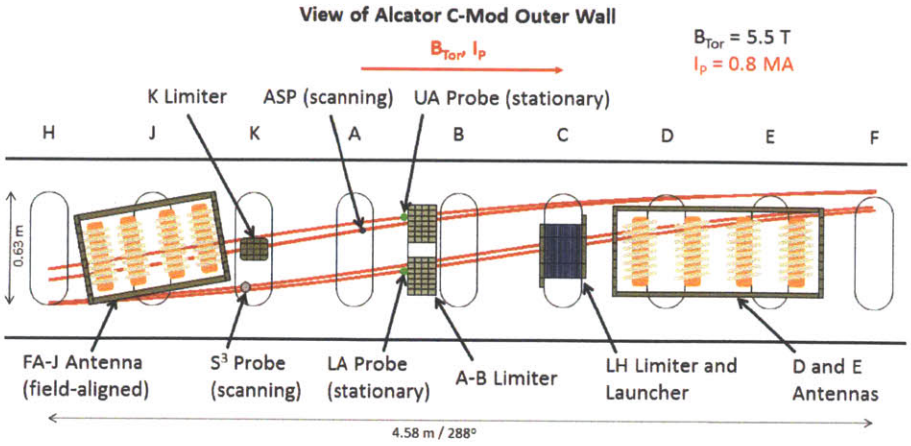

Figure 5-2: The probe arrangement used to characterize plasma potential enhancement with the J antenna in the field-aligned (FA) configuration.

the detailed poloidal, toroidal, and radial positions of the probe stations, respectively.

A large variety of plasma discharges with different discharge parameters was examined. Both L- and H-mode discharges were examined. The key difference between the two modes is the radial plasma density profile in the SOL: the H-mode is characterized by a reduced cross field particle transport near the separatrix and, as a result, has a narrow radial plasma density profile in the SOL with the plasma density values typically an order of magnitude lower than in the L-mode [14]. Several key plasma parameters were also varied within a single discharge mode. Examples include the core plasma density, which impacts the plasma density in the SOL, and the ICRF resonance position, which impacts the fast wave absorption in the core. Probe studies were performed in a variety of plasma shapes (lower single null or LSN, upper single null or USN, inner wall limited or IWL) and measurements were performed on plasma flux tubes that directly map (along magnetic B-field) and do not map to active ICRF antennas. The poloidal magnetic field mapping was also varied by either changing the plasma current or the toroidal magnetic field strength.

Overall, a number of distinct ICRF-driven mechanisms that enhance the plasma potential in the SOL of Alcator C-Mod are identified. 1) Plasma potential enhancement with features that are consistent with the slow wave rectification. In this case the enhancement is due to the slow waves that are directly generated by the active

antenna. This type of plasma potential enhancement is the subject of the current chapter. 2) Plasma potential enhancement consistent with the fast-to-slow wave coupling and then rectification where the fast wave source is in the form of unabsorbed and/or reflected fast waves from the plasma core. In this case the enhancement is due to the slow waves that are generated by fast waves reflecting at conducting material surfaces. The experimental evidence for the second mechanism, which is often called fast wave rectification [79], is provided in the following chapter.

5.1 ICRF-enhanced plasma potentials: measurements on probes mapped to active ICRF antennas

According to the slow wave rectification theory [76, 77] plasma flux tubes that directly intercept active ICRF antennas and reside in regions where the plasma density is below the lower hybrid (LH) cutoff ($n_e < n_{LH} \approx 2\times10^{17}\ m^{-3}$ on Alcator C-Mod) allow for plasma potential enhancement by slow waves directly excited by the active ICRF antennas. If the plasma density rises above its value at the lower hybrid resonance, the slow wave becomes strongly evanescent in the radial direction: the slow wave amplitude is reduced by a factor of $\frac{1}{e}$ in a radial distance of $< 1\ mm$ for $n_{//} > 10$. Note that Alcator C-Mod's previous plasma potential measurements in [23, 29] belong to the mapped category. The previous studies used the lower B station, which, before the installation of the lower hybrid limiter and launcher, mapped directly to the D antenna and the lower A station, which mapped directly to the TA-J antenna [23, 29]. The mapped results in the current study are limited to the S^3 probe measurements, which map directly to the corner of the TA-J antenna.

The previous studies of the plasma potential enhancement [23, 29] only used stationary emissive probes to measure ICRF-enhanced plasma potentials. The key results of the study showed that plasma potentials $> 100\ V$ were observed for the probes that were directly mapped to the active antennas [23]. Generally, the highest

potentials were observed at the highest ICRF powers, however, it was not always the case that increases in the ICRF power resulted in a proportional increase in the plasma potential enhancement [23]. In fact, large variations in the plasma potential were observed for the case of an almost constant ICRF power level (Figure 1-8) [23]. No additional probes were used in the previous studies to determine the influence of the local plasma density and/or ICRF wave amplitude variations.

As discussed in the theory section [76, 77], one of the most defining features of the slow wave rectification theory is the predicted appearance of the rectified plasma potentials when the dimensionless rectification parameter Λ_o is above a threshold value of unity to allow strong Φ_P rectification. The easiest methods to scan the value of Λ_o are either through varying the local plasma density, for example by changing the core plasma density via a gas puff, or through changing the ICRF voltage source amplitude (V_o), which is equivalent to changing the level of launched ICRF power ($V_o \propto P_{RF}^{1/2}$).

A threshold-like appearance of significant plasma potentials (>100 V) is observed when the local plasma density is scanned over a wide range. An example of such a threshold is shown in Figure 5-3. The local plasma density scan was achieved by scanning the core plasma density using a deuterium gas puff. The plasma potential measurements were made using the S^3 emissive probe, with the probe positioned 3 mm behind the main limiter: $\Delta_{probe} = 3\ mm$, $\Delta_{probe} \equiv R_{probe} - R_{limiter}$, where all radial distances are mapped to the midplane. $R_{limiter} = 0.910\ m$. The TA-J antenna was used to inject ICRF power and the S^3 probes were directly mapped to the active antenna.

The local plasma density was measured with the S^3 ISP probe. In this case, the guard/wall electrode of the ion sensitive probe was treated as a flush-mounted probe, where the I_{sat} values on the ISP wall were calibrated against the I_{sat} values measured with the S^3 Langmuir probe at a later time. The calibration factor between the I_{SAT} values on the ISP wall and the Langmuir probe is shown in Figure 5-4 and is ~ 5. The local plasma density values are estimated for deuterium ions, $A_{LP\ probe} = 7.6 \times 10^{-6}\ m^{-2}$, and $T_e = 10\ eV$.

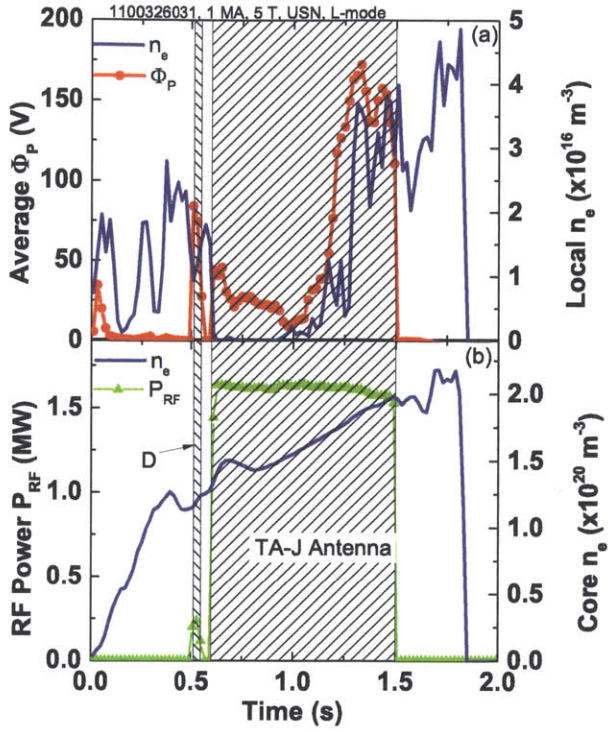

Figure 5-3: An example of an ICRF-heated plasma discharge on Alcator C-Mod demonstrating a plasma potential enhancement threshold with the local plasma density. The shown profiles are (a) Φ_P and local n_e and (b) launched ICRF power and core n_e. S^3 probe data. $\Delta_{probe} = 3\ mm$, $\Delta_{probe} \equiv R_{probe} - R_{limiter}$, where all radial distances are mapped to the midplane. $R_{limiter} = 0.910\ m$. Active TA-J antenna only (dipole). The probes are mapped to the active antenna.

Using experimental values applicable to ICRF-heated discharges on Alcator C-mod, it is possible to estimate the experimentally determined dependence between the plasma potential and Λ_o. This dependence is shown in Figure 5-5 for several ICRF-heated plasma discharges. We used the numerical constant of order unity $\alpha = 0.6$, the local $T_e = 10\ eV$, the ICRF source voltage $V_o = 200\ V$ [85], and the characteristic scale length of the launching structure $a = 0.1\ m$, which is determined by the ICRF current strap toroidal width. Note that the operating frequency of the TA-J antenna for this particular data set was 70 MHz, not the typical 80 MHz launch frequency that is used to obtain the theoretical estimate of Λ_o. Λ_o scales as $\sim \epsilon_{//} \sim \frac{1}{\omega^2}$. Therefore, a 10 % change in the value of the launched frequency

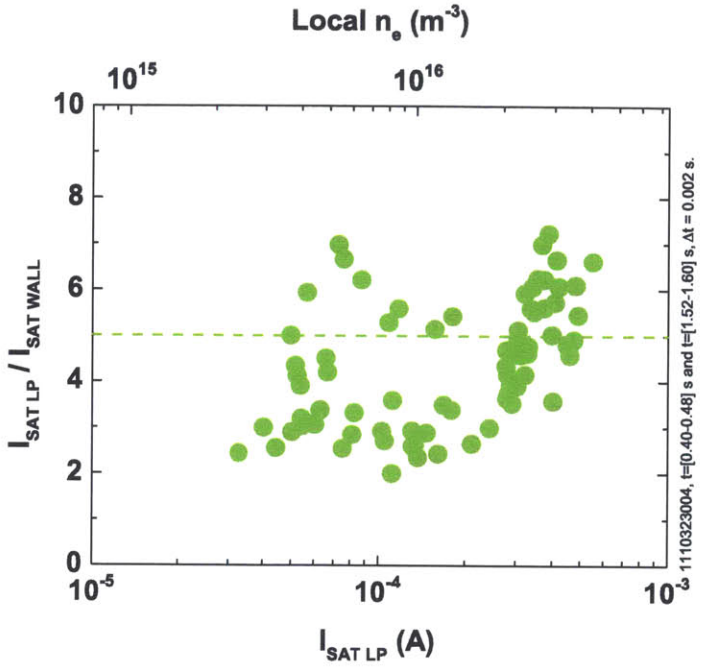

Figure 5-4: Ratio between the $I_{SAT\ LP}$ values measured with the S^3 Langmuir probe (LP) and the $I_{SAT\ WALL}$ values measured with the ISP wall electrode as a function $I_{SAT\ LP}$. The local plasma estimate is for deuterium ions, $A_{LP\ probe} = 7.6 \times 10^{-6}\ m^{-2}$, and $T_e = 10\ eV$. S^3 probe data.

results in a 30 % change in the value of Λ_o, which is within the range of the data scatter shown in Figure 5-5. The toroidal magnetic field strength was 5.3 T. The theoretically computed values of the plasma potential correspond to the sum of the thermal plasma potential drop ($3 \times T_e/e = 30\ V$) and the rectified plasma potential drop based on Equation 4.27. Λ_o was varied by changing the plasma density at the probe, which, in turn, was achieved by scanning the line-averaged value of the core plasma density: $n_{e\ core} = 1.22 - 1.98 \times 10^{20}\ m^{-3}$. Additionally over a set of repeated discharges the S^3 probe was radially moved to different locations; due to the intrinsic steep radial profiles in plasma density in the SOL this provides for a wide variation in local plasma density. Δ_{probe} refers to the distance between the emissive probe major radius location and the plasma facing side of the main limiter ($R_{limiter} = 0.91\ m$): $\Delta_{probe} \equiv R_{probe} - R_{limiter}$, where the major radius distances are mapped to the midplane. Note that a positive Δ_{probe} indicates the probe is "behind"

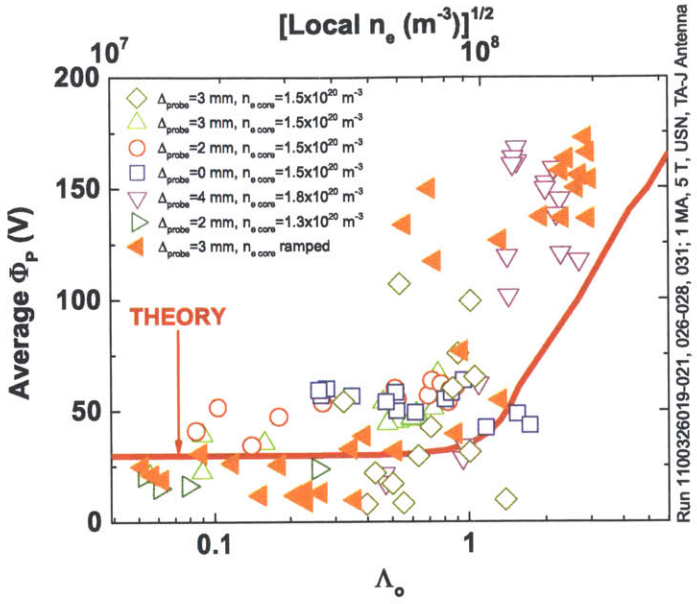

Figure 5-5: An experimentally determined dependence between measured plasma potential enhancement and dimensionless sheath parameter Λ_o. The line corresponds to the trend expected from the slow-wave theory [76]. Active TA-J antenna only (dipole). S^3 probe data. $\Delta_{probe} \equiv R_{probe} - R_{limiter}$, where all radial distances are mapped to the midplane. $R_{limiter} = 0.910\ m$. The probes are mapped to the active antenna.

the limiter i.e. further away from the SOL. Also note that the local ICRF limiter is located at $R_{ICRF\ limiter} = 0.915\ m$ or 5 mm "behind" the main limiter.

As can be seen in Figure 5-5, the threshold Λ_o value is of order unity. This result is expected from the slow wave rectification theory [76] and corresponds to the local electron density of $n_e \sim 10^{16}\ m^{-3}$. Once the threshold is crossed and the plasma potential becomes strongly enhanced to values $> 100\ V$, Φ_P appears to saturate at 100-200 V with little dependence on the RF power. The lack of Φ_P dependence on the RF power is illustrated in Figure 5-6. For each of the two data sets shown in Figure 5-6, the value of the line-averaged plasma density was scanned over a range of $n_{e\ core} = 1.22 - 1.98 \times 10^{20}\ m^{-3}$, while the launched ICRF power was constant at either 1.1 MW or 1.6 MW. The S^3 probe was positioned at $\Delta_{probe} = 3\ mm$.

As can be seen from Figure 5-6, the local plasma density is the plasma parameter that shows the strongest correlation with ICRF-enhanced plasma potentials: once

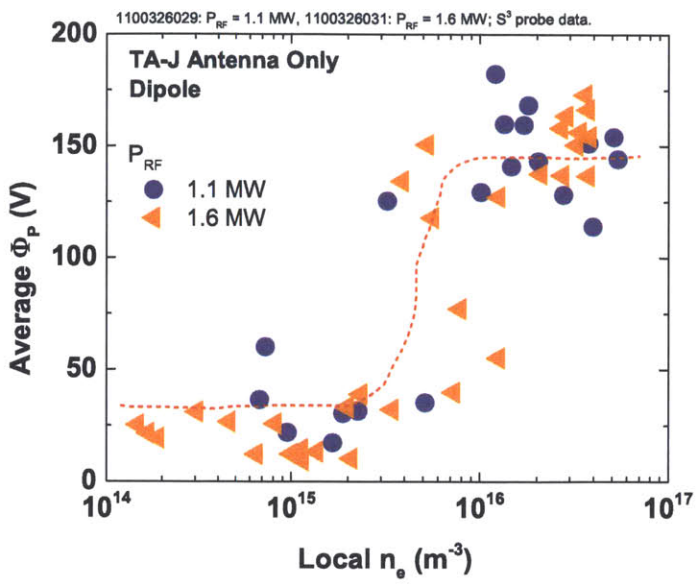

Figure 5-6: ICRF-enhanced plasma potentials vs. the local plasma density at different levels of launched ICRF power. S^3 probe data. $\Delta_{probe} = 3\ mm$, $\Delta_{probe} \equiv R_{probe} - R_{limiter}$, where all radial distances are mapped to the midplane. $R_{limiter} = 0.910\ m$. Active TA-J antenna only (dipole). The probes are mapped to the active antenna. The dashed line is to guide the eye.

the local plasma potential exceeds the value of $n_e \sim 10^{16}\ m^{-3}$, the plasma potential reaches values of $\Phi_P \geq 100\ V$ and the value of the enhanced potential is weakly sensitive to the level of ICRF power as long as the local plasma density remains above the threshold value.

Experimentally, it is found that the presence of ICRF power affects the local plasma density (Figure 5-7). The general trend for the "mapped" case is that the local plasma density decreases with increasing ICRF power. Note that the trend is reproduced at each radial location. Also note that the sparseness of the n_e data for the ICRF-heated cases in Figure 5-7 (b) is due to the reduction in the local plasma density value below $n_e \sim 10^{14}\ m^{-3}$. This density value is set by the minimum level of the I_{sat} signal on the ISP wall that can be distinguished above the electroncs noise level. In order to self-consistently include the effect of ICRF power and ICRF-induced plasma potentials on the local plasma density profile, it is necessary to account for the radial gradients in the plasma potential profile [72]. The radial shape of the plasma

potential profile is responsible for generating radial DC electric fields ($E_r = -\nabla_r \Phi_P$). These radial electric fields begin to generate $\mathbf{E} \times \mathbf{B}$ flows along equipotential surfaces in the SOL and the net effect of these flows is to modify the values of the local plasma density [72]. Note that the average ICRF-induced radial electric fields across the profiles in Figure 5-7 are typically $|E_r| = 50\ V/0.01\ m = 5 \times 10^3\ V/m$ and the associated drop in the local plasma density is a factor of ten or more. For comparison, the radial electric fields in Ohmic discharges are typically 500 V/m. Also note that the trend of higher Φ_P values with higher n_e remains consistent with the slow wave enhancement mechanism across the radial profile, with the exception of the point at the limiter surface ($\Delta_{probe} = 0\ mm$): the plasma potential now becomes higher at the lower plasma density. Such a Φ_P vs. local n_e trend suggests that the slow wave rectification mechanism may not be the only process responsible for the ICRF enhancement of the plasma potential on Alcator C-Mod.

The slow-wave sheath rectification mechanism is only applicable for a *propagating* slow wave [76]. As the local plasma density is raised above its value at the lower hybrid resonance ($n_{LH} = 2.5 \times 10^{17}\ m^{-3}$ at $f = 80\ MHz$ and $n_{LH} = 1.8 \times 10^{17}\ m^{-3}$ at $f = 70\ MHz$), the slow wave becomes strongly evanescent in the perpendicular direction ($n_\perp^2 < 0$) and the slow-wave rectification theory is no longer applicable. Experimentally, it is observed that the mapped ICRF-enhanced plasma potentials become greatly reduced as the local plasma density is raised above $\sim 10^{17}\ m^{-3}$ (Figure 5-8 (b)). Figure 5-8 (b) reveals that significant plasma potential enhancement is confined to a narrow plasma density range $10^{16} < n_e < 10^{17}\ m^{-3}$. This result is in agreement with the slow wave rectification mechanism [76]: the lower bound corresponds to the plasma density value at which the sheath rectification parameter Λ_o is unity, while the upper bound corresponds to the plasma density at the lower hybrid resonance, above which the slow wave becomes strongly evanescent. The slow wave rectification theory is no longer applicable for the case of $n_e > n_{LH}$.

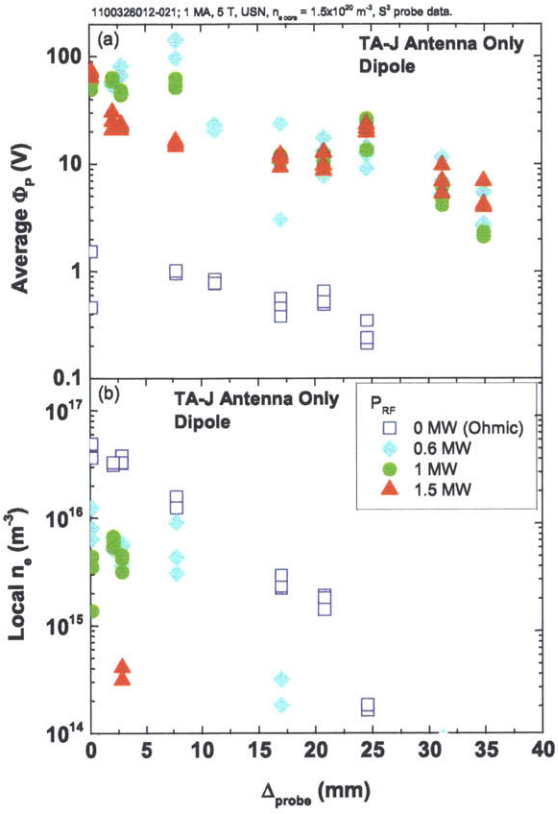

Figure 5-7: Radial (a) plasma potential and (b) plasma density profiles in the shadow of the limiter in the vicinity of an active ICRF antenna. $\Delta_{probe} \equiv R_{probe} - R_{main\ limiter}$, $R_{main\ limiter} = 0.910\ m$, all radial distances are mapped to the midplane. The profiles are shown for various levels of ICRF power. S^3 probe data. Active TA-J antenna only (dipole). The probes are mapped to the active antenna.

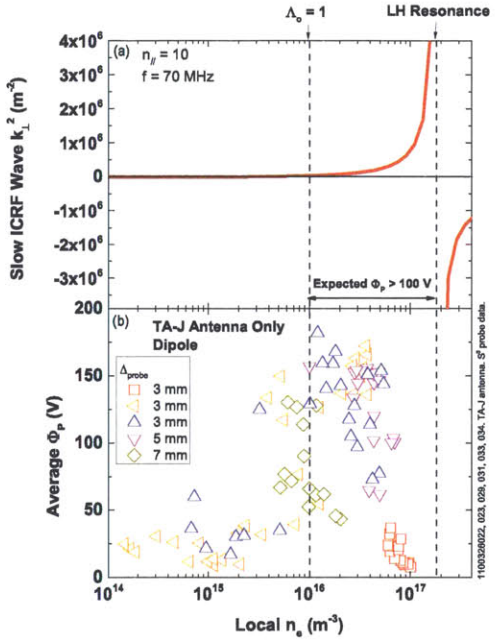

Figure 5-8: (a) slow ICRF wave dispersion relation as a function of the local plasma density; $f = 70\ MHz$ and launched $n_{//} = 10$, LH refers to the lower hybrid resonance, Λ_o is the dimensionless sheath parameter [76]; (b) ICRF-enhanced plasma potentials as a function of the local plasma density. $\Delta_{probe} \equiv R_{probe} - R_{main\ limiter}$, $R_{main\ limiter} = 0.910\ m$, all radial distances are mapped to the midplane. S^3 probe data. Active TA-J antenna only (dipole). The probes are mapped to the active antenna.

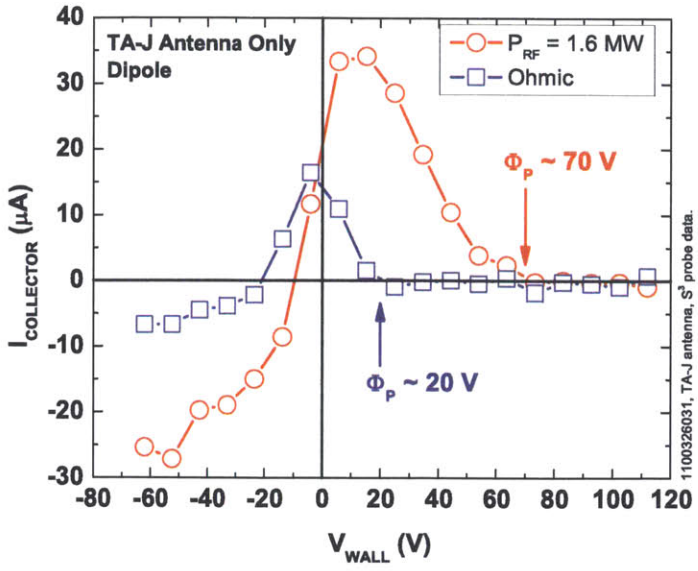

Figure 5-9: Example of the ISP used as a plasma potential diagnostic on Alcator C-Mod in ICRF-heated and Ohmic plasmas. Active TA-J antenna only (dipole). S^3 probe data. $\Delta_{probe} = 3\ mm$. The probe is mapped to the active antenna.

5.2 ISP measurements of the plasma potential on field lines directly mapped to an active ICRF antenna

The plasma potential measurements discussed in the previous section were all carried out with an emissive probe installed on the S^3. However, as the S^3 probe is radially scanned toward the main SOL region ($\Delta_{probe} \leq 0\ mm$), the local plasma density rises past the limit at which the emissive probe can still function as a plasma potential diagnostic, typically $n_e \geq 10^{18}\ m^{-3}$ for the emissive probes on Alcator C-Mod. An ion sensitve probe was installed on the S^3 for the purpose of measuring the plasma potential in high density plasmas. A demonstration of the ISP functioning as a plasma potential diagnostic on Alcator C-Mod is shown in Figure 5-9. To reiterate from Chapter 2, section 2.4, the plasma potential is interpreted from the ISP data as the wall potential at which the collector current vanished. The measurements in Figure 5-9 are shown for Ohmic and ICRF-heated plasmas.

The radial plasma potential profile in the vicinity of the active TA-J antenna (Figure 5-7) suggests that the slow wave does not solely determine the observed Φ_P enhancement. Figure 5-10 (b) demonstrates that in the region radially inboard (i.e. toward the core plasma) of the main limiter ($\Delta_{probe} \leq 0\ mm$) significant Φ_P enhancement (~50 V) is present at all core densities. The field lines in this region no longer directly intercept the active antenna, but rather pass in front of it, and the plasma density is $n_e \geq n_{LH}$ implying that the slow wave is deeply evanescent with the characteristic e-folding decay length of $< 1\ mm$. Note that the plasma potential in this case was measured with the ISP as the plasma density becomes too high for the emissive probe to operate as a plasma potential diagnostic (Figure 5-10 (b)). The large spike in the plasma potential that appears in the Ohmic part of the discharge at Time = 0.1 s in Figure 5-10 (b) is due to the runaway electrons during the start-up phase of the discharge.

Both the ISP and the emissive probe measured Φ_P's agree with each other only in the low plasma density regions (Figure 5-10 (a)). The observed enhancement of the plasma potential in the main SOL region ($\Delta_{probe} \leq 0\ mm$) is consistent with past ASP measurements of the floating potential enhancement of a regular Langmuir probe [23]. Our measurements are also consistent with ICRF-induced radial electric fields that are generated in the main SOL ($R_{mid} < 0.910\ m$) of ICRF-heated discharges on Alcator C-Mod [71]. Therefore, for locations directly magnetically mapped to the active antennas the Φ_P dependence, and its expected threshold with the local plasma density, is broadly consistent with the SW rectification theory [76, 77]. Yet it appears that other mechanisms may be at play at locations not magnetically mapped (5-10 (b)), which will be the subject of the next chapter.

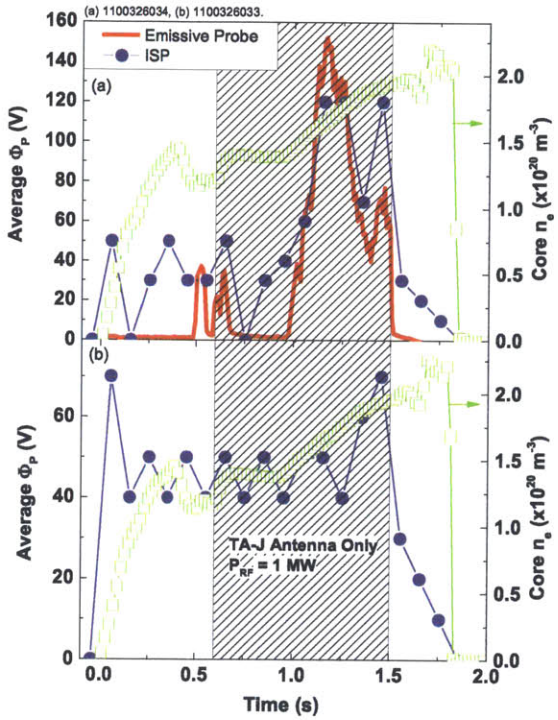

Figure 5-10: ICRF-enhanced plasma potential measurements (a) in the shadow of the local ICRF limiter ($\Delta_{probe} = 7\ mm$ and (b) inboard of the shadow of the TA-J antenna limiter ($\Delta_{probe} = 0\ mm$). Active TA-J antenna only (dipole). S^3 probe data. The probes are mapped to the active antenna in case (a) and unmapped to the active antenna in case (b).

Chapter 6

ICRF-enhanced potentials: experimental results on fast-wave rectification

Direct magnetic mapping is required for the slow waves launched by the active ICRF antenna to produce enhanced plasma potentials at surfaces away from the antenna. However, most locations in the SOL do not have direct magnetic connection to active ICRF antennas, i.e. field lines traced from these locations cannot be followed continuously to the antennas. There are two categories to distinguish here. In the first case the field lines mapped to the toroidal location of the antennas do not intercept the poloidal location of the antennas, i.e. they pass above, below, or inboard of the antennas. These locations are labeled as "unmapped" to the active antennas. In the second case, the field line traced to the toroidal location would intercept the active antenna; however, the field line is intercepted by a physical limiter object. These locations are labeled as "blocked" to the antennas. As an example of this distinction the Upper A (UA) stationary probe in Figure 5-2 is "unmapped" to the D and E antennas, but is "blocked" to the J antenna because the corresponding field lines are intercepted by the K-limiter.

An extensive set of measurements was carried out on the unmapped and blocked groups of field lines with no direct magnetic connection to active ICRF antennas.

It was found that these groups of field lines also experience plasma potential enhancement of over 100 V. These enhanced plasma potentials are inconsistent with rectification of slow waves that are directly launched by the active antennas. Both unmapped and blocked locations are not accessible to directly launched slow waves because the slow waves propagate primarily along magnetic field lines. Therefore, a mechanism other than the slow wave rectification must be responsible for the observed plasma potential enhancement. The observation of ICRF-enhanced potentials in such locations is likely important to understand ICRF-induced impurity generation because it allows the possibility of enhanced impurity sputtering from many more surfaces inside the tokamak. The subject of the following sections will be how ICRF fast waves, re-incident to the boundary plasma due to incomplete absorption in the core, are the primary cause of these enhanced sheaths.

6.1 General observations of ICRF-enhanced plasma potentials in the presence of fast waves

An example of an evolving plasma potential and ICRF wave fields at a magnetically blocked location is shown in Figure 6-1. In this case the LB probe is blocked by the LH limiter and launcher to the active D and E antennas (Figure 5-1). There are several key observations from this example, which motivate further systematic study. First, locations blocked to the directly launched slow waves clearly form enhanced plasma potentials, making such locations a potentially important impurity source. Secondly, an ~80 MHz ICRF wave field with the fast wave polarization ($|E_{RF,\ FW}|$) is measured locally with a $\dot{B}$ probe due to the active antenna. Third, the average values of the plasma potential and the FW field are clearly affected by the ICRF power launched by the active antennae, even if the organizing principle between potential and power is non-monotonic. Fourth, the potential is affected by the relative toroidal distance between the probes and the active antenna (e.g. the potential at the LB probe is lower when the E antenna is on compared to D). Fifth, the Φ_P and FW field intensity

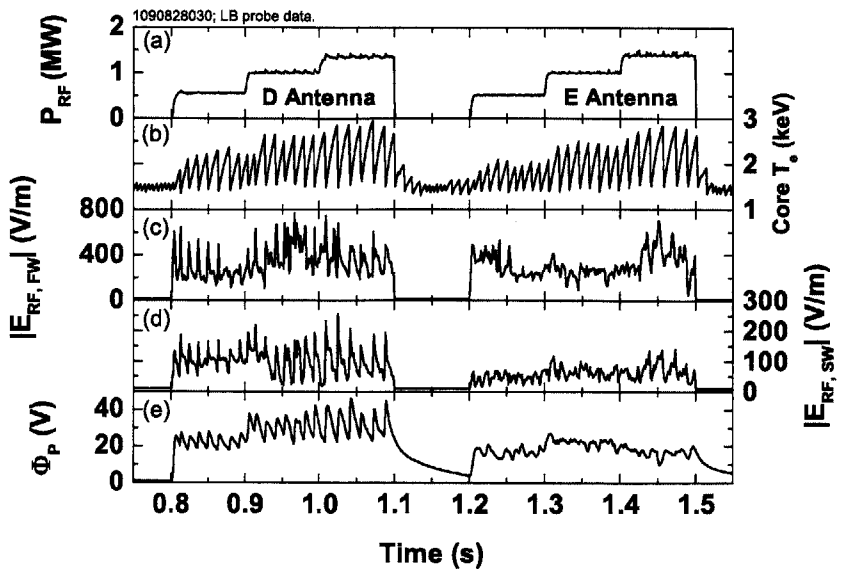

Figure 6-1: Time traces of (a) the launched ICRF power (P_{RF}), (b) the core electron temperature, (c) the fast wave electric field strength at the LB probe station, (d) the slow wave electric field strength at the LB probe station, and (e) the average plasma potential at the LB probe station. Active D or E antenna only (dipole). The probes are blocked to the D and E antennas.

are modulated by the occurrence of core plasma sawteeth indicating a correlation between the FW core behavior/absorption, the FW presence in the boundary, and the enhanced potentials. These observations are now examined in more detail in the following sections.

6.1.1 Effect of sawtooth modulations on fast wave fields

As seen in Figure 6-1 the sawtooth modulations induce major changes in both the RF fields and plasma potentials at magnetically blocked locations. At first glance this would seem surprising because sawteeth are internal magnetohydrodynamic (MHD) instabilities that occur near the magnetic axis of the core plasma, so their link to SOL plasma potentials is not obvious. The $\dot{B}$ measurements show that the FW E-field modulations ($|E_{RF,\ FW}|$) are more than the double in amplitude than the SW modulations (i.e. more than 4× effective RF power in FW than the SW). Yet the SW local amplitude correlates extremely well to the FW amplitude (Figure 6-2) suggesting qualitatively that the SW presence is strongly linked to the FW in this magnetically blocked location. In addition the radial position of the ICRF resonance ($R_{ICRF\ res}$) clearly affects the modulation of the RF field. It is found that the shift of the ICRF resonance location away from the on-axis location ($\Delta_{res} \equiv R_{ICRF\ res} - R_o$, $R_o = 0.67$ m) influences the FW strength, modulated by sawteeth, in the SOL.

While there are considerable differences in sawtooth RF modulation with RF resonance, there is also a discernible trend of increasing FW E-field with RF input power in Figure 6-2. The presence of FW in the boundary implies incomplete absorption of the FW in the core after being launched from the ICRF antenna with dipole phasing, and, therefore, the amplitude of RF E-field would scale as $P_{RF}^{1/2}$ at constant absorption fraction. In Figure 6-2 the picture is complicated by the fact that the sawtooth modulated amplitude is simultaneously affected by the RF power and the resonance location, which can both affect sawtooth amplitudes [31]. Therefore, quantitative trends are difficult to extract in this case. Conversely the trend of RF E-field and P_{RF} is readily quantified with monopole ICRF phasing as seen in Figure 6-3, where the average (not modulated) SOL RF E-field follows closely the expected $P_{RF}^{1/2}$. In this case of monopole phasing there is effectively no measurable heating of the core plasma by the FW, and thus no effect on sawteeth and one expects almost all of FW power reflected toward the boundary. Thus, the monopole phasing case is an excellent indicator to the importance of unabsorbed FW in affecting RF fields in the

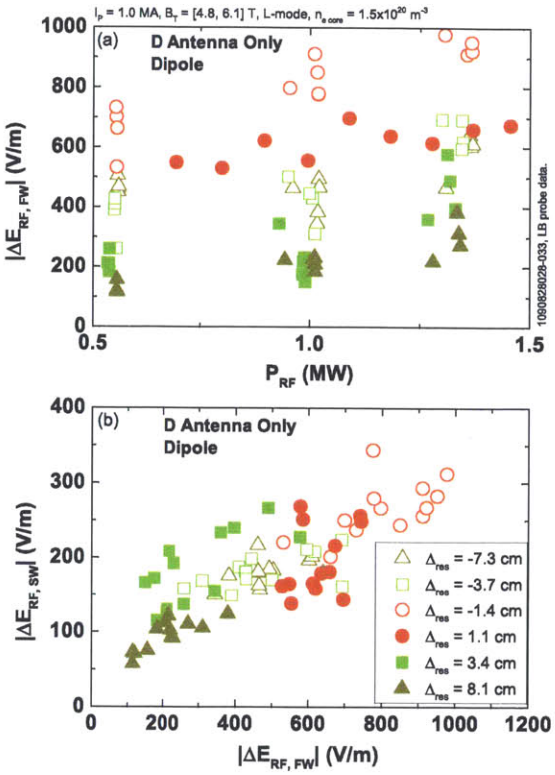

Figure 6-2: (a) sawtooth-induced modulation amplitude in the fast wave electric field strength as a function of the launched ICRF power and (b) relation between sawtooth-induced modulation amplitude of the SW and FW E-fields. Different symbols denote varying positions of the ICRF resonance ($R_{ICRF\ res}$) with respect to the on-axis major radius location (R_o): $\Delta_{res} \equiv R_{ICRF\ res} - R_o$, $R_o = 0.67$ m. Active D antenna only (dipole). LB probe data. The probes are blocked to the active antenna.

boundary.

The sawtooth amplitude and activity in the plasma core influence the strength of the fast wave fields in the SOL. This dependence is more pronounced for the active ICRF antenna that is toroidally nearest to the probes (Figures 6-1 and 6-4). The sawtooth amplitudes were varied by changing the toroidal B field and, thus, moving the ICRF resonance with respect to $R_o = 0.67$ m while keeping other parameters constant. The influence of the sawtooth activity on the strength of the fast wave fields in the SOL has been previously observed on Alcator C-Mod with $\dot{B}$ measurements on the inboard wall [31]. It is speculated that the sawtooth modulated hydrogen minority fraction in the plasma core affects dynamic fast wave core absorption [31].

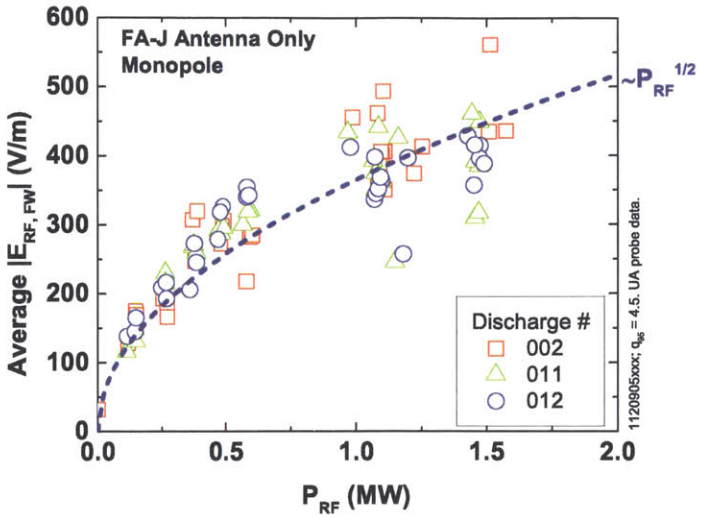

Figure 6-3: Average fast wave electric field strength $|E_{RF,\ FW}|$ as a function of the launched ICRF power. The trends are shown for several reproducible discharges with constant plasma parameters. The expected trend of $|E_{RF,\ FW}| \sim P_{RF}^{1/2}$ is also shown. Active FA-J antenna only (monopole). UA probe data. The probes are blocked to the active antenna.

The current diagnostic set on the LB probe station now directly links the sawtooth-modulated FW absorption to an enhancement of the plasma potential. Comparing Figures 6-4 (a) and 6-4 (b) also shows that the toroidal distance from the active antennas is important, i.e. that a larger RF amplitude (and clearer correlation with sawtooth amplitude) is seen at the location closer to the active antenna. Extensive simulation results of the fast wave absorption and propagation in the core plasmas of Alcator C-Mod show that the fast ICRF wave strength peaks in the vicinity of the active antenna and decays toroidally away from the antenna [86]. Our experimental results are qualitatively consistent with this picture.

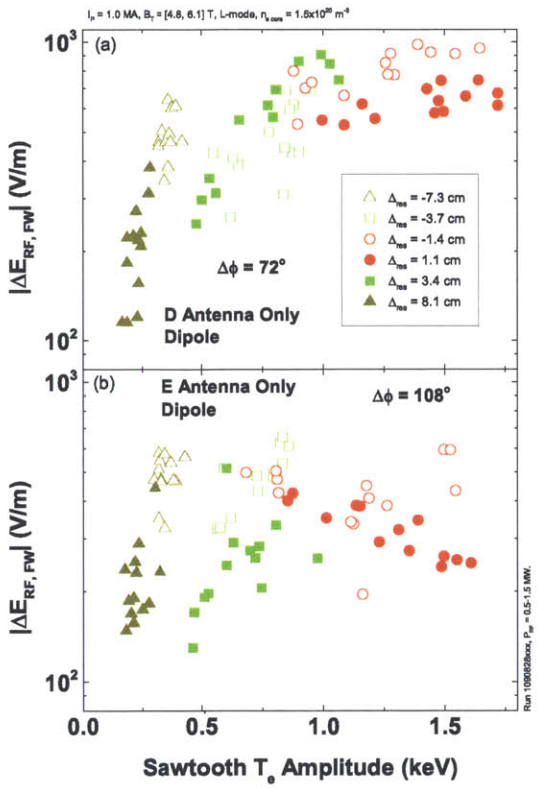

Figure 6-4: The effect of sawtooth T_e modulations on the fast wave electric field strength. (a) active D antenna only (dipole) and (b) active E antenna only (dipole). Symbols denote different positions of the ICRF resonance. The D antenna is toroidally closer to the probe station than the E antenna, see Figure 5-1. LB probe data: $\Delta\phi$ refers to the toroidal spacing between the probe and the active antenna. The probes are blocked to the active antenna.

6.1.2 Correlation between FW fields and plasma potentials

In both the dipole and monopole-heated discharges the amplitude of the plasma potential enhancement follows the strength of the local fast wave electric fields ($|E_{RF,\ FW}|$) (Figures 6-5 and 6-6). The plasma potential enhancement dependence on the local fast wave electric field amplitude is generally stronger than linear as $|E_{RF,\ FW}|$ increases to ~1 kV/m. This trend is consistent with a fast wave rectification theory (Chapter 4, Section 4.4) and is expected due to a nonlinear transition between the lowest, middle, and highest roots of the Φ_P vs. $E_{RF,\ FW}$ relation, as shown in Figure 6-5 (a) for a particular case of $|n_\perp| = 40$ [80]. Once again, it is important to clarify that the FW E-field in the so-called fast wave rectification theory does not directly lead to sheath rectification. Rather, the FW E-field couples to a slow wave at a conducting material surface and the resultant slow wave electric field is responsible for sheath rectification [79]. The theoretically expected trends in Figures 6-5 and 6-6 are estimated using local plasma conditions at the limiter surface ($R_{mid} = 0.91$ m): $n_e = 6 \times 10^{18}\ m^{-3}$, $T_e = 10\ eV$, $B_T = 4\ T$ [80]. The local plasma conditions are assumed constant when estimating the theoretical trends. As the strength of the fast wave electric field is increased, the strength of the ICRF-enhanced Φ_P suddenly transitions to values typically $\Phi_P > 100\ V$, as shown with the red solid curves in Figure 6-5 (a) for the case of $|n_\perp| = 40$ [80].

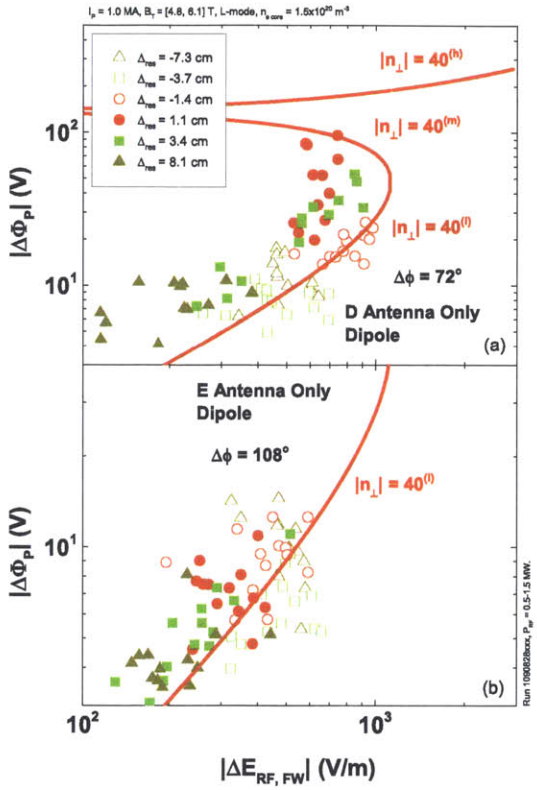

Figure 6-5: Correlations between changes in the plasma potential ($|\Phi_P|$) and the local fast wave electric field amplitude ($|E_{RF,\ FW}|$) for (a) the active D antenna only (dipole) and (b) the active E antenna only (dipole). Symbols denote different positions of the ICRF resonance. The lines are a theoretically expected trend; (l), (m), and (h) refers to the lowest, middle, and highest roots of the Φ_P vs. $E_{RF,\ FW}$ relation, respectively [80]. LB probe data: $\Delta\phi$ refers to the toroidal spacing between the probe and the active antenna. The probes are blocked to the active antenna.

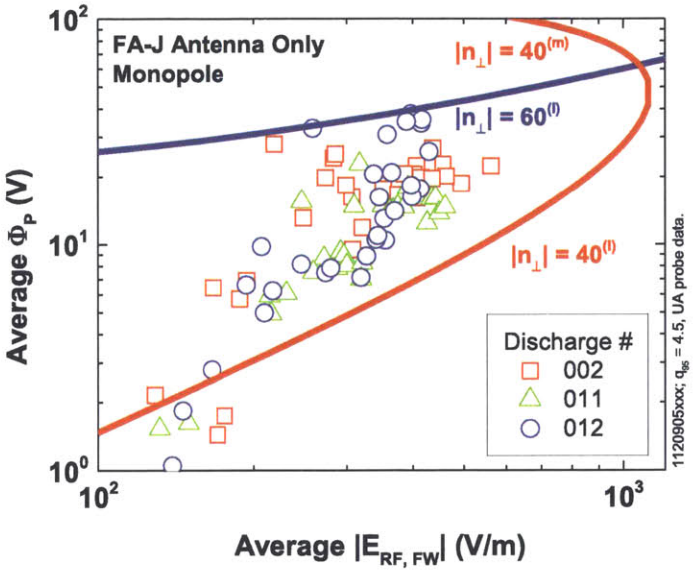

Figure 6-6: Average ICRF-enhanced plasma potential values as a function of the average $|E_{RF,\ FW}|$ for discharges under constant plasma conditions. The trends are shown for several reproducible discharges with constant plasma parameters. The solid lines are a theoretically expected trend from [80]. Active FA-J antenna only (monopole). UA probe data. The probes are blocked to the active antenna.

6.1.3 Correlation of plasma potential with local plasma density

The effect of the local plasma density on the plasma potential enhancement at the blocked location is opposite to the trend expected from the SW theory (e.g. Figure 5-5): the plasma potential decreases as the local plasma density is increased (Figure 6-7). The local plasma density at the S^3 probe was varied in Figure 6-7 by either changing the radial position of the probe ($\Delta_{probe} \equiv R_{probe} - R_{main\ limiter}$, $R_{main\ limiter} = 0.910\ m$, all radial distances are mapped to the midplane) or by changing the core plasma density ($n_{e\ core}$), which is known to strongly affect the SOL plasma density $n_{SOL} \sim n_{e\ core}^{2-3}$. Based on theory, the density dependence of the FW-rectified plasma potential is strongly influenced by the formation of the "sheath plasma wave (SPW) resonance" associated with the slow wave [79]. The SPW causes the rapid transition between the lowest and the highest roots in the theory curves of Figure 6-5 (a) and a similar transition happens when plotted against the local plasma density in Figure 4-13 (for the case of $n_\perp = 30$). However, the SPW resonance is expected to form at $n_e \sim 10^{18}\ m^{-3}$ for the experimental conditions found at the limiter surface on Alcator C-Mod. Therefore, even though the trend observed in Figure 6-7 is qualitatively consistent with the highest root of the theoretical solution (Φ_P decreasing with n_e), the experimental trend is expected to lie on the lowest root of the theoretical solution (Φ_P increasing with n_e). A strong upshift in the $|n_\perp|$ to values of ~ 100 or higher could explain the observed discrepancy, however, such a mechanism requires further study with a more extensive model of the ICRF wave-core plasma interaction. Also note that for each data set the RF power from the blocked E antenna was ramped from 0.5 to 1.5 MW and the local plasma would respond by decreasing its density. Such behavior is possibly consistent with the $\mathbf{E} \times \mathbf{B}$ drifts, such that the radial gradients of the plasma potential begin to influence the local plasma density profile [72]. However, our 1D FW model does not address the effect of the spatial profiles [78, 79, 80].

Also note that just as was the case in Chapter 5, Section 5.1, the local plasma

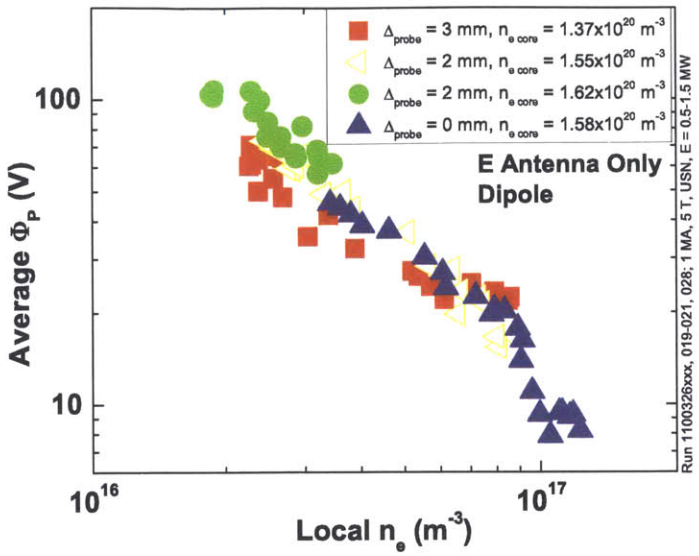

Figure 6-7: Plasma potential enhancement as a function of the local plasma density for the blocked group of field lines. Active E antenna only (dipole), $P_{RF} = 0.5 - 1.5\ MW$. $\Delta_{probe} \equiv R_{probe} - R_{main\ limiter}$, $R_{main\ limiter} = 0.910\ m$, all radial distances are mapped to the midplane. S^3 probe data. The probes are blocked to the active antenna.

density would change by the presence of ICRF power, however, for the case of the blocked active ICRF antenna, the local plasma density would increase, not decrease, in the presence of ICRF power. This experimentally observed effect is shown in Figure 6-8.

Figure 6-8 shows that the plasma potential peaks radially near the plasma facing side of the limiter ($\Delta_{probe} \sim 0\ mm$), which at first appears inconsistent with the plasma density trend in Figure 6-7. However, the trends in Figure 6-7 were obtained with the probe position changing by only 2-3 mm, implying that the FW evanescence over such a short distance may be ignored and the FW E-field amplitude may be assumed to remain constant. The same assumption may not be applied to the data in Figure 6-8 as the probe position changes by several cm and the evanescent decay of the FW E-field amplitude needs to be accounted. The effect of the FW E-field evanescence on the plasma potential will be discussed in more detail in the following subsection.

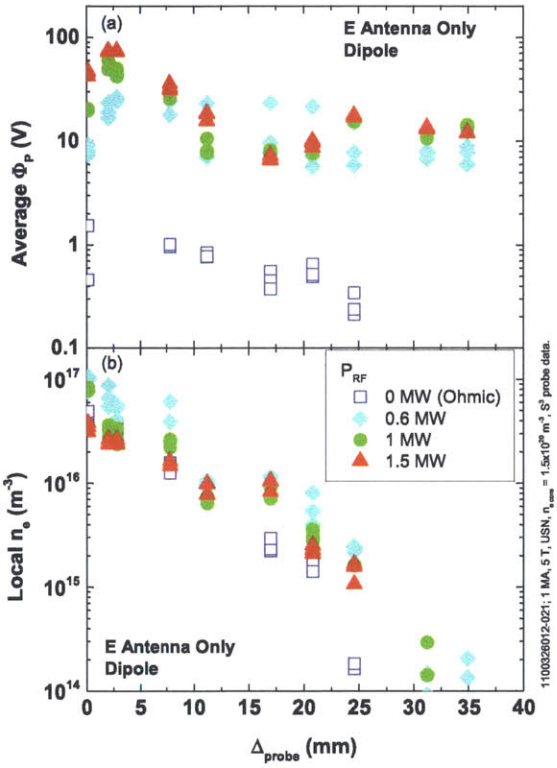

Figure 6-8: (a) radial plasma potential and (b) plasma density profiles in the shadow of the limiter far from an active ICRF antenna. $\Delta_{probe} \equiv R_{probe} - R_{main\ limiter}$, $R_{main\ limiter} = 0.910\ m$, all radial distances are mapped to the midplane. The trends are shown for various levels of ICRF power. Active E antenna only (dipole). S^3 probe data. The probes are blocked to the active antenna.

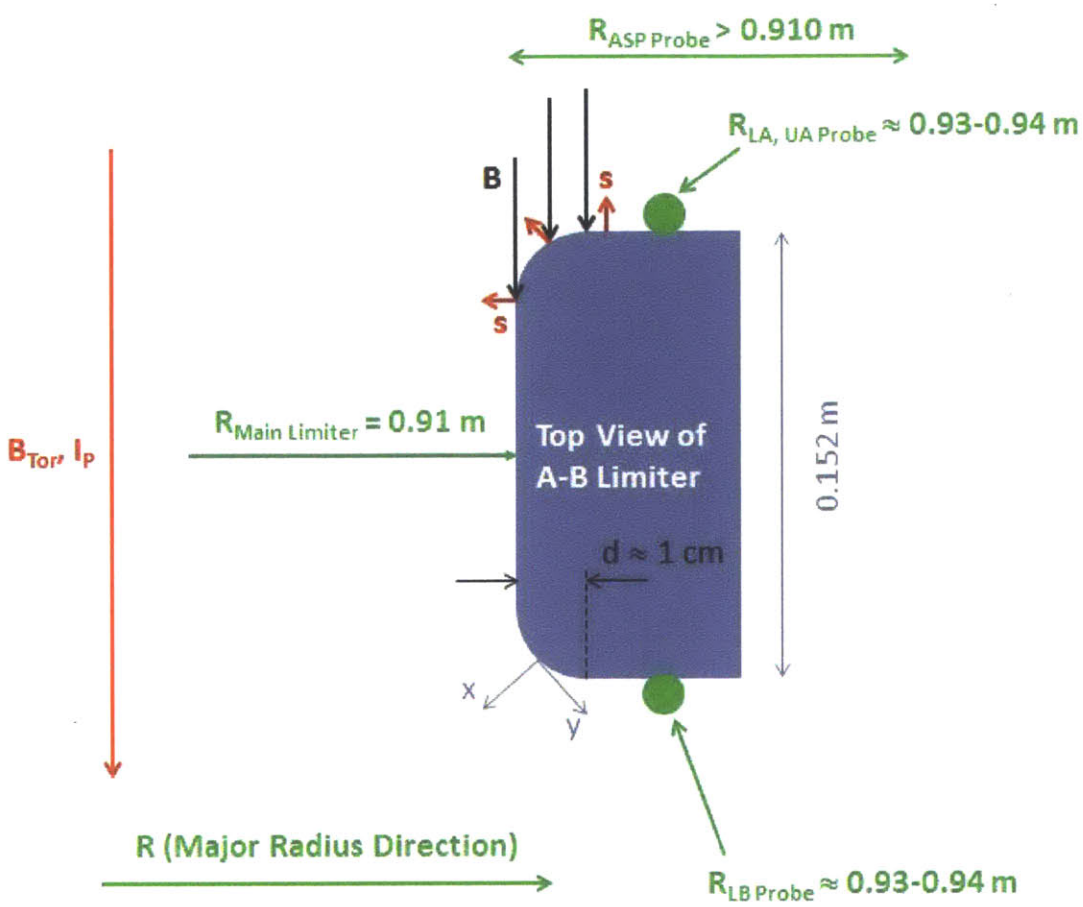

Figure 6-9: A top cross sectional view of the main limiter on Alcator C-Mod.

6.1.4 Correlation of plasma potential with local boundary geometry

Another experimentally observed feature, which is characteristic of the fast-to-slow wave coupling and then rectification, is the appearance of strong gradients in the enhanced plasma potential profile on field lines that intercept surfaces with a rapidly changing geometry, such as the limiter tip (Figure 6-9). The limiter tip is defined as the region where the surface normal $\mathbf{s}$ changes its direction with respect to the magnetic field B. For the case of Alcator C-Mod the limiter tip is characterized by the radial distance $d \approx 1\ cm$ with a constant radius of curvature.

Large gradients in the radial plasma potential profile and the resulting radial

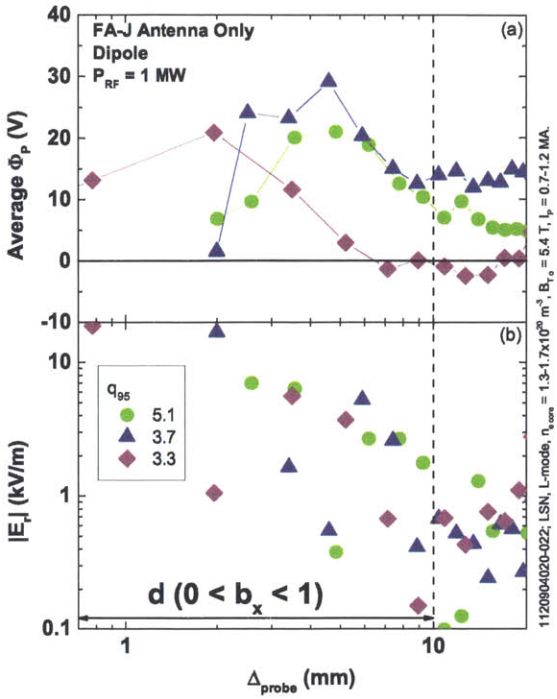

Figure 6-10: Radial profiles of (a) the plasma potential and (b) the resulting electric field profiles in ICRF-heated discharges. $\Delta_{probe} \equiv R_{probe} - R_{main\ limiter}$, $R_{main\ limiter} = 0.910\ m$, all radial distances are mapped to the midplane. The trends are shown for various edge safety factors q_{95}. Active FA-J antenna only (dipole). $P_{RF} = 1\ MW$. ASP probe data. Each point is data averaged over 1 ms. The probe is blocked to the active antenna.

electric fields ($E_r = -\nabla_r \Phi_P$) in the vicinity of the limiter tip are shown in Figure 6-10. The profiles are shown for discharges heated with the FA-J antenna at $P_{RF} = 1.0\ MW$. The profiles are shown for three different edge safety factor (q_{95}) values, 3.3, 3.7, and 5.1. The q_{95} scan was achieved by changing the plasma current, $I_P = 1.2$, 1.0, and 0.7 MA, while keeping the toroidal field (and, hence, the ICRF resonance location) constant at $B_{To} = 5.4$ T. The purpose of the q_{95} scan was to map out different poloidal locations along the limiter surface.

Re-plotting the data shown in Figure 6-10 as a function of the surface misalignment between the surface normal and the magnetic field lines reveals (Figure 6-11) that the misaligned surfaces are consistent with changing b_x, where $b_x \equiv \frac{B_x}{B}$ is the magnetic field component locally normal to the surface. Refer to Figure 6-9 for the definition

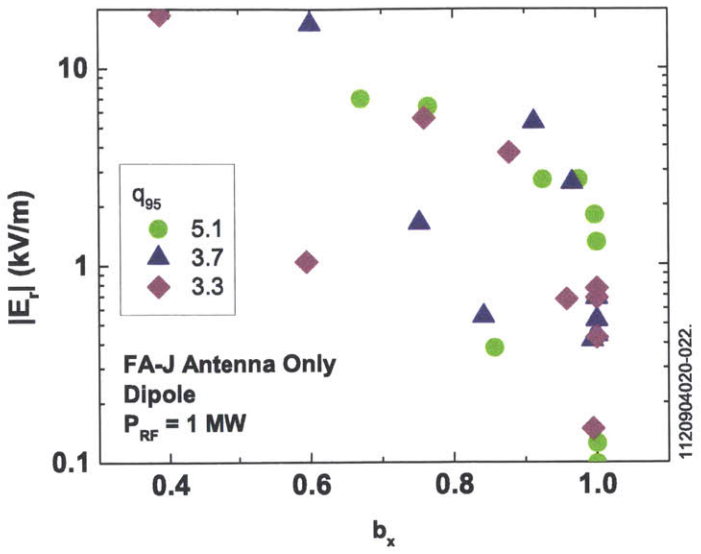

Figure 6-11: Radial gradients in the ICRF-enhanced plasma potentials (E_r) as a function of surface to field line misalignment. b_x is the magnetic field component that is locally normal to the surface. Data as organized in Figure 6-10.

of the local X-direction. The results are independent of the poloidal location along the limiter surface varied with the q_{95} scan. Note that the largest radial gradients in the plasma potential are associated with the limiter tip region, as expected from the fast wave rectification theory [80].

The region outside the limiter tip ($R_{mid} > 0.92\ m$ or $\Delta_{probe} > 10\ mm$) is characterized by a constant geometry condition, $b_x \approx 1$, therefore, we expect to see a slowly varying plasma potential profile across that region as other effects, such as the evanescence of the fast wave electric field strength begin to dominate. This is confirmed by Figure 6-10 (b) that shows $|E_r|$ is typically $\lesssim 1kV/m$ in this region. In addition, a radial ICRF-enhanced plasma potential profile taken in a high-power ($P_{RF} = 4$ MW) L-mode discharge is shown in Figure 6-12. In addition to the steep gradient of the plasma potential across the limiter tip, there is also a much more gradual decay of ICRF-enhanced Φ_P across the majority of the limiter surface characterized by $b_x \approx 1$. The decay of the plasma potential is well approximated by an exponential curve with the e-folding length λ_{Φ_P} of 3.5 cm. This decay rate is too gradual to correlate with the plasma density decay in the shadow of the limiter – the density decays radially with

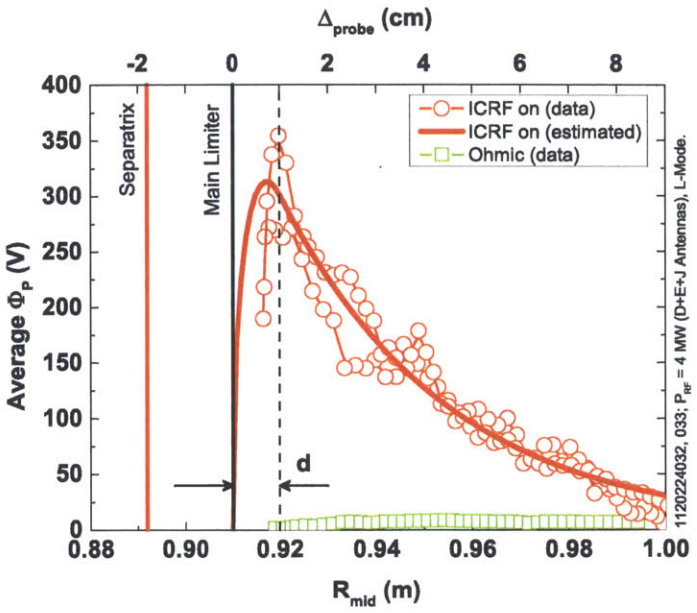

Figure 6-12: A radial plasma potential profile across the entire radial dimension of the main limiter. Active D, E, and FA-J antennas. Solid line is an estimated profile based on Equation 6.1. $P_{RF} = 4\ MW$. ASP probe data. The probe is blocked to the FA-J antenna and unmapped to the D and E antennas.

an e-folding length λ_{n_e} of several mm, not cm. It is also unlikely that the electron temperature profile is responsible for the observed radial plasma potential profile in the shadow of the limiter – the electron temperature is approximately constant across the entire profile, $T_e = 10 - 20\ eV$. Figure 6-13 shows the radial plasma density and electron temperature profiles in the vicinity of the main limiter in an Ohmic L-mode discharge on Alcator C-Mod.

It appears that the radial Φ_P profile is consistent with the fast ICRF waves incident from the main plasma direction (R>0.91 m) and evanescently decaying in the +R radial direction. It is possible to estimate the expected evanescent length of the fast ICRF waves from the cold plasma dispersion relation for fast ICRF waves propagating in a vacuum-like region: $n_\perp^2 + n_{//}^2 = 1$ (Chapter 4, Section 4.4). Assuming that the parallel index of refraction is that of the launched fast waves ($n_{//} \sim 10$) implies that at 80 MHz we have $|k_\perp| \sim 20\ m^{-1}$ and the e-folding length $\frac{1}{|k_\perp|} \sim 5\ cm$. Both λ_{Φ_P} and $\frac{1}{|k_\perp|}$ are of comparable size. Note that for a large $n_{//}$ ($\gg 1$) the perpendicular

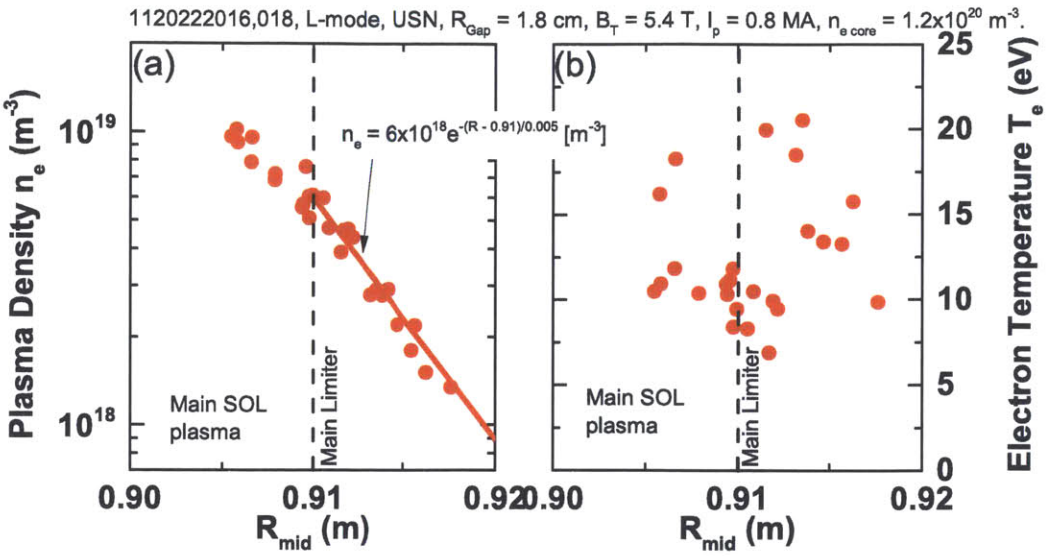

Figure 6-13: Radial profiles of (a) the local plasma density and (b) the local electron temperature profiles in the vicinity of the main limiter in an Ohmic L-mode discharge on Alcator C-Mod. Solid line is an exponential fit to the plasma density with a e-folding length of 5 mm. ASP probe data.

index of refraction may be approximated as $|n_\perp| \approx n_{//}$ and the perpendicular fast wave transmission factor exponentially decreases with increasing $n_{//}$.

Figure 6-12 also shows a heuristic estimate of the plasma potential profile of the form:

$$\Phi_P = 400 b_x e^{-\frac{\Delta_{probe}}{0.035\ [m]}}\ [V], \tag{6.1}$$

where we account both for the limiter curvature and the evanescence of the fast wave. Equation 6.1 assumes that the rectified plasma potential is proportional to the amplitude of the slow wave E-field that is generated/coupled by a fast wave reflecting at a conducting surface. The amplitude of the coupled slow wave E-field is given by Equation 4.31. Equation 4.31 is applicable to a vacuum-like fast wave coupling to an electrostatic slow wave in a low density plasma region, similar to the experimental conditions in Figure 6-12.

6.1.5 Correlation of plasma potential with launched fast wave spectrum

The J antenna (both toroidally and field-aligned configurations) on Alcator C-Mod is capable of actively modifying the launched ICRF wave spectrum by changing the phase between the RF currents that flow along individual antenna straps. For example, the standard phase between the strap currents is dipole (0, π, 0, π), but the antenna is also capable of running in monopole phasing (0, 0, 0, 0). The dipole RF current phasing is expected to launch ICRF waves with the parallel index of refraction $n_{//} \sim 13$, while the monopole configuration is expected to launch waves with $n_{//} \sim 0$. The parallel direction is with respect to the background magnetic field. Experimentally, it is observed that discharges with the ICRF antenna operated in monopole phasing show no core plasma heating as a result of little to no fast wave coupling to the core plasma [87]. Such poor ICRF wave coupling is consistent with a strong upshift of the launched ICRF wave spectrum from the expected value of $n_{//} \sim 0$ to $n_{//} \sim 26$ [85]. A proposed mechanism capable of upshifting the launched ICRF wave spectrum accounts for strong RF image currents flowing along (conducting) antenna septa that separate individual current straps. For the case of dipole phasing, the net image currents along the septa are ~ 0; however, for the case of monopole phasing, the net image currents are no longer zero and begin to actively modify the launched $n_{//}$ spectrum. Figure 6-14 provides a simple diagram that demonstrates the above-described mechanism of spectrum upshifting.

Experimentally, an increase is observed in the ICRF-enhanced plasma potentials in discharges "heated" with monopole phasing, compared to discharges heated with the ICRF antenna operated in dipole phasing (Figure 6-15). These higher plasma potentials occur despite the lower, in general, FW E-fields in monopole phasing (Figure 6-16). Switching from the dipole to the monopole case, it appears that the plasma potential increase anti-correlates with the change in the RF wave E-field amplitude. Yet, the observed Φ_P vs. $\dot{B}$ correlation remains consistent with the fast wave rectification mechanism for the following reasons. 1) Experimentally it is observed that for

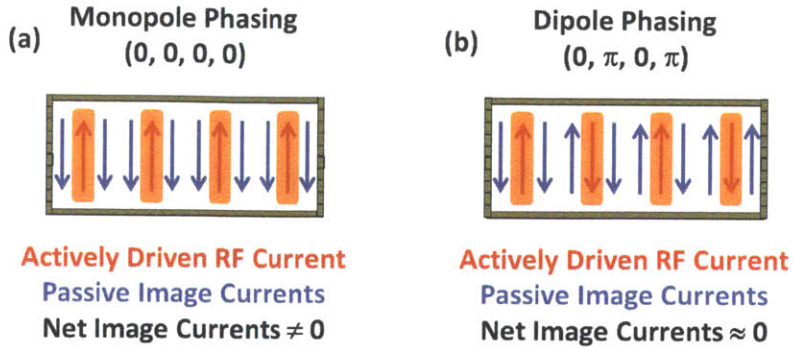

Figure 6-14: Actively driven and image RF currents inside an ICRF antenna box for the case of (a) monopole and (b) dipole phasing. The RF current straps are separated by conducting antenna septa that provide a path for image currents.

given fixed ICRF antenna phasing Φ_P still correlates with the local fast wave E-field amplitude (Figure 6-15 (b)). 2) The drop in the fast wave E-field amplitude (Figure 6-16), as ICRF antenna phasing switches from dipole to monopole, is consistent with the cold plasma FW propagation with a strongly upshifted $n_{//}$. The cold plasma dispersion relation ($|k_\perp|$ vs. n_e) for $n_{//} = 13$ (dipole phasing) and for $n_{//} = 26$ (monopole phasing) reveals that the evanescence of the fast wave is stronger for the upshifted case of $n_{//} = 26$ (Figure 6-17). 3) The general increase in the plasma potential with the upshift in the index of refraction for a given FW E-field amplitude is also consistent with the fast wave rectification mechanism (Figure 6-6) [79]. The strong Φ_P increase is due to the transition to the higher-value root of the Φ_P vs. $|n_\perp|$ solution [79]. Thus, it can be concluded that the Φ_P dependence on the ICRF wave spectrum/phasing in regions blocked to the active antenna is broadly consistent with the FW rectification mechanism.

A multitude of experimental observations showed that potential enhancements in blocked and unmapped SOL regions are often the result of FW fields incident into the SOL boundary plasma due to incomplete absorption in the core plasma. The key features of the fast wave rectification theory [79] are 1) unabsorbed fast waves enter the plasma region in the limiter shadow from the main plasma; 2) the fast waves are evanescent in the low density plasma regions, as dictated by the cold plasma dispersion; 3) the strength of the resulting FW rectification is determined by the

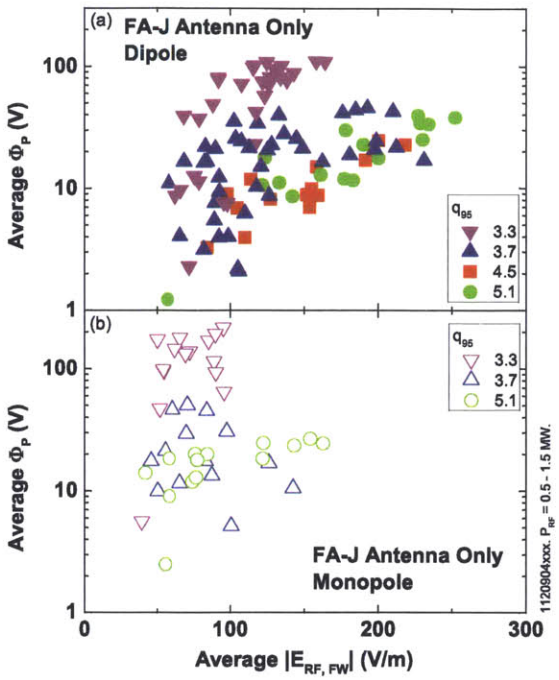

Figure 6-15: Plasma potential enhancement in discharges heated with the FA-J antenna in (a) dipole and (b) monopole phasing as a function of the local FW electric field strength. $P_{RF} = 0.5 - 1.5\ MW$. UA probe data. The probes are blocked to the active antenna.

strength of the fast wave electric field, the geometry of the limiter boundary, and the spectrum of the fast waves. However, under certain conditions, the plasma potential enhancement displays features that are on one hand consistent with the local FW E-field amplitude yet on the other hand are unexpected from the above-mentioned fast wave rectification model. These experimental results are the subject of the following section.

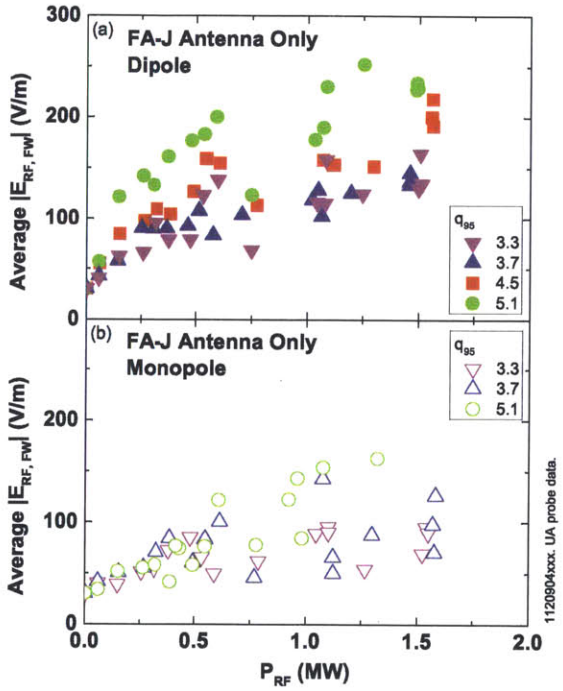

Figure 6-16: Local FW electric field strength as a function of the launched ICRF power with the FA-J antenna operated in (a) dipole and (b) monopole phasing. Data as organized in Figure 6-15. UA probe data. The probes are blocked to the active antenna.

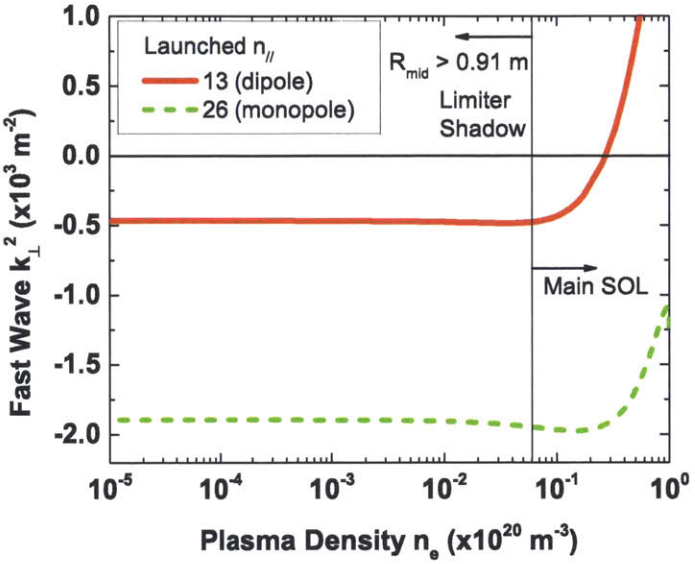

Figure 6-17: A cold plasma dispersion relation for a fast ICRF wave for the cases of dipole (launched $n_{//} = 13$) and monopole (launched $n_{//} = 26$) wave spectrum. Launched $f = 80\ MHz$.

6.2 ICRF enhancement of plasma potentials in far SOL regions between passive limiters

While the 1D FW rectification model outlined in the previous section appears to be an important cause of enhanced potentials, in certain cases in the far SOL regions of the plasma neither this model, nor SW rectification, can account for the presence of ICRF-enhanced plasma potentials. This result is illustrated in Figure 6-18, which shows that for certain values of the edge safety factor (q_{95}) a large peak in the ICRF-enhanced plasma potential, measured by the ASP, develops far in the shadow of the main limiter. The q_{95} scans were performed to determine the plasma potential dependence on the poloidal field mapping along limiter surfaces (in the Z-direction). The far SOL potential feature is observed on both the ASP and UA probes when the FA-J antenna is powered. Correlating the UA and ASP data at the same local radial locations of the ASP probe (Figure 6-19) reveals that the formation of the far SOL plasma potential structure appears to depend only on q_{95} and is not observed at the same mapped location on the K limiter surface for different q_{95} values (i.e. the q_{95} scan does not simply "sweep" the potential structure by the two different probes). The far SOL potential structure appears at the same radial location in all cases but shows a stronger potential enhancement when the FA-J antenna is operated in monopole phasing. This result is qualitatively consistent with a higher level of unabsorbed ICRF power in the SOL for a given level of launched ICRF power in monopole phasing (based on core plasma response). The effect of the launched ICRF wave spectrum on the plasma potential enhancement was discussed in the previous section. However, the plasma potential still scales with the local fast wave electric field as shown in Figure 6-20. It seems that the 1D FW rectification mechanism [79] may be a possible cause of the potential increase. Yet, further examination will indicate that this mechanism is an incorrect or, at best, an incomplete explanation.

Note that this far SOL Φ_P enhancement occurs on a blocked group of field lines that are bounded toroidally by two passive limiter surfaces (K and A-B limiters) and do not directly map to an active ICRF antenna structure. As a result, we can

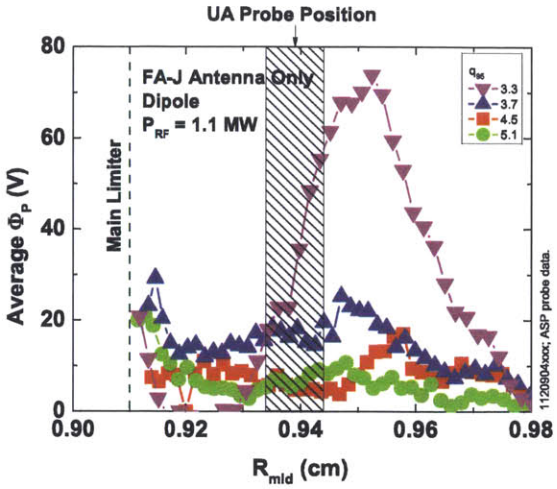

Figure 6-18: A radial profile of the ICRF-enhanced plasma potential in the shadow of the limiter at various q_{95} values. The results are mapped to the A side of the K limiter, see Figure 5-2. Active FA-J antenna only (dipole). $P_{RF} = 1.1$ MW. ASP probe data. The probes are blocked to the active antenna.

rule out RF-driven limiter currents as the mechanism responsible for the observed far SOL plasma potential structure, as this mechanism requires a direct magnetic field connection to the active ICRF antenna structure [31, 88]. It is also unlikely that the observed plasma potential structure is a result of an excited RF cavity mode, where the cavity boundary is defined by the spatial dimensions of the limiter sides ($\sim$0.1 $\times$ 0.1 m) and the length of the field line ($\sim$1 m). The cutoff frequency to excite modes in such a cavity would be $> 1\ GHz$, which is far greater than the operating frequency of the ICRF antenna (78 MHz). It is also safe to eliminate the reflected fast wave fields as a source of the far SOL plasma potential enhancement: the fast wave is evanescent in the low density plasma region of the far SOL on Alcator C-Mod. The evanescence of the fast wave determines the shape of the radial profiles of the fast wave field strength and the resulting FW-rectified plasma potential is that of a decaying exponential curve that peaks at its source. Our standard 1D FW rectification mechanism assumes that the fast wave source is in the form of unabsorbed scattered fast waves that are incident from the direction of the plasma core ($R_{mid} < 0.91\ m$, travelling in the $+R$ direction). However, the shape of the far SOL plasma potential

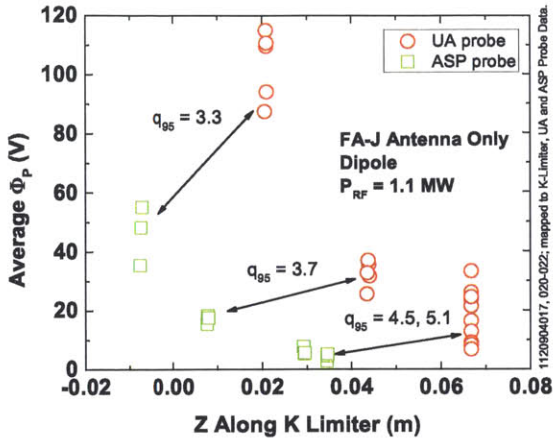

Figure 6-19: A poloidal profile of the ICRF-enhanced plasma potential in the shadow of the limiter at various q_{95} values. The results are mapped to the A side of the K limiter, see Figure 5-2. Active FA-J antenna only (dipole). $P_{RF} = 1.1$ MW. ASP and UA probes data. The probes are blocked to the active antenna.

feature is consistent with a fast wave source that is excited locally in the shadow of the limiter ($R_{mid} > 0.91\ m$) at $R_{mid} \approx 0.95\ m$. Therefore, while the Φ_P enhancement follows the FW E-field amplitude, the source of the FW E-field can seemingly not be the reflection of fast wave unabsorbed from the core because these wave fields could not peak in amplitude so far into the limiter shadow.

Surprisingly, the far SOL Φ_P rise is *not* observed on the LA probes, see Figure 6-21, even though the LA station is located approximately the same toroidal distance from the active FA-J antenna as the UA probe (Figure 5-2). However, the LA probe station resides below the midplane. As a result, this location is not blocked but rather completely unmapped to the active FA-J antenna. Note that for the case of the active FA-J antenna, only the ASP and UA probes sample blocked field lines and only these probes observe the far SOL plasma potential enhancement. The geometry of the bounding surfaces is also different for the case of the magnetic field lines that are intercepted by the LA probes: the field lines are now bounded by the vertical limiter side plate and the horizontal lower divertor shelf. These observations together suggest that the limiting surfaces and their mapping to the active antennas play an important role in ICRF enhancement of the plasma potential.

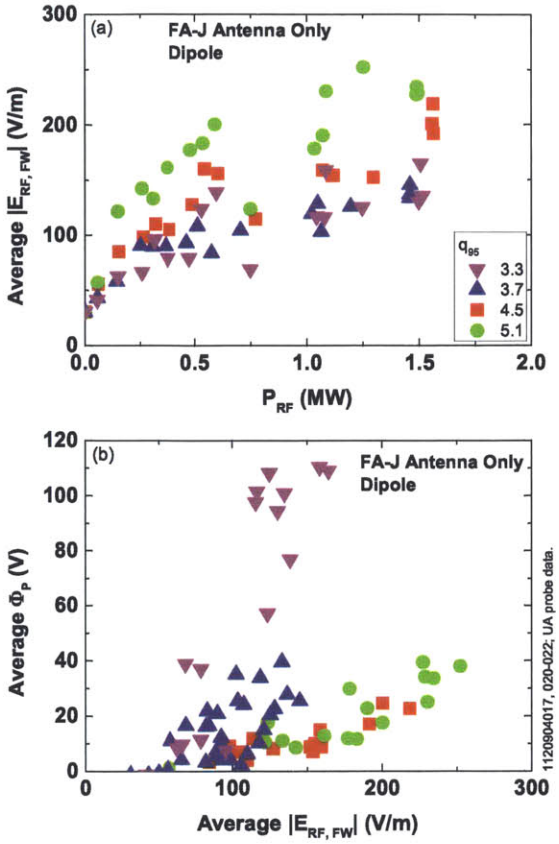

Figure 6-20: (a) The average fast electric field strength as a function of the launched ICRF power and (b) the average ICRF-enhanced plasma potential as a function of the fast wave electric field strength. The far SOL plasma potential structure forms for $q_{95} = 3.3$ (Figures 6-18 and 6-19). Active FA-J antenna only (dipole). UA probe data. The probes are blocked to the active antenna.

The far SOL Φ_P rise is also *not* observed on the S^3 probes, see Figure 6-21. The S^3 probes sample magnetic field lines in the close vicinity of the field lines sampled by the LA probes, yet the S^3 diagnostic is located much closer toroidally to the active FA-J antenna. This result also supports our previous statement that the far SOL plasma potential enhancement only affects field lines that are blocked to the active ICRF antenna.

The far SOL feature is *not* observed on any of the four probe stations (ASP, UA, LA, S^3) when the plasma discharge is heated with the E antenna (Figure 6-22). Note that for the case of the E antenna no magnetic field lines sampled by the four

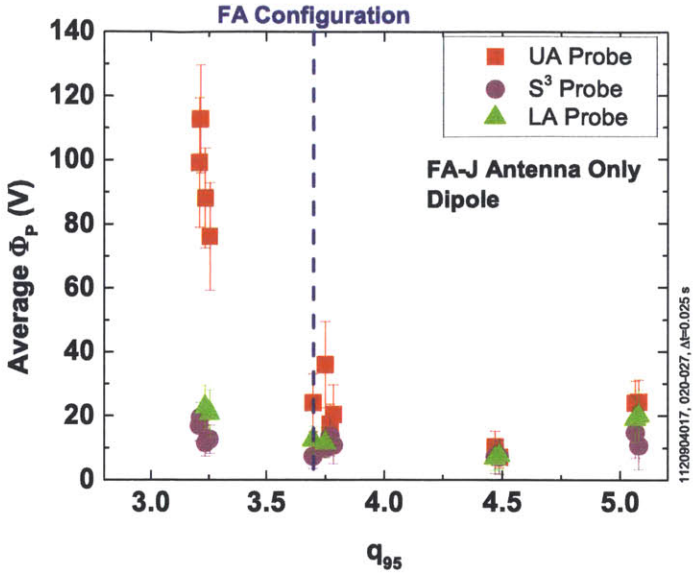

Figure 6-21: Average ICRF-enhanced plasma potential values as a function of q_{95}. UA, S^3, and LA probe data. Active FA-J antenna only (dipole). $P_{RF} = 1.1\ MW$. FA refers to the field-aligned q_{95} value of the FA-J antenna. The S^3 probe was positioned at $R_{mid} = 0.925\ m$ or $\Delta_{probe} = 15\ mm$. The UA probe is blocked to the active antenna. The S^3 and LA probes are unmapped to the active antenna.

probes directly map to the active antenna structure: the UA and ASP probes are unmapped and the S^3 and LA probes are (marginally) blocked to the active antenna. This result once again supports our observation that only field lines that are blocked to the active antenna, but do not directly map to the antenna, experience the far SOL plasma potential enhancement.

This far SOL region that is toroidally bounded by two passive limiter surfaces is not accessible to RF-driven currents excited by the active antenna, nor is the radial plasma potential profile consistent with the FW rectification where the fast waves enter the far SOL region from the main plasma direction. However, it would be possible to make the far SOL plasma potential feature consistent with the FW rectification mechanism, but under a condition that the fast wave is excited far in the shadow of the passive limiters at $R_{mid} \approx 0.95\ m$. In this case the radial shape of the plasma potential peak would be determined by the fast waves that evanesce in the $+R$ and $-R$ directions radially away from the source with a typical e-folding length

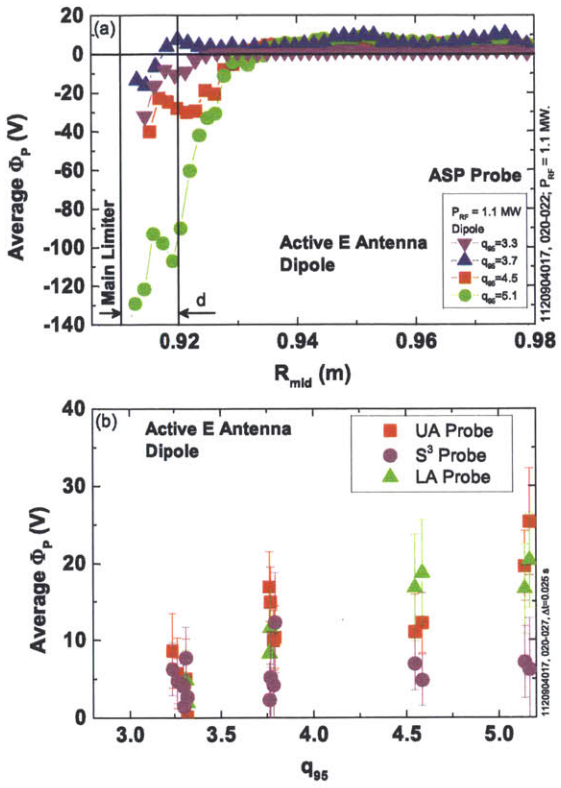

Figure 6-22: (a) Radial plasma potential profiles at various q_{95} values, ASP probe data. (b) ICRF-enhanced plasma potentials as a function of q_{95}, UA, LA, and S^3 probe data. Active E antenna only (dipole). $P_{RF} = 1.1\ MW$. The S^3 probe was positioned at $R_{mid} = 0.925\ m$ or $\Delta_{probe} = 15\ mm$. The UA and ASP probes are unmapped to the E antenna. The LA and S^3 probes are blocked to the E antenna.

1-2 cm. Note that the radial position of the plasma potential peak matches the radial location of the ICRF antenna current strap located at $R_{mid} = 0.94\ m$. However, direct field line mapping between the ASP and UA probes and the active FA-J antenna is not possible since they are blocked by the K limiter in all cases. Therefore, it is not clear what mechanism is capable of exciting fast waves at this toroidal location. However the data suggests that perhaps the passive structures are "activated" by the RF power and are acting as proxy antennas, i.e there are finite RF currents being excited in the structures that could generate the RF fields measured in the far-SOL. The exact mechanism by which this could occur may be related to unexpected current return paths in the vessel and/or inductive excitation of the passive structures. This

could be the subject of further investigations.

Chapter 7

Implications of ICRF-enhanced plasma potentials on plasma-material interactions

In the previous section we saw that the plasma potential on open magnetic field lines in the SOL becomes significantly enhanced in ICRF-heated discharges on Alcator C-Mod. In this section we are going to briefly explore what possible implications this ICRF enhancement of the plasma potential has on plasma-wall interactions in a tokamak. In particular, we are interested to know what happens to sputtering and erosion of PFCs as the plasma potential is significantly changed by the presence of ICRF power. Note that sputtering and erosion of PFCs on Alcator C-Mod were extensively studied previously by Pappas [20] and one of the key conclusions of that study was that erosion of the PFCs is significantly enhanced in ICRF-heated discharges on Alcator C-Mod. *Is the enhancement of the plasma potential in ICRF-heated discharges the leading cause that is responsible for the observed enhancement in sputtering and erosion of the plasma facing components?*

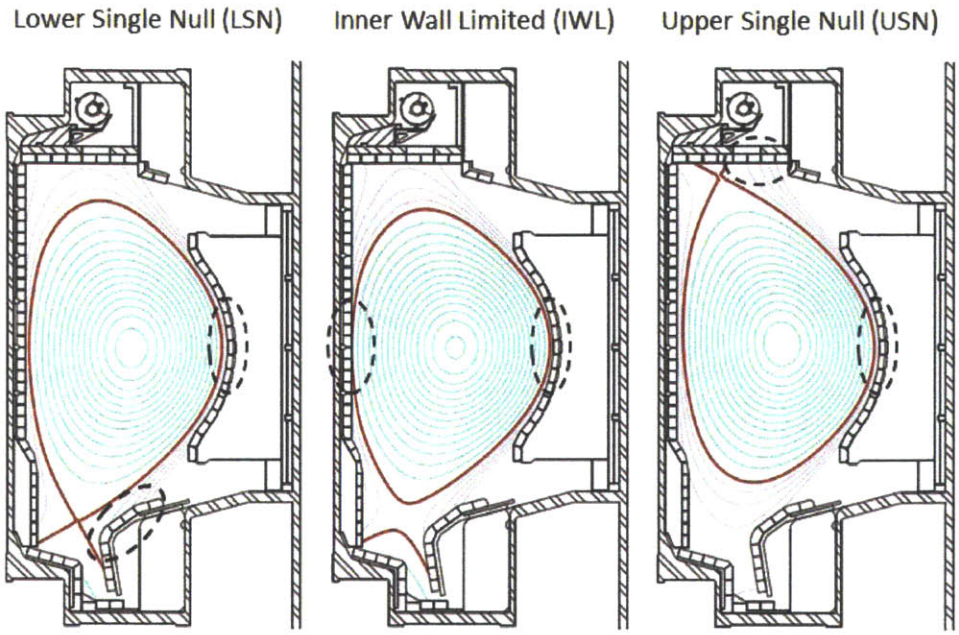

Figure 7-1: Typical plasma shapes generated in Alcator C-Mod. The dashed lines show regions of the most intense plasma-material interactions (PMIs).

7.1 Brief overview of possible erosion mechanisms in tokamaks

Erosion of PFCs in tokamaks is a key PMI that ultimately determines the life-time of in-vessel components. Depending on the operating regime, the components subjected to the most intense PMIs are the divertor and the inboard and outboard limiters, see Figure 7-1.

Possible erosion mechanisms in tokamaks are physical [18] and chemical [18] sputtering, melting/evaporation/sublimation [18], arcing [18] and fuzz growth [89]. Melting, sublimation and arching are typically transient off-normal events that are capable of injecting significant quantities of eroded materials into the plasma, large enough to cause disruptions [18]. Fuzz growth is only relevant to plasmas with a non-zero helium impurity fraction and to tokamaks with refractory PFCs (either molybdenum or tungsten) [89]. Sputtering, physical and chemical, is a steady state process that dominates erosion of PFCs during the majority of the discharge duration in a typical

tokamak plasma. Chemical sputtering is significant in tokamaks with low-Z PFCs, such as C [18]. Alcator C-Mod is a high-Z (Mo) tokamak and, as a result, physical sputtering by ions is by far the dominant erosion mechanism in this device.

7.2 Physical ion sputtering in presence of ICRF-enhanced plasma potentials

Modeling of ion sputtering is an actively researched area on several tokamaks, such as DIII-D [90], ASDEX [91], NSTX [92] and Alcator C-Mod [20, 22, 25]. The gross erosion flux, or influx, caused by incident plasma species f ($\Gamma_{o,f}$) is determined by the product of the incident plasma flux of that species striking the PFCs ($\Gamma_{i,f}$) and the ion sputtering yield of the material surface by that ion species (Y_f): $\Gamma_{o,f} = \Gamma_{i,f} Y_f$. The incident flux due to the main deuterium ions (Γ_i) is directly proportional to the local plasma density according to Equation 7.1 [32]:

$$\Gamma_i \approx 0.5 n_e c_s, \tag{7.1}$$

where the sound speed c_s is estimated according to: $c_s = 1 \times 10^4 \sqrt{\frac{T_e}{m_i}}$ $[m/s]$ [34]. Equation 7.1 assumes that the magnetic field line is normal to the surface, which is a good approximation of the angle between magnetic field lines and the toroidal sides of the limiters on Alcator C-Mod.

The total gross erosion due to several ion species is equal to the sum over all the species present in the plasma. For example, a typical Alcator C-Mod deuterium plasma striking the Mo divertor plates is composed primarily of ~99% D^+ ions and ~1% B^{3+} ions with trace amounts of other impurities, such as other boron ionization states, Mo, Fe, H, O, Ni, W, C, Ti, etc. [20]. Note that the species with the highest presence in the plasma, such as D^+ in deuterium discharges, is not necessarily the species that dominates sputtering of PFCs in tokamaks due to the non-linear dependence of the sputtering yield on the incident species mass [18].

Previous [23, 29] and current [35, 53] probe studies of ICRF-heated discharges on

Alcator C-Mod show that the plasma potential and, hence, the third term in Equation 1.15 ($E_{sheath} = Z_i|V_{sheath}|$) is strongly affected (enhanced) by ICRF power. The potential drop across the sheath is no longer thermal, i.e. $|eV_{sheath}| \neq 3T_e$, but is a non-linear combination of multiple local parameters, such as n_e, T_e, field line orientation and RF wave intensity and spectrum. The precise physics that determines the sheath voltage drop depends primarily on the nature of the sheath voltage enhancement, fast wave vs. slow wave rectification [76, 77, 78, 79, 80]. Note that previous and current emissive probe studies show that the enhanced potentials in the SOL of ICRF-heated plasmas on Alcator C-Mod often reach values $> 100\ V$ [23, 29, 35, 53]. These high potentials are observed in locations that are mapped, unmapped, and blocked to active ICRF antennas.

So what are the implications of the plasma potential enhancement on the gross Mo influx estimate? Pappas' analysis using the thermal sheath voltage drop showed that gross Mo PFC erosion in D^+ discharges on Alcator C-Mod is dominated by B^{3+} ions, which typically represent only ~1% of the incident plasma flux, with the D^+ ions accounting for the remaining ~99% [20]. A combination of the high sputtering threshold energy of $E_{th,\ D^+} = 94\ eV$ and the low electron temperature in the vicinity of the PFCs in Alcator C-Mod, typically $< 50 - 60\ eV$ [14], results in a typically low fraction of the sputtered gross Mo influx due to the incident D^+ ion flux. Figure 7-2 shows the sputtering yield vs. the incident ion energy due to D^+ and B^{3+} ions.

As we mentioned in the previous paragraph, the electron temperature in the vicinity of the PFCs in Alcator C-Mod is typically $< 50 - 60\ eV$ reaching the values of $\sim 10\ eV$ in the vicinity of the main protection limiters. As a result, any sputtering/erosion model, which is based on the thermal sheath assumption, has a constraint on the maximum allowed incident ion energy. However, as we remove the thermal constraint on the voltage drop across the sheath, the gross erosion pattern begins to change considerably. This effect is demonstrated in Figure 7-3. We used realistic Alcator C-Mod parameters found in the vicinity of the main limiter PFCs: local $T_e = 10\ eV$, local $n_e = 6 \times 10^{18}\ m^{-3}$, boron ion fraction $f_{B^{3+}} = 0.01$, deuterium main ions, ions striking the surface normally. The boron ions are assumed to be frictionally

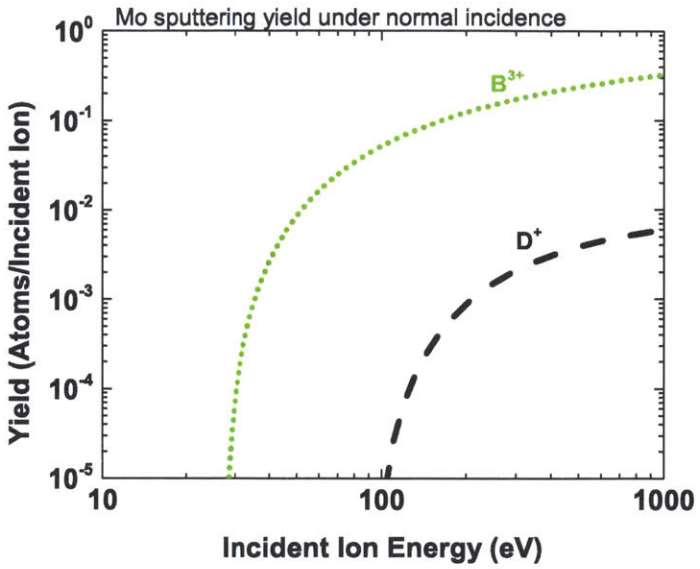

Figure 7-2: Estimated Mo sputtering yields due to normally incident D^+ and B^{3+} ions. The estimates are based on the empirical Bohdansky Equation 1.11 [17].

coupled to the main ion species and, hence, enter the plasma sheath at the deuterium ion sound speed [20].

Figure 7-3 shows that gross erosion of PFCs is dominated by boron impurities for the plasma sheath potential drops that are below 100 V. However, as the sheath potential drop is raised to several hundred volts, the gross erosion due to the main deuterium ions becomes comparable to the value due to the boron impurities. As the sheath potential drop is raised above $\sim 400\ V$ erosion due to the main deuterium ions becomes dominant. As it was shown in Chapters 5 and 6, the peak plasma potential values are typically $< 200\ V$ in discharges heated with a single ICRF antenna ($P_{RF} < 2\ MW$), but may reach values of $\sim 400\ V$ or more in high-power discharges heated with multiple ICRF antennas ($P_{RF} > 2\ MW$). The corresponding range of the expected Mo sputtering yield values for typical ($P_{RF} < 2\ MW$) and high-power ($P_{RF} > 2\ MW$) ICRF-heated discharges is shown in Figure 7-3.

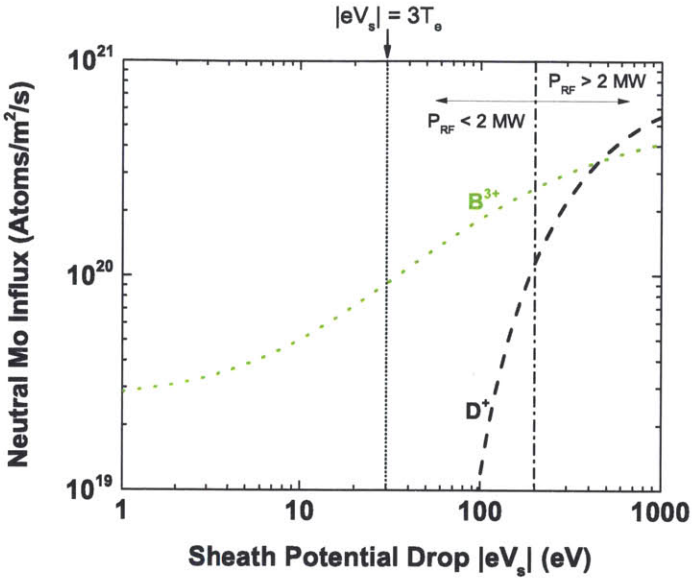

Figure 7-3: Mo sputtering yield due to ion sputtering by incident D^+ and B^{3+} ions as a function of the sheath potential drop. The total incident ion energy is estimated based on Equation 1.15. Typical Alcator C-Mod plasma parameters in the vicinity of the main limiter are assumed: $T_e = 10\ eV$, $f_{B3+} = 0.01$, $n_e = 6 \times 10^{18}\ m^{-3}$. The B^{3+} ions are assumed to be frictionally coupled to the main ion deuterium species. The peak plasma potential values are typically $< 200\ V$ in discharges heated with a single ICRF antenna ($P_{RF} < 2\ MW$).

7.3 Effect of plasma potential profile on incident ion flux

As we saw in the previous chapter, ICRF power has a dramatic effect on the plasma potential in the SOL region. The direct impact of the plasma potential enhancement on PMIs is to modify the sputtering yield of the plasma facing surface and it was discussed in Section 7.2. However, our radially scanning probes reveal that the plasma potential is not the only plasma parameter that becomes affected: the plasma density profile also begins to change in the presence of ICRF power. This effect is shown in Figures 7-4 (b) and 7-5 (b) for the mapped and blocked cases, respectively. The most prominent trend is the decrease in the plasma density across the entire radial profile for the mapped case (Figure 7-4 (b)). Note that the sparseness of the plasma density

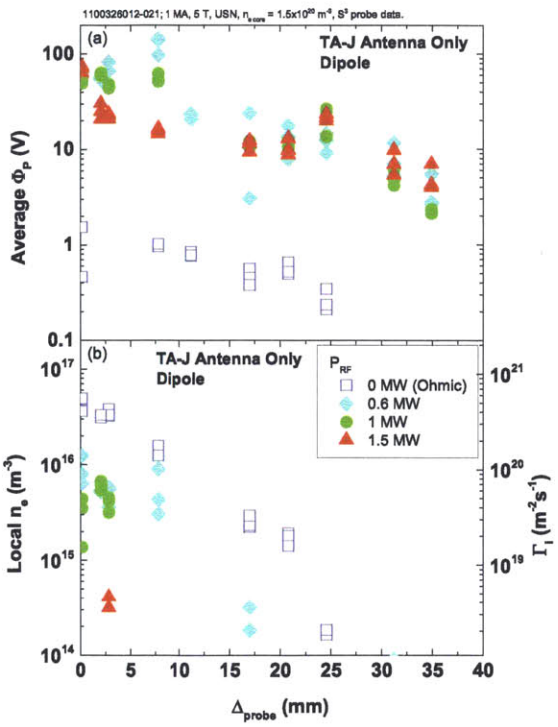

Figure 7-4: Radial profiles of (a) plasma potential and (b) plasma density in the shadow of the limiter. Γ_i is the incident deuterium ion flux estimated for $T_e = 10\ eV$ and normal incidence. The profiles are shown for various levels of ICRF power. Active TA-J antenna only (dipole). S^3 probe data. The probes are mapped to the active antenna.

data in Figure 7-4 (b) is due to the reduction of the local plasma density values below the detectable limit of the Langmuir probe ($n_e \lesssim 10^{14}\ m^{-3}$).

It is unlikely that the plasma density radial profile changes in the shadow of the limiter are a result of the core plasma density changes in response to injected ICRF power. While the line-averaged plasma density does change when ICRF antennas are turned on in both mapped and blocked cases, the line-averaged plasma density shows no dependence on the level of injected ICRF power, see Figure 7-6 (c). Yet the local plasma density shows a clear response to the level of launched ICRF power (Figure 7-6 (d)).

The effect of the RF power (both lower hybrid and ICRF) on the plasma density profile has been extensively studied on Alcator C-Mod with a reflectometer diagnostic

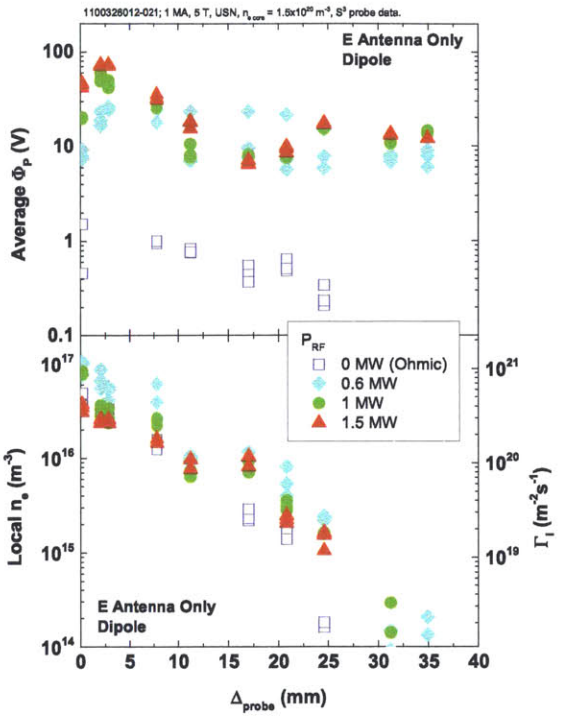

Figure 7-5: Radial profiles of (a) plasma potential and (b) plasma density in the shadow of the limiter. The profiles are shown for various levels of ICRF power. Active E antenna only (dipole). S^3 probe data. The probes are blocked to the active antenna.

[72, 96]. The key conclusion of these studies is: the radially varying plasma potential profile begins to influence the radial plasma density profile. The physical mechanism responsible for this modification is consistent with the $\mathbf{E} \times \mathbf{B}$-induced charged particle flow along equipotential surfaces.

How does the change in the plasma density affect the plasma material interactions? The incident main ion flux (Γ_i) is directly proportional to the local plasma density according to Equation 7.1, where we assume that the angle between the magnetic field line and the surface is normal. The radial profile of the incident ion flux is shown in Figures 7-4 (b) and 7-5 (b) for the mapped and blocked field lines. The electron temperature was taken as $T_e = 10\ eV$, which is typical for Alcator C-Mod SOL plasmas in the shadow of the limiter.

Using the plasma potential and the plasma density profiles shown in Figures 7-4

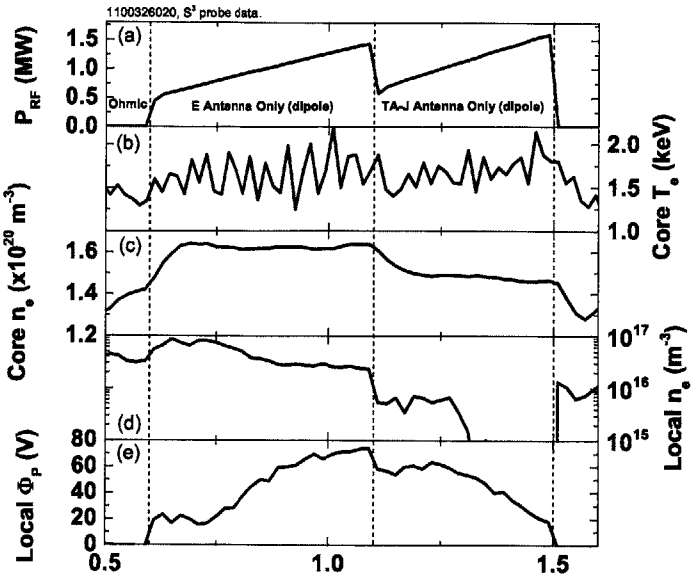

Figure 7-6: A time history of (a) the launched ICRF power, (b) the core electron temperature, (c) the line-averaged plasma density, (d) the local plasma density at the probe, and (e) the plasma potential at the probe. Active E antenna only (dipole) or active TA-J antenna only (dipole). S^3 data. $\Delta_{probe} = 2.1\ mm$. The probe is blocked to the E antenna and mapped to the TA-J antenna.

and 7-5 it is possible to reconstruct the expected influx profiles Γ_{Mo} of sputtered Mo impurity atoms from the toroidal sides of the limiter structures: $\Gamma_{Mo} = \Gamma_i Y$. These profiles are shown in Figure 7-7 (a) and (b) for the mapped and blocked active antennas, respectively. The estimated Mo influx values are for normally incident D^+ ions and the electron temperature $T_e = 10\ eV$. The incident ion energy is estimated at $3T_e + |e\Phi_P|$. Note that the estimates influx values are shown only for the cases of the incident ion energy greater than the threshold energy ($\sim 100\ eV$) and the plasma density greater than the detectable limit of the Langmuir probe ($> 10^{14}\ m^{-3}$). Mo sputtering only becomes significant across the limiter tip region $0 < \Delta_{probe} < 10\ mm$ and the typical influx values are $10^{15} < \Gamma_{Mo} < 10^{17}\ m^{-2}s^{-1}$. Accounting for the poloidal length of the outboard limiter ($\sim 0.5\ m$) and the two toroidal sides per limiter structure, implies that the total Mo source rate from the sides of a single limiter structure on Alcator C-Mod is typically $< 10^{15}\ s^{-1}$. For comparison, typical Mo source values measured in ICRF-heated discharges on plasma facing surfaces (as

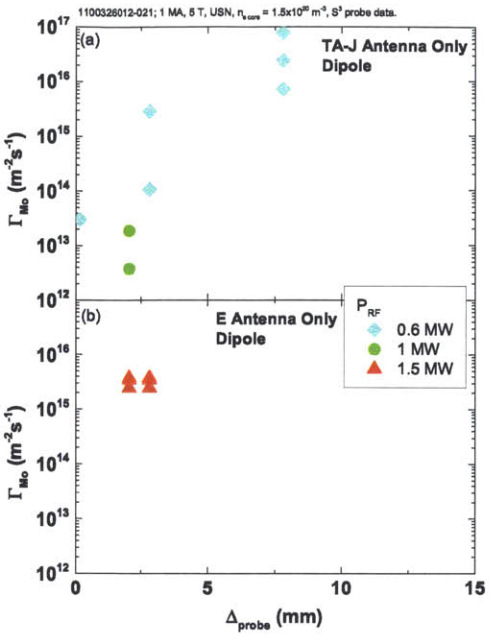

Figure 7-7: Estimated Mo impurity influx profiles sputtered by normally incident D^+ ions from the toroidal sides of the limiter structures. (a) For the active TA-J antenna only (dipole) and (b) for the active E antenna only (dipole). $T_e = 10\ eV$. S^3 probe data. The probes are mapped to the TA-J antenna and blocked to the E antenna.

opposed to the toroidal sides) of the active antenna, the inner wall, and the lower outer divertor are $> 10^{17}\ s^{-1}$ [23]. Our estimate implies that the toroidal sides of the limiter structures represent a minor contributor to the total Mo impurity source in ICRF-heated discharges on Alcator C-Mod.

7.4 Mitigation of ICRF-induced plasma potentials on Alcator C-Mod

In the previous chapters we examined the effects of ICRF power on the plasma potential in the SOL regions of Alcator C-Mod. The new result is that the plasma potential in blocked and unmapped regions scales with the local amplitude of the fast wave electric field. The resulting plasma potentials can be over 100 V, which is enough to accelerate main plasma ions (deuterium) in the SOL to energies above the sputtering threshold energy for Mo PFCs. Additionally, gradients (or electric fields) in the plasma potential cross field profile begin to modify the local plasma density cross field profile [72]. This effect directly impacts the incident ion flux and, hence, the sputtered Mo influx. The final question we want to explore in the thesis is: are there methods to mitigate (reduce) the ICRF-induced plasma potentials down to levels that have a negligible impact on the plasma-material interactions? If so, what are the conditions/mechanisms that are capable of reducing the plasma potentials in the SOL?

One of the techniques that makes a significant impact on the performance of magnetically confined plasmas is wall-conditioning. Wall-conditioning on Alcator C-Mod is achieved through boronization [64]: a thin (a few μm in thickness) layer of boron films is deposited overnight on Mo PFCs. Boronization has a number of beneficial effects on the plasma performance on Alcator C-Mod. 1) Sputtering of Mo PFCs is reduced as the plasma facing surfaces are now covered with a sacrificial layer of boron [20, 22]. 2) The Mo contents in the plasma core are reduced [24]. The reduction in the core Mo impurities leads to an improved performance of the core plasma as the line radiation power losses are now reduced.

It is also found that boronization has a strong effect on the ICRF enhancement of the plasma potential in the SOL of Alcator C-Mod: the plasma potentials become reduced in post-boronized discharges (Figure 7-8) [29]. The reducing effect of boronization on the ICRF-enhanced plasma potentials that was measured in the previous study [29] is reproduced in the current study. Figure 7-9 shows two similar

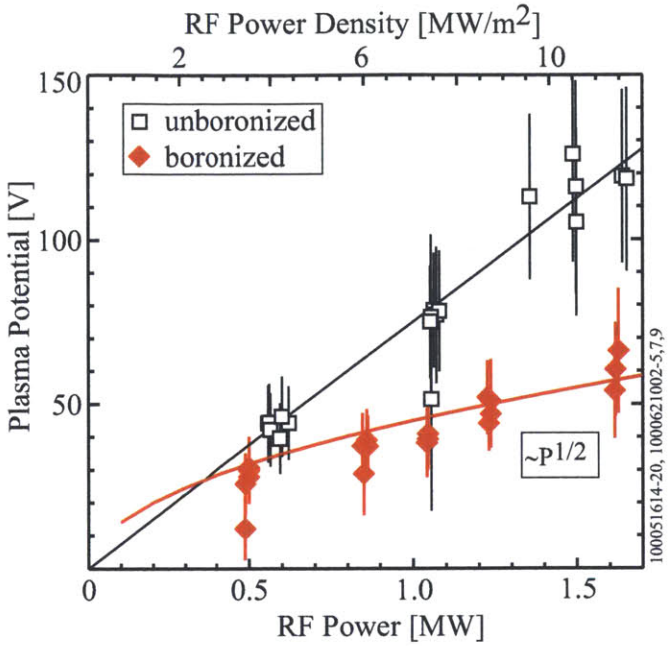

Figure 7-8: In L-mode discharges, the measured plasma potential scales as the square root of the RF power for recently boronized PFCs and linear with RF power for unboronized PFCs. Reprinted from [29] with the author's permission.

ICRF-heated discharges: a discharge was performed under pre-boronized (pre-BZN) conditions and then repeated with the boronized PFCs (post-BZN). As we saw in the previous chapter, the plasma potential in blocked regions is strongly affected by the magnitude of sawtooth core T_e oscillations. These measurements were performed with the PFCs in the pre-boronized state where the effects of the last boronization have been "worn away" by multiple ICRF-heated discharges [24]. However, the effect of the sawteeth on the plasma potential enhancement in the blocked SOL regions is reduced by nearly an order of magnitude in discharges with recently boronized PFCs, see Figure 7-9 (b).

In fact, it is observed that the ICRF-enhanced plasma potentials are reduced across a variety of L- and H-mode post-boronized discharges, see Figure 7-10. Figure 7-10 reveals that the maximum observable plasma potentials are reduced down to levels well below 100 V. Note that the previous studies [23, 29] were performed with probes that mapped to the active antennas, while the probes in the current study

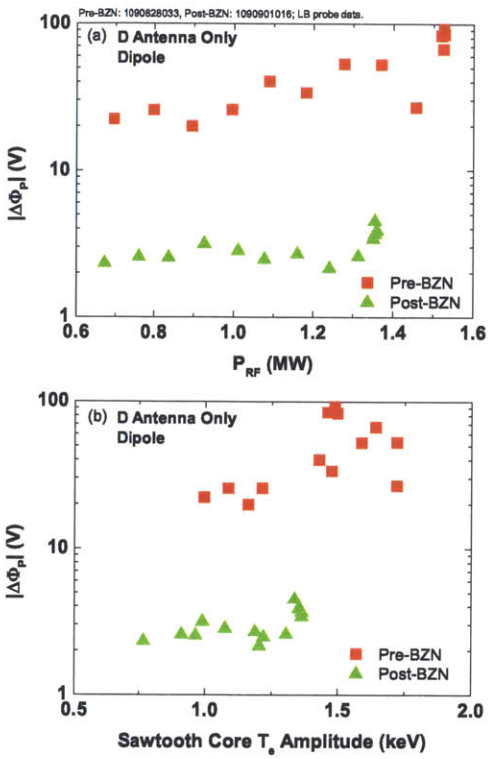

Figure 7-9: A change in the plasma potential in response to the sawtooth core T_e oscillations (a) at various levels of launched ICRF power and (b) at various sawtooth T_e amplitudes. Active D antenna only (dipole). LB probe data. The probes are blocked to the active antenna. The PFC conditions are pre-boronized (pre-BZN, solid red squares) and post-boronized (post-BZN, solid green triangles).

are blocked to the active antenna. Yet the reduction of the ICRF-enhanced plasma potentials in post-boronized discharges is similar between the two studies.

So what aspect of boronization changes the ICRF-induced plasma potentials? $\dot{B}$ measurements reveal that the ICRF wave fields in the SOL remain unchanged in pre- and post-boronized ICRF-heated discharges (Figure 7-11). The fast wave fields remain unchanged in both L- and H-mode discharges. If it is not the RF wave aspect of the ICRF enhancement of the plasma potential, then what other property changes could account for the observed reduction in the plasma potential in post-boronized ICRF-heated discharges?

Boronization deposits a thin film of an insulating material (boron) on *Mo* PFCs and, hence, changes the boundary condition at the material surface from conducting

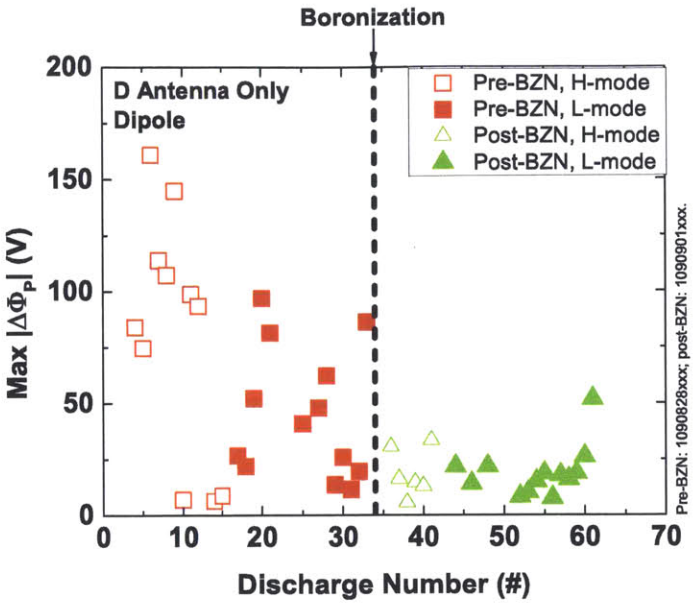

Figure 7-10: The maximum change in the plasma potential during a single ICRF-heated discharge. BZN refers to boronization. The data is shown for pre- and post-boronized discharges in L- and H-mode plasmas. Active D antenna only (dipole). LB probe data. The probe is blocked to the active antenna.

to insulating. However, the previous studies include measurements of the plasma potential on magnetic field lines that terminate on boron nitride (BN) insulating protection tiles, see Figure 7-12. These studies reveal that the plasma potential enhancement remains comparable to those in discharges where the magnetic field lines are terminated on conducting *Mo* surfaces [29]. Therefore, it appears that the change in the surface boundary condition cannot account for the observed changes in the plasma potential enhancement in pre- and post-boronized ICRF-heated discharges.

Two aspects of the plasma potential enhancement that have not been explored in neither the previous, nor the current studies are possible particle emissions from the surface. One example is a secondary electron emission from the surface: a strong secondary electron emission would reduce the electron repelling DC potential across the plasma sheath that is needed to maintain the ambipolarity condition at the surface. Secondary electrons are produced primarily by primary electrons striking the surface and the effect of the secondary electron flux on the plasma potential drop across the

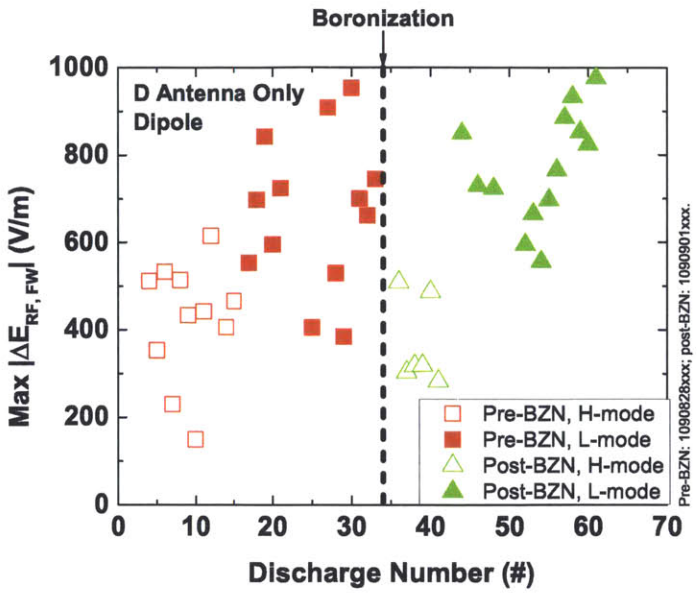

Figure 7-11: The maximum change in the fast wave electric field amplitude during a single ICRF-heated discharge. BZN refers to boronization. The data is shown for pre- and post-boronized discharges in L- and H-mode plasmas. Active D antenna only (dipole). LB probe data. The probe is blocked to the active antenna.

plasma sheath is given by Equation 7.2 [74]:

$$\frac{eV_{sheath}}{k_B T_e} = 0.5 \ln \left[\left(2\pi \frac{m_e}{m_i} \right) \left(1 + \frac{T_i}{T_e} \right) \frac{1}{(1-\delta_e)^2} \right], \tag{7.2}$$

where δ_e is the electron emission coefficient per incident primary electron. As the secondary electron emission coefficient approaches unity, the electron repelling plasma sheath (and, hence, the plasma potential) becomes greatly reduced. Pure metallic surfaces have a low (below unity) secondary electron emission yield for low energy (below 100 eV) primary electrons [97]. The secondary electron emission coefficient for Mo is $\delta_e \approx 0.6$ for normally incident primary electrons striking the surface with 50 eV [98]. However, surface impurities are known to affect (increase) the secondary electron emission yield of pure metal surfaces [98].

The second example is the emission of neutral atoms, either sputtered or ablated, from the surface and ionized in the vicinity of the PFCs. The sputtering rate of boron is much higher than the sputtering rate of Mo due to the low atomic weight

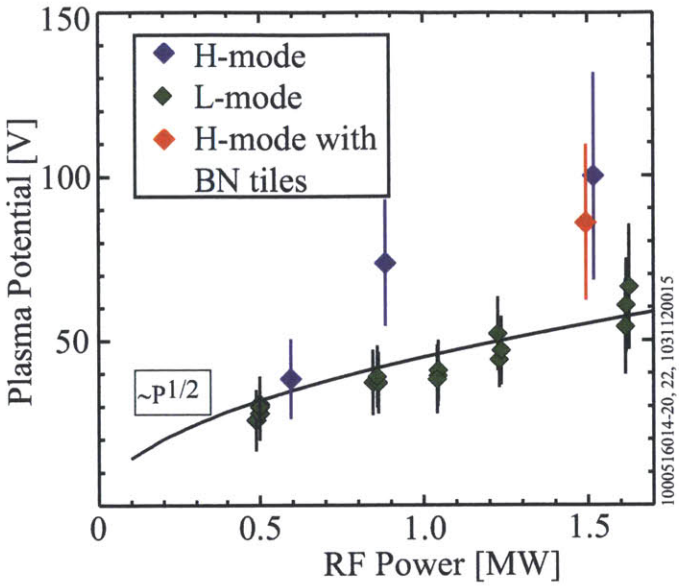

Figure 7-12: Comparison of the measured plasma potential for L and H-mode discharges showing that the H-mode potential is $\times 2$ L-mode. Comparing an H-mode discharge with boron nitrite (BN) tiles, shows the RF sheath is unaffected relative to the RF sheath in H-mode with metallic RF limiter tiles. Reprinted from [29] with the author's permission.

of boron. As a result, freshly boronized surfaces, which typically contain a mixture of B, D, and He atoms [64], introduce large quantities of low-Z impurities into the plasma. The net result is a change in the local plasma density and recycling of the main ion (deuterium) species, which then can affect both the slow and fast-wave rectified plasma potentials. Local plasma density measurements were not available for the pre- (1090828xxx) and post-boronized (1090901xxx) run days. As a result, the effect of sputtered neutral atoms on the local plasma conditions and the rectified plasma potential cannot be conclusively quantified. A detailed exploration of both the secondary electron and neutral atom emissions on the enhancement of the plasma potential on Alcator C-Mod is beyond the scope of the current thesis and is suggested as a subject of future work.

Chapter 8

Summary and conclusion

An extensive assessment of ICRF-heated discharges on Alcator C-Mod reveals that plasma material interactions become enhanced by the presence of ICRF power. Specifically, sputtering of plasma facing surfaces and impurity levels in the plasma core increase with the application of ICRF power. The leading mechanism suspected of causing enhanced sputtering is the rectification of the plasma sheath on open magnetic field lines: oscillating electric fields aligned parallel to the magnetic field ($\tilde{E}_{//}$) become rectified at the plasma sheath and the net result of the rectification is the development of an electron repelling DC potential. These DC potentials begin to accelerate incident ions toward the surface, which leads to enhanced sputtering. While enhanced plasma potentials of greater than 100 V (high enough to induce sputtering of high-Z molybdenum surfaces by deuterium ions on C-Mod) are observed in ICRF-heated discharges it is not clear what aspects of the ICRF power lead to the observed enhancement. The goal of the thesis is to experimentally deduce what mechanisms are responsible for the observed enhancement of the plasma potential.

In order to achieve the goal of the thesis multiple stationary and radially scanning probe stations were installed to determine what role local plasma properties play in enhancing the plasma sheath. Emissive probes and ion sensitive probes were used to measure the plasma potential, Langmuir probes were used to measure the plasma density and the electron temperature, and $\dot{B}$ probes were used to measure ICRF wave fields with fast and slow wave polarizations. Measurements were made on plasma flux

tubes that directly magnetically map and do not map to active ICRF antennas.

There are several proposed mechanisms that may generate $\tilde{E}_{//}$ in ICRF-heated discharges on open magnetic field lines. One mechanism involves the generation of slow waves (with a non-zero $\tilde{E}_{//}$) directly by the active ICRF antennas: this process is expected to enhance the plasma potential only on plasma flux tubes that directly magnetically map to the active antennas. One of the most defining features of the slow wave enhancement is the threshold appearance of large plasma potentials when a characteristic plasma sheath parameter Λ_o is above unity. An experimental scan of Λ_o on plasma flux tubes that directly map to the active antennas reveals the existence of such a threshold, which, in part, confirms the slow wave theory. However, we also measure significant plasma potential enhancement on plasma flux tubes that do not directly magnetically map to the active ICRF antennas. The slow wave theory cannot account for this enhancement as the slow waves directly launched by the active antennas cannot reach these locations. $\dot{B}$ measurements reveal a presence of fast ICRF wave fields in these unmapped or blocked locations and the enhanced plasma potentials show a strong correlation to the strength of the local fast wave fields. While the fast wave does not have the necessary polarization to enhance the plasma potential on open magnetic field lines ($\tilde{E}_{//} = 0$ for the fast wave), a proposed theory involves a fast-to-slow wave coupling at conducting surfaces. Multiple features of the fast-to-slow wave coupling theory are experimentally observed. These include the effect of the shape of the conducting surface, the effect of the fast wave field strength and the fast wave index of refraction. We also observe unexpected enhanced plasma potential structures that are consistent with RF wave fields being excited outside the active ICRF antenna box in regions bounded by passive limiter structures.

To summarize, our experimental assessment of the plasma potential enhancement in the SOL of ICRF-heated discharges on Alcator C-Mod reveals that the fast ICRF waves play a significant role in enhancing the plasma potential to values high enough to generate sputtering of plasma facing surfaces in regions that are non-local to the active antennas. The regions that dominate impurity production in ICRF-heated discharges on C-Mod have yet to be determined as we find that regions local and

non-local to the active ICRF antennas experience plasma potential enhancement. Additionally, we observe that the local plasma density profile is also modified by ICRF power: the implications are that ICRF-enhanced plasma potentials influence both the sputtering yield of the plasma facing surfaces and the incident ion fluxes. Our results suggest that in order to minimize the effects of ICRF power on the core plasma performance it is crucial to operate in the high single pass absorption regime.

Appendix A

Circuit diagrams

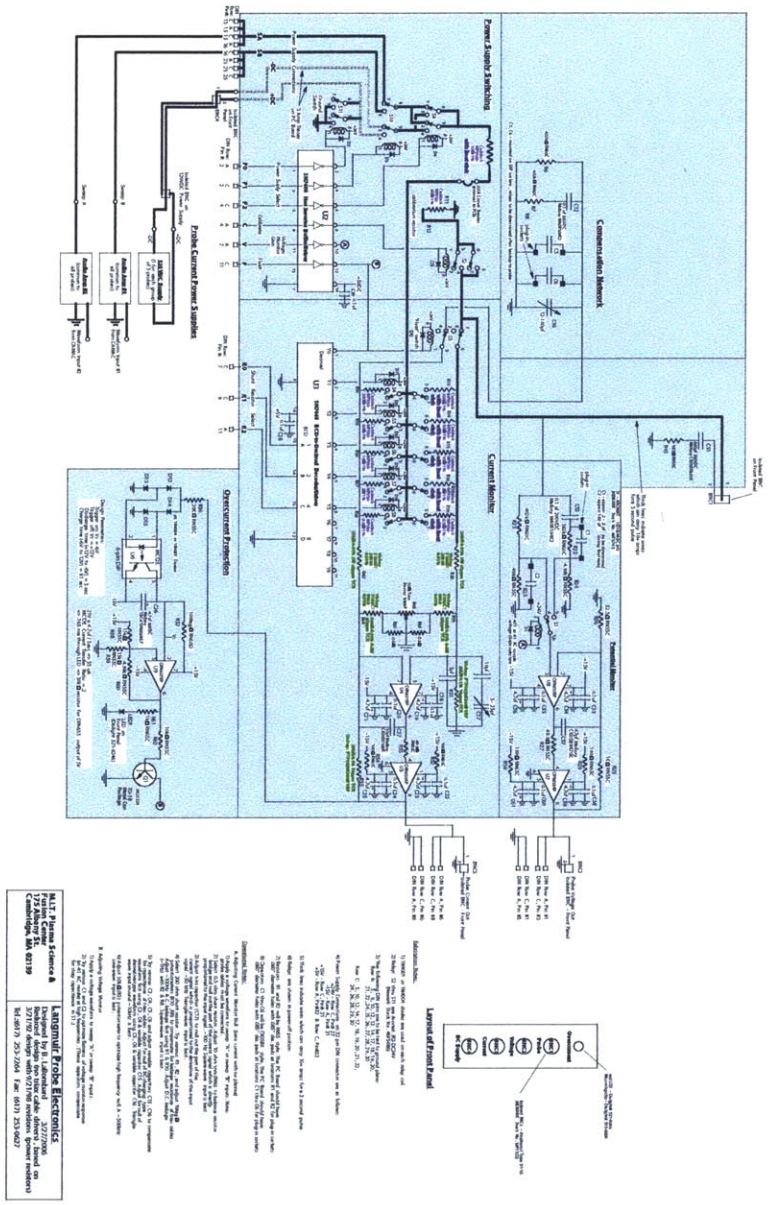

Figure A-1: A detailed circuit diagram for the electronics board used to operate Langmuir and ISP probes on Alcator C-Mod. The circuit board was designed by Brian LaBombard, PSFC, MIT.

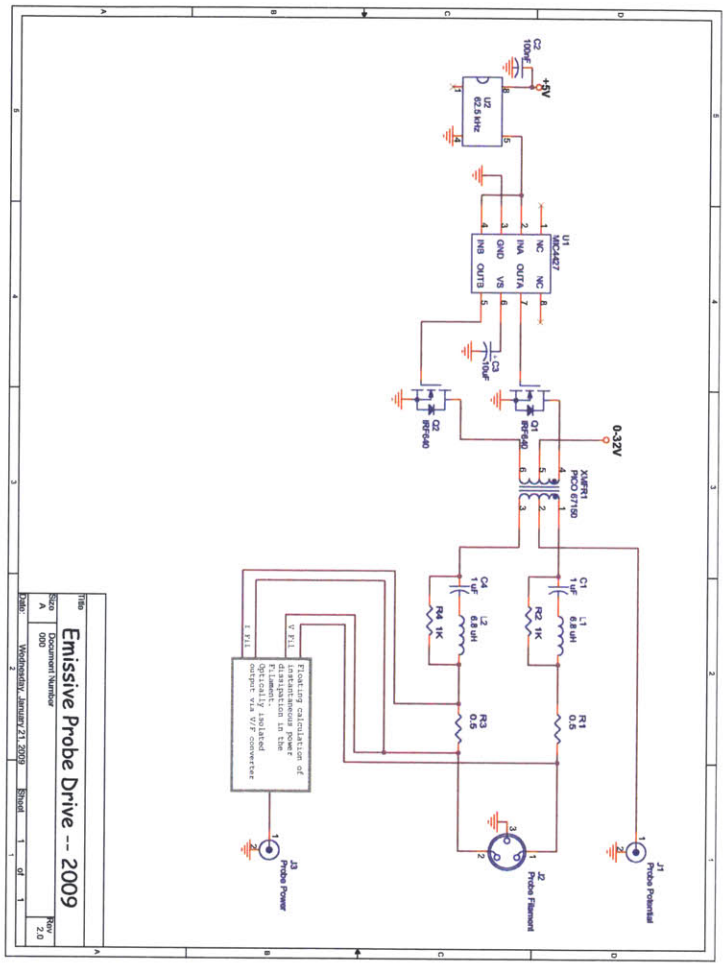

Figure A-2: A detailed circuit diagram for the electronics board used to operate emissive probes on Alcator C-Mod. The circuit board was designed by William Burke, PSFC, MIT.

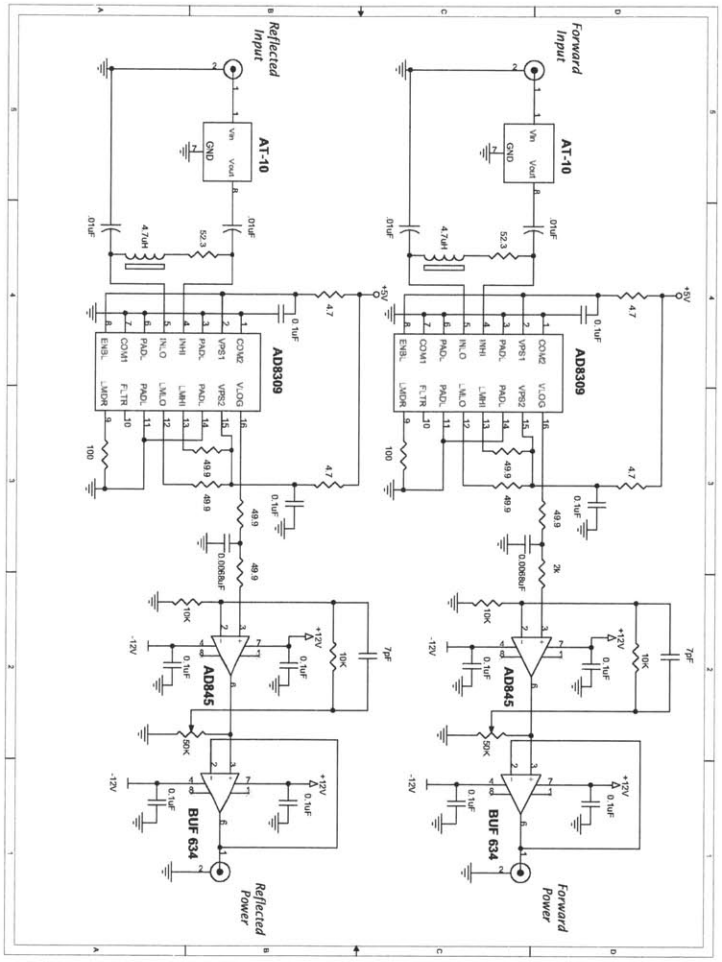

Figure A-3: A detailed circuit diagram for the electronics board used to operate $\dot{B}$ probes on Alcator C-Mod. The circuit board was designed by Richard Murray, PSFC, MIT.

Bibliography

[1] J.P. Freidberg. *Plasma Physics and Fusion Energy.* Cambridge University Press, first edition, 2008.

[2] J. Wesson. *Tokamaks.* Oxford University Press, second edition, 1997.

[3] S J Wukitch, R L Boivin, P T Bonoli, J A Goetz, J Irby, I Hutchinson, Y Lin, A Parisot, M Porkolab, E Marmar, G Schilling and J R Wilson. Investigation of performance limiting phenomena in a variable phase ICRF antenna in Alcator C-Mod. *Plasma Physics and Controlled Fusion*, 46:1479, 2004.

[4] R. I. Pinsker, M. J. Mayberry, C. C. Petty, S. C. Chiu, M. Porkolab, R. Prater, F. W. Baity, R. H. Goulding, and D. J. Hoffman. ICRF Heating Experiments on DIII-D. *American Institute of Physics Conference Proceedings*, 244:105–114, 1991.

[5] J. R. Wilson, S. Bernabei, T. Biewer, S. Diem, J. Hosea, B. LeBlanc, C. K. Phillips, P. Ryan, and D. W. Swain. Parametric Decay During HHFW on NSTX. *American Institute of Physics Conference Proceedings*, 787:66 73, 2005.

[6] G Taylor, J R Wilson, R C Goldfinger, J C Hosea, D J Hoffman, R Majeski, C K Phillips, D A Rasmussen, J H Rogers, G Schilling, J E Stevens, M G Bell, R V Budny, C E Bush, Z Chang, D Darrow, D R Ernst, E Fredrickson, G Hammett, K Hill, A Janos, D Jassby, D W Johnson, L C Johnson, S S Medley, H K Park, J Schivell, J D Strachan, E Synakowski and S Zweben. ICRF heating of TFTR deuterium supershot plasmas in the ^3He minority regime. *Plasma Physics and Controlled Fusion,* 36:523, 1994.

[7] M. J. Mantsinen, L.-G. Eriksson, C. Gormezano, F. G. Rimini, and A. C. C. Sips. ICRF heating in JET high-performance discharges: Analysis of the effects on the plasma performance. *American Institute of Physics Conference Proceedings*, 485:120 123, 1999.

[8] F. Wesner, W. Becker, F. Braun, H. Faugel, C. Hoffmann, F. Hofmeister, R. Neu, J.-M. Noterdaeme, M. Schittenhelm, T. Sperger, P. Verplancke, H. Wedler, ICRF Team, ASDEX Upgrade Team, and NBI Team. Recent results from ICRF experiments on ASDEX upgrade. *American Institute of Physics Conference Proceedings*, 355:15–22, 1995.

[9] R. J. Dumont, V. Basiuk, L.-G. Eriksson, and Tore Supra team. Second harmonic ICRF heating experiments in Tore Supra. *American Institute of Physics Conference Proceedings*, 1187:85–88, 2009.

[10] H Kimura, T Fujii, M Saigusa, S Moriyama, K Hamamatsu, M Nemoto and K Tobita. High-harmonic ICRF heating experiments in JT-60. *Plasma Physics and Controlled Fusion,* 35:845, 1993.

[11] F. Louche, P. Dumortier, F. Durodi e, V. Kyrytsya and A.M. Messiaen. 3D modeling and optimization of the ICRH antenna for the experimental fusion experiment ITER with CST Microwave Studio. *Computer Simulation Technology - 7^{th} European User Conference*, 2012.

[12] T.H. Stix. *Waves in Plasmas.* Springer, 1992.

[13] A. Parisot. *Mode Conversion Current Drive Experiments on Alcator C-Mod.* PhD Thesis, MIT, 2007.

[14] N. Smick. *Plasma Flows in the Alcator C-Mod Scrape-Off Layer.* PhD Thesis, MIT, 2009.

[15] E. Lassner, W-D. Schubert. *Tungsten: Properties, Chemistry, Technology of the Element, Alloys, and Chemical Compounds.* Springer, 1999 edition.

[16] G.M. McCracken and B.E. Stott. Plasma-surface interactions in tokamaks. *Nuclear Fusion*, 19:889 981, 1979.

[17] J. Bohdansky, J. Roth, and H. Bay. An analytical formula and important parameters for low-energy ion sputtering. *Journal of Applied Physics*, 51:2861 2865, 1980.

[18] R.A. Langley, J. Bohdansky, W. Eckstein, P. Mioduszewski, J. Roth, E. Taglauer, E.W. Thomas, H. Verbeek and K.L. Wilson. Data compendium for plasma-surface interactions. *Nuclear Fusion*, 24:9–117, S9, 1984.

[19] C. Garćia-Rosales, W. Eckstein, J. Roth. Revised formulae for sputtering data. *Journal of Nuclear Materials* , 218:8–17, 1995.

[20] D. Pappas. *Study of Molybdenum Sources and Sputtering in the Alcator C-Mod Tokamak.* PhD Thesis, MIT, 2000.

[21] F.F. Chen. *Introduction to plasma physics and controlled fusion. Volume 1, Plasma physics.* Springer, second edition, 1984.

[22] D.A. Pappas, B. Lipschultz, B. LaBombard, M.J. May, C.S. Pitcher. Molybdenum sources and transport in the Alcator C-Mod tokamak. *Journal of Nuclear Materials* , 266-269:635–641, 1999.

[23] B. Lipschultz, D.A. Pappas, B. LaBombard, J.E. Rice, D. Smith, S.J. Wukitch. A study of molybdenum influxes and transport in Alcator C-Mod. *Nuclear Fusion* , 41:585–596, 2001.

[24] E. Marmar, Y. Lin, B. Lipschultz, D. Whyte, P. Bonoli, C. Fiore, M. Greenwald, I. Hutchinson, J. Irby, M. Reinke, J. Rice, S. Scott, J. Terry, S. Wolfe, S. Wukitch, Alcator Team. Operation of Alcator C-Mod with High-Z Plasma Facing Components With and Without Boronization. *33rd European Physical Society Conference on Plasma Physics,* 2006.

[25] W.R. Wampler, B. LaBombard, B. Lipschultz, G.M. McCracken, D.A. Pappas, C.S. Pitcher. Molybdenum erosion measurements in Alcator C-Mod. *Journal of Nuclear Materials*, 266-269:217–221, 1999.

[26] L. Colas, A. Argouarch, S. Brémond, Y. Corre, M. Chantant, M. Firdaouss, M. Goniche, D. Guilhem, J.P. Gunn, J. Jacquot, M. Kubič, G. Lombard, X. Litaudon, P. Mollard, O. Meyer, K. Vulliez. RF sheath patterns modification via novel Faraday screen and strap current imbalance on Tore Supra Ion Cyclotron antennae. *Journal of Nuclear Materials*, In Press, 2013.

[27] Vl. Bobkov, E. Lerche, P. Jacquet, M.L. Mayoral, D. Van Eester, F. Braun, M. Clever, J. Coenen, L. Colas, A. Czarnecka, R. Dux, F. Marcotte, M. Maslov, A. Huber, C. Klepper, C. Maggi. G. Matthews, K. McCormick, A. Meigs, D. Milanesio, I. Monakhov, R. Neu, Th. Pütterich, F. Rimini, G. Van Rooj, G. Sergienko and the JET-EFDA contributors. ICRF specific plasma-wall interactions in JET with the ITER-like wall. *Journal of Nuclear Materials*, In Press, 2013.

[28] R. Neu, A. Kallenbach, M. Balden, V. Bobkov, J.W. Coenen, R. Dux, H. Greuner, A. Herrmann, H. Höhnle, J. Hobirk, K. Krieger, M. Kočan, P. Lang, T. Lunt, H. Maier, M. Mayer, H.W. Müller, S. Potzel, T. Pütterich, J. Rapp, V. Rohde, F. Ryter, Ph. Schneider, J. Schweinzer, M. Sertoli, J. Stober, W. Suttrop, K. Sugiyama, G. van Rooij, M. Wischmeier, ASDEX Upgrade Team. Overview on plasma operation with a full tungsten wall in ASDEX Upgrade. *Journal of Nuclear Materials*, In Press, 2013.

[29] S.J. Wukitch, B. LaBombard, Y. Lin, B. Lipschultz, E. Marmar, M.L. Reinke, D.G. Whyte, The Alcator C-Mod Team. ICRF specific impurity sources and plasma sheaths in Alcator C-Mod. *Journal of Nuclear Materials* , 390-391:951–954, 2009.

[30] H.S. Butler and G.S. Kino. Plasma Sheath Formation by Radio-Frequency Fields. *Physics of Fluids*, 6:1346–1355, 1963.

[31] J.C. Reardon. *RF Edge Physics on the Alcator C-Mod Tokamak.* PhD Thesis, MIT, 1999.

[32] I.H. Hutchinson. *Principles of Plasma Diagnostics.* Cambridge University Press, second edition, 2005.

[33] B. Lipschultz, I. Hutchinson, B. LaBombard, and A. Wan. Electric probes in plasmas. *Journal of Vacuum Science & Technology A*, 4:1810–1816, 1986.

[34] J.D. Huba. NRL Plasma Formulary. Technical report, Naval Research Laboratory, 2007.

[35] R. Ochoukov, D.G. Whyte, D. Brunner, I. Cziegler, B. LaBombard, B. Lipschultz, J. Myra, J. Terry, S. Wukitch. Investigation of RF-enhanced plasma potentials on Alcator C-Mod. *Journal of Nuclear Materials*, in press, 2013.

[36] Roman Schrittwieser, Jiří Adámek, Petru Balan, Martin Hron, Codrina Ioniţă, Karel Jakubka, Ladislav Kryška, Emilio Martines, Jan Stöckel, Milan Tichy and Guido Van Oost. Measurements with an emissive probe in the CASTOR tokamak. *Plasma Physics and Controlled Fusion*, 44:567-578, 2002.

[37] D. A. Diebold, N. Hershkowitz, J. Pew, J. Sorensen, T. Tanaka, R. Walsh, E. Y. Wang, X. Wang, and G. Winz. Phaedrus-T probe techniques. *Review of Scientific Instruments*, 66:434–436, 1995.

[38] J. P. Sheehan, Y. Raitses, N. Hershkowitz, I. Kaganovich, and N. J. Fisch. A comparison of emissive probe techniques for electric potential measurements in a complex plasma. *Physics of Plasmas*, 18:073501–9, 2011.

[39] C.R. Crowell. The Richardson constant for thermionic emission in Schottky barrier diodes. *Solid-State Electronics*, 8:395-399, 1965.

[40] X. Wang, C. T. Howes, M. Horányi, and S. Robertson. Effect of filament supports on emissive probe measurements. *Review of Scientific Instruments*, 84:013506–3, 2013.

[41] G.J. Greene. *ICRF Antenna Coupling And Wave Propagation In A Tokamak Plasma.* PhD Thesis, California Institute of Technology, 1984.

[42] Itsuo Katsumata and Moroe Okazaki. Ion Sensitive Probe-A New Diagnostic Method for Plasma in Magnetic Fields. *Japanese Journal of Applied Physics*, 6:123–124, 1967.

[43] I. Katsumata. A Review of Ion Sensitive Probes. *Contributions to Plasma Physics*, 36S:73 80, 1996.

[44] N. Ezumi, S. Masuzaki, N. Ohno, Y. Uesugi, S. Takamura, LHD Experimental Group. Ion temperature measurement using an ion sensitive probe in the LHD divertor plasma. *Journal of Nuclear Materials*, 313-316:696–700, 2003.

[45] Uehara, K., Fukumoto, R., Tsushima, A., Amemiya, H. Evaluation of ion temperature using ion sensitive probe in the boundary plasma of the JFT-2M tokamak. *Journal of the Physical Society of Japan*, 72:2804–2810, 2003.

[46] N. Ezumi, Zh. Kiss'ovski, W. Bohmeyer, G. Fussmann. Ion sensitive probe measurement in the linear plasma device PSI-2. *Journal of Nuclear Materials*, 337-339:1106–1110, 2005.

[47] J. Adámek, J. Stöckel, M. Hron, J. Ryszawy, M. Tichý, R. Schrittwieser, C. Ionită, P. Balan, E. Martines, G. Van Oost. A novel approach to direct measurement of the plasma potential. *Czechoslovak Journal of Physics*, 54:C95–C99, 2004.

[48] J. Adámek, J. Stöckel, I. Ďuran, M. Hron, R. Pánek, M. Tichý, R. Schrittwieser, C. Ionită, P. Balan, E. Martines, G. Van Oost. Comparative measurements of the plasma potential with the ball-pen and emissive probes on the CASTOR tokamak. *Czechoslovak Journal of Physics*, 55:235–242, 2005.

[49] J. Adamek, J. Horacek, H.W. Müller, R. Schrittwieser, M. Tichy, A.H. Nielsen, and ASDEX Upgrade Team. Fast ion temperature measurements using ball-pen probes in the SOL of ASDEX Upgrade during L-mode. *European Physical Society – 38th Conference on Plasma Physics*, 2011.

[50] V. I. Demidov, S. M. Finnegan, M. E. Koepke, and E. W. Reynolds. Baffled probe for real-time measurement of space potential in magnetized plasma. *Review of Scientific Instruments*, 74:4558–4561, 2003.

[51] M. J. McCarrick. R. F. Ellis, M. Koepke, and R. P. Majeski. Perpendicular ion energy analyzer for hot-ion plasmas. *Review of Scientific Instruments*, 56:1463–1464, 1985.

[52] R. Ochoukov, D. G. Whyte, B. Lipschultz, B. LaBombard, and S. Wukitch. Interpretation and implementation of an ion sensitive probe as a plasma potential diagnostic. *Review of Scientific Instruments*, 81:10E111–3, 2010.

[53] R. Ochoukov, D.G. Whyte, B. Lipschultz, B. LaBombard, S. Wukitch. Interpretation and implementation of an ion sensitive probe as a plasma potential diagnostic on Alcator C-Mod. *Journal of Nuclear Materials*, 415:S1143-S1146, 2011.

[54] R.M. Sullivan, R. Ochoukov, D.G. Whyte. Internal physics of the ion-sensitive probe. *Journal of Nuclear Materials*, In Press, 2013.

[55] G.M. Wright, D.G. Whyte, B. Lipschultz, R.P. Doerner, J.G. Kulpin. Dynamics of hydrogenic retention in molybdenum: First results from DIONISOS. *Journal of Nuclear Materials*, 363365:977–983, 2007.

[56] Isaac D Sudit and Francis F Chen. Discharge equilibrium of a helicon plasma. *Plasma Sources Science and Technology*, 5:43–53, 1996.

[57] C.D. Child. DISCHARGE FROM HOT CAO. *Physical Review*, 32:492–511, 1911.

[58] I. Langmuir. THE EFFECT OF SPACE CHARGE AND RESIDUAL GASES ON THERMIONIC CURRENTS IN HIGH VACUUM. *Physical Review*, 2:450–486, 1913.

[59] Y.Y. Lau. Phys. Rev. Lett., Vol. 87, No. 27 (2001). Simple Theory for the Two-Dimensional Child-Langmuir Law. *Physical Review Letters*, 87, 27:278301-1–3 2001.

[60] R. R. Puri, Debabrata Biswas, and Raghwendra Kumar. Generalization of the ChildLangmuir law for nonzero injection velocities in a planar diode. *Physics of Plasmas*, 11, 3:1178–1186, 2004.

[61] D. Brunner, B. LaBombard, R. Ochoukov, R. Sullivan, and D. G. Whyte. Space charge limits of ion sensitive probes. *Plasma Physics and Controlled Fusion*, in press, 2013.

[62] D. Brunner, B. LaBombard, R. Ochoukov, and D. Whyte. Scanning ion sensitive probe for plasma profile measurements in the boundary of the Alcator C-Mod tokamak. *Review of Scientific Instruments*, 84:053507–12, 2013.

[63] I. H. Hutchinson, R. Boivin, F. Bombarda, P. Bonoli, S. Fairfax, C. Fiore, J. Goetz, S. Golovato, R. Granetz, M. Greenwald, S. Horne, A. Hubbard, J. Irby, B. LaBombard, B. Lipschultz, E. Marmar, G. McCracken, M. Porkolab, J. Rice, J. Snipes, Y. Takase, J. Terry, S. Wolfe, C. Christensen, D. Garnier, M. Graf, T. Hsu, T. Luke, M. May, A. Niemczewski, G. Tinios, J. Schachter, and J. Urbahn. First results from Alcator-C-MOD. *Physics of Plasmas*, 1:1511–1518, 1994.

[64] Roman Ochoukov, Dennis Whyte, Bruce Lipschultz, Brian LaBombard, Niels Gierse, Soren Harrison. Study and optimization of boronization in Alcator C-Mod using the Surface Science Station (S^3). *Fusion Engineering and Design*, 87:1700–1707, 2012.

[65] S.J. Wukitch, D. Brunner, M.L. Garrett, B. Labombard, C. Lau, Y. Lin, B. Lipschultz, R. Ochoukov, M.L. Reinke, J.L. Terry, D. Whyte and the Alcator C-Mod Team. Evaluation of a Field Aligned ICRF Antenna in Alcator C-Mod. *International Atomic Energy Agency – 24^{th} Fusion Energy Conference*, 2012.

[66] R.S. Granetz, E.M. Hollmann, D.G. Whyte, V.A. Izzo, G.Y. Antar, A. Bader, M. Bakhtiari, T. Biewer, J.A. Boedo, T.E. Evans, I.H. Hutchinson, T.C. Jernigan, D.S. Gray, M. Groth, D.A. Humphreys, C.J. Lasnier, R.A. Moyer, P.B. Parks, M.L. Reinke, D.L. Rudakov, E.J. Strait, J.L. Terry, J.Wesley, W.P. West, G.Wurden and J. Yu. Gas jet disruption mitigation studies on Alcator C-Mod and DIII-D. *Nuclear Fusion*, 47:1086-1091, 2007.

[67] Leeds and Northrup Co. Potentiometer type optical pyrometer. *Journal of Scientific Instruments*, 17:265, 1940.

[68] W. M. Haynes. *CRC Handbook of Chemistry and Physics.* CRC Press, 93rd edition, 2013.

[69] FAR Associates. Tungsten Filament Emissivity Behavior. *http : //pyrometry.com/farassociates_tungstenfilaments.pdf*, Retrieved on July 22nd, 2013.

[70] M.N.O. Sadiku. *Elements of Electromagnetics.* Oxford University Press, third edition, 2000.

[71] I. Cziegler, J.L. Terry, S.J. Wukitch, M.L. Garrett, C. Lau and Y. Lin. Ion-cyclotron range of frequencies in the scrape-off-layer: fine structure radial electric fields. *Plasma Physics and Controlled Fusion*, 54:105019, 2012.

[72] C Lau, G R Hanson, B Labombard, Y Lin, O Meneghini, R Ochoukov, R Parker, S Shiraiwa, J Terry, G Wallace, J Wilgen and S J Wukitch. Effects of LH power on SOL density profiles and LH coupling on Alcator C-Mod. *Plasma Physics and Controlled Fusion*, 55:025008–13, 2013.

[73] L.L. Lao, H. St. John, R.D. Stambaugh, A.G. Kellman, W. Pfeiffer. Reconstruction Of Current Profile Parameters And Plasma Shapes In Tokamaks. *Nuclear Fusion*, 25:1611 1622, 1985.

[74] P.C. Stangeby. *The plasma boundary of magnetic fusion devices.* Institute of Physics Publishing, 1999.

[75] H. Kohno. *Numerical Analysis of Radio-Frequency Sheath-Plasma Interactions in the Ion Cyclotron Range of Frequencies.* PhD Thesis, MIT, 2011.

[76] J.R. Myra and D.A. D'Ippolito. Resonance Cone Interaction With a Self-Consistent Radio-Frequency Sheath. *Physical Review Letters*, 101:195004–4, 2008.

[77] J.R. Myra and D.A. D'Ippolito. Slow-wave propagation and sheath interaction in the ion-cyclotron frequency range. *Plasma Physics and Controlled Fusion* , 52:015003 15, 2010.

[78] J.R. Myra, D.A. D'Ippolito, and M. Bures. Far field sheaths from waves in the ion cyclotron range of frequencies. *Physics of Plasmas*, 1:2890–2900, 1994.

[79] D.A. D'Ippolito, J.R. Myra, E.F. Jaeger, and L.A. Berry. Far-field sheaths due to fast waves incident on material boundaries. *Physics of Plasmas*, 15:102501 12, 2008.

[80] D.A. D'Ippolito, J.R. Myra, R. Ochoukov and D.G. Whyte. Modeling far-field radiofrequency sheaths in Alcator C-Mod. *Plasma Physics and Controlled Fusion*, 55:085001, (2013).

[81] P.C. Stangeby. The Chodura sheath for angles of a few degrees between the magnetic field and the surface of divertor targets and limiters. *Nuclear Fusion* , 52:083012, 2012.

[82] W. Eckstein, J. Bohdansky, and J. Roth. Physical sputtering. *Nuclear Fusion Supplement*, 1:51–61, 1991.

[83] G. Wallace. *Behavior of Lower Hybrid Waves in the Scrape Off Layer of a Diverted Tokamak.* PhD Thesis, MIT, 2009.

[84] P.M. Bellan. *Fundamentals of Plasma Physics.* Cambridge University Press, 2006.

[85] M.L. Garrett, S.J. Wukitch, A.N. James, P. Koert, C. Lau, Y. Lin, B. Lipschultz, D.R. Miller, R. Ochoukov, M.L. Reinke, J.L. Terry. Initial Characterization of Magnetic Field-Aligned ICRF Antenna. *American Physical Society – Division of Plasma Physics: 54^{th} Annual Meeting*, 2012.

[86] N. Tsujii, M. Porkolab, P. T. Bonoli, Y. Lin, J. C. Wright, S. J. Wukitch, E. F. Jaeger, D. L. Green, and R. W. Harvey. Measurements of ion cyclotron range of frequencies mode converted wave intensity with phase contrast imaging in Alcator C-Mod and comparison with full-wave simulations. *Physics of Plasmas* , 19:082508–13, 2012.

[87] S.J. Wukitch, D. Brunner, P. Ennever, M.L. Garrett, A. Hubbard, B. Labombard, C. Lau, Y. Lin, B. Lipschultz, D. Miller, R. Ochoukov, M. Porkolab, M.L. Reinke, J.L. Terry, A. Tronchin-James, N. Tsujii, D. Whyte and the Alcator C-Mod Team. Field-Aligned ICRF Antenna Characterization and Performance in Alcator C-Mod. *American Physical Society – Division of Plasma Physics: 54^{th} Annual Meeting*, 2012.

[88] T. Tanaka, R. Majeski, D.A. Diebold, N. Hershkowitz. RF Generated Voltage On The Faraday Screen Of An ICRF Antenna And Its Effect On The Phaedrus-T Edge Plasma. *Nuclear Fusion* , 36:1609–1622.

[89] G.M. Wright, D. Brunner, M.J. Baldwin, R.P. Doerner, B. Labombard, B. Lipschultz, J.L. Terry and D.G. Whyte. Tungsten nano-tendril growth in the Alcator C-Mod divertor. *Nuclear Fusion*, 52:042003, 2012.

[90] P.C. Stangeby. Reduction of Net Erosion of High-Z Divertor Surface by Local Redeposition in DIII-D. *American Physical Society – Division of Plasma Physics: 54^{th} Annual Meeting*, 2012.

[91] G. Fussmann, J.V. Hofmann, G. Janeschitz and H.R. Yang. Sputtering flux measurements in the ASDEX divertor. *Nuclear Fusion*, 30:2319–2328, 1990.

[92] J.P. Allain and J.N. Brooks. Lithium surface-response modelling for the NSTX liquid lithium divertor. *Nuclear Fusion*, 51:023002, 2011.

[93] R. Chodura. Numerical analysis of plasma-wall interaction for an oblique magnetic field. *Journal of Nuclear Materials*, 111-112:420–423, 1982.

[94] M.A. Mantenieks. Sputtering threshold energies of heavy ions. NASA/TM–1999-209273. NASA technical report, prepared for 25th International Electric Propulsion Conference, Cleveland, Ohio, August 24-28, 1997.

[95] D. Naujoks, K. Asmussen, M. Bessenrodt-Weberpals, S. Deschka, R. Dux, W. Engelhardt, A.R. Field, G. Fussmann, J.C. Fuchs, C. Garcia-Rosales, S. Hirsch, P. Ignacz, G. Lieder, K.F. Mast, R. Neu, R. Radtke, J. Roth and U. Wenzel. Tungsten as target material in fusion devices. *Nuclear Fusion*, 36:671–687, 1996.

[96] C. Lau. *Effects of RF power on SOL density profiles and RF coupling on the Alcator C-Mod Tokamak.* PhD Thesis, MIT, 2013.

[97] A. Shih, J. Yater, C. Hor, R. Abrams. Secondary electron emission studies. *Applied Surface Science*, 111:251–258, 1997.

[98] Arnold Shih and Charles Hor. Secondary Emission Properties as a Function of the Electron Incidence Angle. *IEEE TRANSACTIONS ON ELECTRON DEVICES*, 40:4, 1993.